EFFECT OF STRESS ASSISTED AGING ON SUPERELASTIC BEHAVIOR OF A HOT-ROLLED NiTi SHAPE MEMORY ALLOY

A THESIS SUBMITTED TO
THE GRADUATE SCHOOL OF NATURAL AND APPLIED SCIENCES
OF
MIDDLE EAST TECHNICAL UNIVERSITY

BY

IRMAK SARGIN

IN PARTIAL FULFILLMENT OF THE REQUIREMENTS
FOR
THE DEGREE OF MASTER OF SCIENCE
IN
METALLURGICAL AND MATERIALS ENGINEERING

MAY 2011

Approval of the thesis:

"EFFECT OF STRESS ASSISTED AGING ON SUPERELASTIC BEHAVIOR OF A HOT-ROLLED TiNi SHAPE MEMORY ALLOY"

submitted by **IRMAK SARGIN** in partial fulfillment of the requirements for the degree of **Master of Science in Metallurgical and Materials Engineering, Middle East Technical University** by,

Prof. Dr. Canan Özgen
Dean, Graduate School of **Natural and Applied Sciences** ________________

Prof. Dr. Tayfur Öztürk
Head of Department, **Metallurgical and Materials Engineering** ________________

Prof. Dr. Şakir Bor
Supervisor, **Metallurgical and Materials Engineering, METU** ________________

Examining Committee Members

Prof. Dr. Rıza Gürbüz
Metallurgical and Materials Engineering, METU ____________________________

Prof. Dr. Şakir Bor
Metallurgical and Materials Engineering, METU ____________________________

Assist. Prof. Dr. Arcan Dericioğlu
Metallurgical and Materials Engineering, METU ____________________________

Assist. Prof. Dr. Ziya Esen
Materials Science and Engineering,Cankaya University ____________________________

Assist. Prof. Dr. Benat Koçkar ____________________________
Mechanical Engineering, Hacettepe University

Date: 05.05.2011

I hereby declare that all information in this document has been obtained and presented in accordance with academic rules and ethical conduct. I also declare that, as required by these rules and conduct, I have fully cited and referenced all material and results that are not original to this work.

Name, Last name : Irmak Sargın

Signature :

ABSTRACT

EFFECT OF STRESS ASSISTED AGING ON SUPERELASTIC BEHAVIOR OF A HOT-ROLLED TiNi SHAPE MEMORY ALLOY

Sargın, Irmak
Ms., Department of Metallurgical and Materials Engineering
Supervisor: Prof. Dr. Şakir Bor
Co-supervisor: Assist. Prof. Dr. Benat Koçkar

May 2011, 131 pages

Effect of stress-assisted aging on stress induced martensitic transformation in hot-rolled Ni-rich 50.7at. Ni%-Ti alloy has been investigated. Alloys are aged freely and under 20 MPa, 100 MPa, and 200 MPa stress at 400 °C for 90 minutes. Aging procedure affected both stress-induced and thermally induced transformation behavior. Superelasticity behavior is correlated with the multistep transformation in aged Ni-rich NiTi alloys and the aging stress level is found to be effective. Relative to the free aged alloy, the alloy aged under 20 MPa exhibited a slight and the alloy aged under 100 MPa exhibited a considerable reduction, whereas the alloy aged under 200 MPa exhibited an increase in the critical transformation stress. DSC studies have shown that the transformation is multistep for freely aged and aged under 20 MPa alloys, whereas it is single step and two-step for alloys aged under 100 MPa and 200 MPa, respectively, and this has been attributed to the effect of stress on nucleation and growth rates. As a result of the different response mechanisms to the applied stress upon loading during superelasticity testing, the recovered strain amounts varied considerably depending on the aging conditions and the test temperatures.

Keywords: Aging, Hot-rolled NiTi, Martensitic Transformations, Superelasticity

ÖZ

SICAK HADDELENMİŞ TİTANYUM-NİKEL ALAŞIMINDA GERİLİM ALTINDA YAŞLANDIRMANIN SÜPERELASTİK DAVRANIŞA ETKİSİ

Sargın, Irmak
Yüksek Lisans, Metalurji ve Malzeme Mühendisliği Bölümü
Tez Yöneticisi: Prof. Dr. Şakir Bor
Ortak Tez Yöneticisi: Yardımcı Doçent Dr. Benat Koçkar

Mayıs 2011, 131 sayfa

Sıcak haddelenmiş nikelce zengin 50.7 at. %Ni-Ti alaşımında gerilim altında gerçekleştirilen yaşlandırma işleminin martenzitik dönüşümlere etkisi incelenmiştir. Alaşımlar gerilimsiz olarak ve 20, 100, 200 MPa gerilim altında, 400 ^{o}C'de 90 dakika boyunca yaşlandırma ısıl işlemlerine maruz bırakılmıştır. Yaşlandırma işlemi hem termal hem de mekanik etki ile gerçekleşen dönüşümleri etkilemiştir. Bunun yanı sıra, süperelastisite davranışı ile çok adımlı ısıl dönüşümler arasında bağlantı kurulmuş ve uygulanan gerilim büyüklüğünün etkili olduğu gözlenmiştir. Gerilimsiz yaşlandırılan alaşıma kıyasla 20 MPa altında yaşlandırılan alaşımda kritik dönüşüm gerilimi küçük bir düşüş gösterirken, 100 MPa altında yaşlandırılan numunede bu değerdeki düşüş daha büyüktür. Öte yandan, 200 MPa altında yaşlandırılan numunede bu değer 100 MPa altında yaşlandırılan numunede gözlenen değerden az bir farkla düşüktür. Diferensiyal taramalı kalorimetri çalışmaları gerilimsiz ve 20 MPa gerilim altında yaşlandırılan numunelerde çok adımlı dönüşümün, 100 MPa ve 200 MPa altında yaşlandırılan numunelerde ise sırayla tek adımlı ve iki adımlı dönüşümün gerçekleştiğini göstermiştir. Bu durum gerilimin çekirdeklenme ve büyüme hızına bağlanmıştır. Test sıcakları ve yaşlandırma koşullarına bağlı olarak, süperelastisite testleri boyunca yükleme sırasında aktif hale gelen farklı mekanizmaların sonucu olarak geri kazanılan gerinim miktarları önemli ölçüde değişmiştir.

Anahtar Kelimeler: Yaşlandırma, Sıcak haddelenmiş NiTi, Martenzitik Dönüşümler, Süperelastisite

To My Parents and Sister

ACKNOWLEDGEMENTS

I would like to express my indebted appreciation to my supervisor Prof. Dr. Ali Şakir Bor for his guidance, supervision, encouragements and kindness from the very beginning of this thesis. I would also like to express my sincere gratitude to Assist. Prof. Dr. Benat Koçkar for her caring, comments and suggestions during the study. The friendly attitude combined with the knowledge she shared, had a major influence on me. I would also like to thank Associate Prof. Dr. İbrahim Karaman for providing me materials and his invaluable comments.

I would also like to thank Dr. Tarık Aydoğmuş for his guidance, suggestions and lasting support throughout this theses study.

I would like to thank Dr. Elif Tarhan Bor, Assist. Prof. Dr. Yunus Eren Kalay and Prof. Dr. Necati Özkan for their help with electron microscopy analysis and mechanical characterization.

This thesis would never be completed without the help, support and patience of my family. I would also like to express my sincere feelings to them for their unlimited patience and continuous support, not only in this study but also throughout my whole life. So, thank you all for your valuable existences.

I would also like to thank Güher Kotan, Evren Tan, Dr. Ziya Esen, Dr. Hasan Akyıldız and all my collegues and staff in the department for their endless friendship and support.

Last, but not least, I would like to thank Sinem Setenay Erdoğan and Seda Badem who are my childhood, youth and today, for every moment that we shared and for their endless support throughout my studies. I would also like to thank Doruk Tunaoğlu, Uğur Akyıldız, Çağdaş Cengiz, Ceren Çiçek, Ajda Akyıldız and Evrim Afacan for supporting me even when I am annoying during my studies and letting me shine a light.

TABLE OF CONTENTS

CHAPTERS

CHAPTER 1

INTRODUCTION

Shape Memory Alloys (SMAs) have attracted attention as both a materials science research field and a widely used industrial material due to their unique shape recovery properties, which stems from thermoelastic martensitic transformations. Shape memory effect can be described as recovering the deformation given in martensitic state by transforming into austenite by heat application. The SMAs show another incomparable property, superelasticity, at higher temperatures, where the high temperature phase, austenite, is thermodynamically stable but it is possible to form martensite by stress application, i.e. at temperature between A_f and M_d. Reverse transformation takes place upon unloading and as a result of this simultaneous shape recovery is achieved. There are many commercial shape memory alloys. Basically Cu-based ones; CuZnAl, CuAlNi, CuZnSi, CuAlBe, Fe-based ones, FeMnSi, Fe_3Pt, and NiTi and NiTi –based ones can be given as most widely known shape memory alloys. Among these, NiTi and NiTi-based ones come forward due to their superior mechanical properties and distinct matchless properties like corrosion resistance.

Aging is one of the frequently applied heat treatment to the Ni-rich NiTi SMAs to improve their properties. Aging results in an increase in the transformation temperatures due to depletion of Ni content of the matrix due to formation of Ni-rich precipitates. In addition, critical stress for forward martensitic transformation decreases with increased transformation temperatures and strain field created by coherent and semi-coherent Ti_3Ni_4 precipitates. Furthermore, precipitation hardening of austenite and martensite phases promotes higher strain recovery in aged NiTi alloys than the solutionized ones. Another interesting outcome of aging is the change in transformation behavior from a single step one to two or multi-step ones by introduction of intermediate R-phase and incomplete transformations mostly upon cooling.

The multi-step transformation behavior has been subject of many studies. The main aim of the studies was to elucidate the reasons behind this transformation behavior and suggesting remedies for avoiding it. The findings were such that any kind of heterogeneity stemming from presence of precipitates creates multi-step transformation behavior. The heterogeneities were related to inhomogeneous distribution of precipitates along grain boundaries and inside the grains, and might be with respect to composition and/or induced strain fields. Since these heterogeneities disappear with long aging times or higher aging temperatures, the multi-step transformation was accepted as an intermediate aging time phenomenon at high aging temperatures.

The multi-step transformations appear with splitting of martensitic transformations, from austenite to martensite or from austenite to R-phase due to slight compositional or strain field related transformation temperatures. Another reason is the different transformation routes of precipitated and precipitate-free regions. Any precautions avoiding heterogeneous distribution were suggested to hinder multi-step transformations. As a remedy to the problem stress-assisted aging was also considered.

The application of relatively higher stresses during aging seems to cause multi step transformation, whereas the alloys aged freely or under small stresses show two-step transformations. For long aging times, the transformation behavior of free aged specimens is single step whereas that of stress-assisted aged ones show two-step transformation. The multi-step transformations observed in stress-assisted aged alloys were related to the heterogeneous distribution of precipitation variants along the grain boundaries and grain interiors. The effect of stress application during aging is claimed to cause significant increase in the rate of nucleation compared to that of free-aged independent of the level of stress. On the other hand, the level of stress is important with respect to growth kinetics by increasing it proportionally but slight.

Much of the prior work on free and stress-assisted aging has concentrated on relating the resultant microstructure of aging and thermally induced transformation behavior. The effect of thermal transformation behavior and resultant microstructure on superelasticity characteristics in alloys showing multi-step transformations has not been considered deeply. The present study aims to correlate thermal transformation behavior on superelasticity in a more comprehensive and fundamental manner. In addition, higher stress levels and lower aging temperature with shorter aging times are applied to elucidate effect of stress more clearly.

CHAPTER 2

THEORY

2.1. Martensitic Transformations

2.1.1. General Features of the Martensitic Transformations

Martensitic phase transformations are first-order shear-type solid state transformations which do not follow Avrami kinetics and does not involve diffusion [1, 2]. In these types of transformations, the total distance moved by an atom is less than the interatomic distance. However, a macroscopic shape change takes place. During the martensitic transformation, in the lattice, every atom moves a relative distance to the others. So, all the atomic motions in this type of transformations occur at the same time. As a result of this, the martensitic transformations are also known as military transformations [3]. In addition, since, being the alternative transformation mechanism, diffusional transformations will occur when sufficient time is given, generally martensitic transformations are observed as a result of rapid cooling. Mostly, martensite is a metastable phase and forms as a result of quenching but, there are metals and alloys in which martensite forms under normal cooling conditions and it is stable [1, 3]. The high temperature phase is called as austenite while the low temperature phase is called as martensite which may or may not be stable. Mostly, the high temperature phase, so called austenite, has cubic Bravais Lattice structure, while low temperature phase, martensite, has a crystal structure with a lower symmetry [2]. In short, the phase forming as a result of non-diffusional shear transformation is called as martensite [1-3].

As it is stated above, martensitic transformations lead crystal structure change without diffusion. To visualize that, continuity of a line, primarily drawn on austenite phase, may be used. This line will only change its direction as a result of martensitic transformation.

The Bain transformation in steels which is presented by Bain distortion [4] can be given as an example of crystal structure change. The austenite phase with face centered cubic structure changes into body centered tetragonal structure via martensitic transformation by Bain distortion. The change of structure is illustrated in Figure 2.1. The face centered cubic structure and body centered tetragonal structure can be represented as each other as it can be seen in figure 2.1 (c). Distortion materializes with the elongation along the X and Y directions and contraction along the Z direction [5-7]. Even though, the mechanisms are different, in all metals, nonmetals and alloys the martensite formation can be explained with the elongation, contraction and shear of the parent phase in certain directions [5].

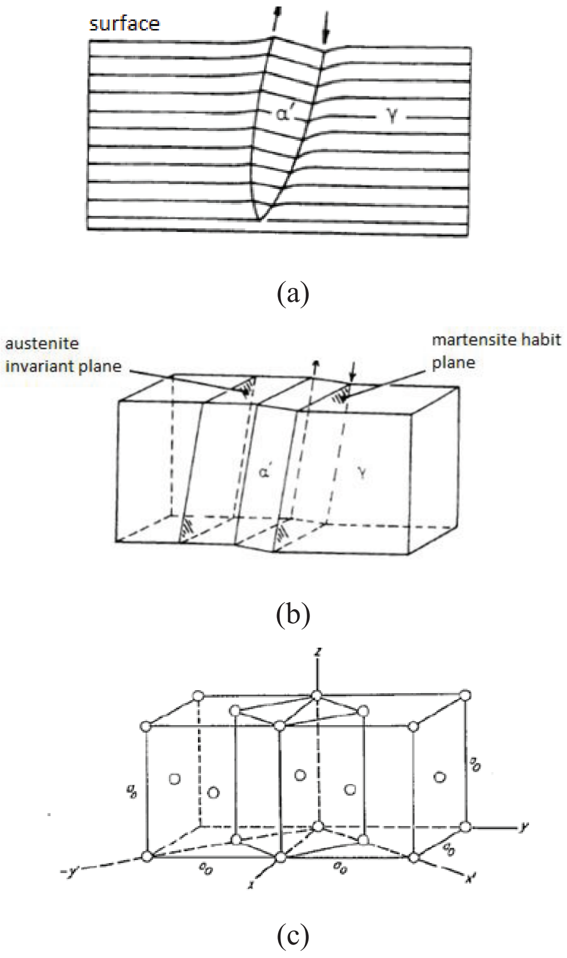

Figure 2.1 (a) Changing the direction of a line, primarily drawn on the surface of the austenite, without any discontinuity as a result of martensitic transformation. (b) Invariant planes between martensite and austenite phases and surface relief related to the martensitic transformation [8]. (c) Representation of face centered cubic structure as body centered tetragonal structure (d) Unit cell prior to Bain distortion (e) Unit cell forming as a result of Bain distortion [7].

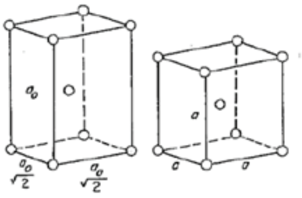

(d) (e)

Figure 2.1 (continued)

Although, the crystal structure formed as a result of martensitic transformation is same, the orientation of the individual martensite plates can be different. These martensites with different orientations are called as correspondence variants [2, 5]. As it will be explained in detail in the further parts, lattice correspondences are preferred due to the minimum energy requirements.

Martensitic transformations are first order solid state reactions and they proceed by nucleation and growth. However, since the growth of nucleated martensite reaches the speed of sound, the step limiting the rate of transformation is nucleation [9]. Based on the rate of growth, it can be stated that the interface between martensite and austenite phase is highly mobile. In addition, observations have shown that the habit plane of the martensite is an undistorted plane which means that habit plane is common for martensite and austenite. Thus, martensite phase forms as a result of homogeneous shear [8]. Additionally, to accommodate to the available volume, shears or distortions without changing the crystal structure of martensite (therefore called lattice invariant shear) are actualized by twinning or slip depending on to the alloy system as shown in figure 2.2 [5].

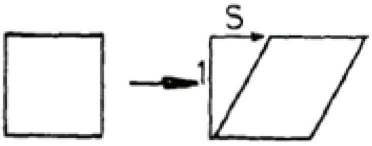

(a)

Figure 2.2 Shear strains (S) created as a result of (a) Shear without dislocation and twinning mechanisms, (b) Shear with dislocation mechanism (c) Shear with twinning mechanisms [10].

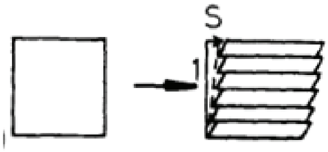

(b)

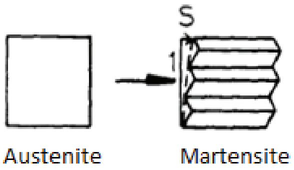

(c)

Figure 2.2 (continued)

As it can be seen in Figure 2.3, strain accommodation due to shape change occurred during martensitic transformation should be further maximized by combination of two or four mostly favored habit plane variants. The phenomenological martensite theory suggests that there can be as many as 24 habit planes, following that there are 12 possible habit planes of martensite and shear be along two opposite directions. Martensites on these 24 habit planes are called habit plane variants. The combination of two or four mostly favored habit plane variants is called self-accommodation of martensites.

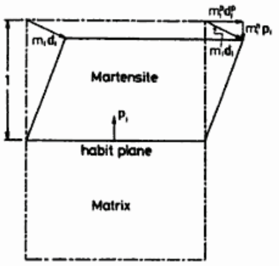

Figure 2.3 Illustration of invariant strain [11].

Figure 2.4 (a) shows a typical SEM micrograph of self-accommodation, while (b) shows four habit plane variants. Also, figure 2.4 (c) shows the basic self-accommodation morphologies.

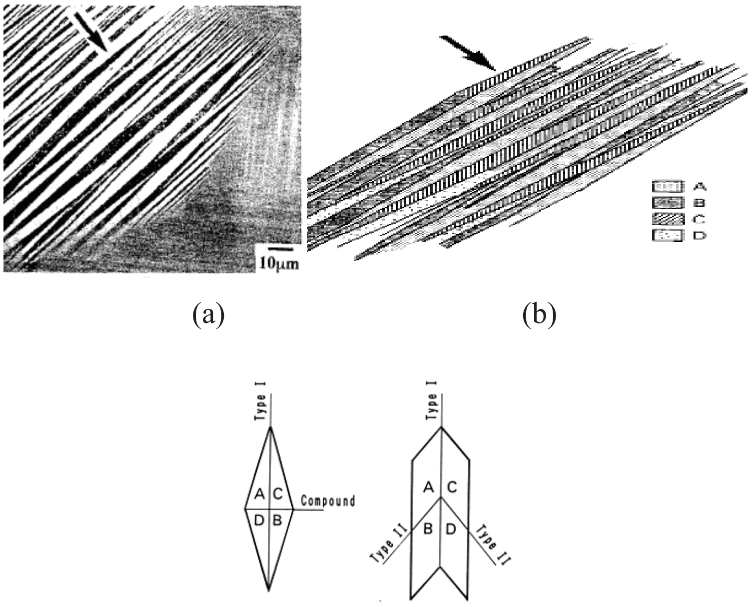

(a) (b)

(c)

Figure 2.4 Self-accommodation of martensites (a) Typical SEM image of self-accommodation of 7R (14M) martensites (b) Four habit plane variants [12] (c) Basic self-accommodating morphologies [13].

The lattice based characteristics which are explained above can be summarized as,

1. The habit plane of martensite is an invariant shear plane of homogeneous shear. This type of shear accomplishes with displacement of atoms in each plane as a linear function of distance from the habit plane (Figure 2.5) [6].

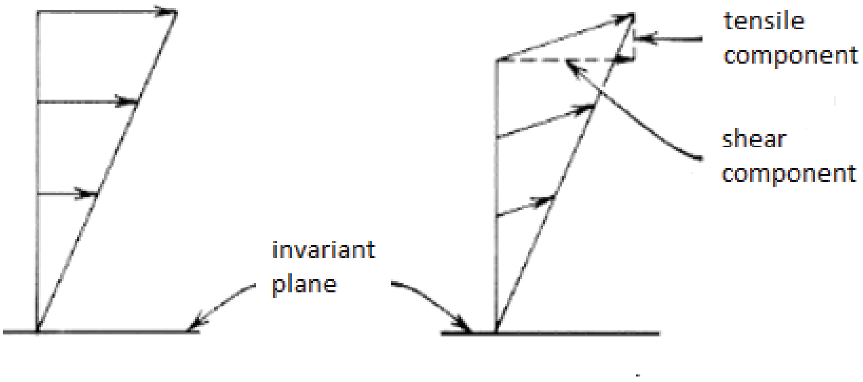

(a) (b)

Figure 2.5 Strains as a result of (a) Twinning (b) Martensite formation [6]

2. Macroscopic shape change is a result of shear strains which are invariant plane strains.
3. The habit plane of martensite is irrational.

In martensitic transformations, four different transformation temperatures are crucial; these are martensite start (M_s), martensite finish (M_f), austenite start (A_s), austenite finish (A_s). In Figure 2.7, change in Gibbs free energy with temperature and M_s and A_s are shown schematically. As it is previously mentioned, in martensitic transformations, there is no diffusion and compositional change; so, Gibbs free energy changes linearly with temperature. Also, another temperature, T_o, is worth to mention. At this temperature martensite and austenite phases are at thermodynamical equilibrium [14], and expected to be exist together. However, strains associated with martensitic transformation (in addition to such smaller surface energy requirement) hinder nucleation of martensite upon cooling [14] and austenite phase should be supercooled to provide the necessary driving force. As a result, transformation starts at M_s instead of T_o.

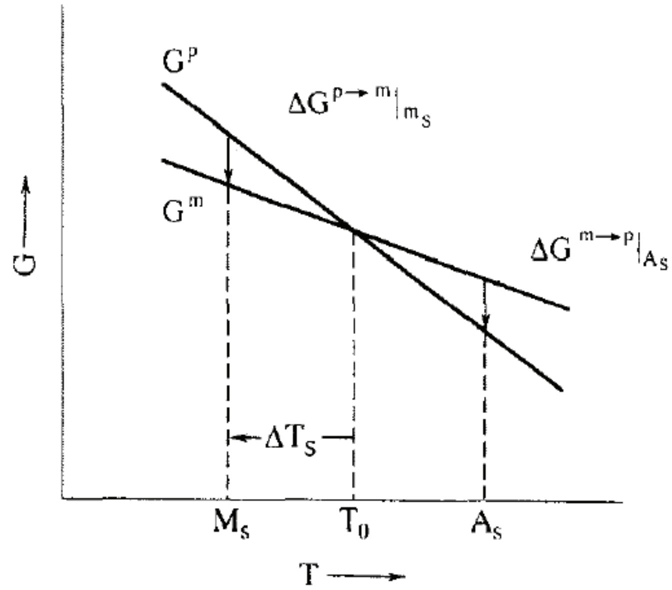

Figure 2.6 Schematic free energy versus temperature diagram for both martensite and austenite phases, M_s and A_s temperatures. Here ΔT_s is the required supercooling for forward transformation [14].

Since the formation of martensite phase affects the physical properties, in determination of transformation temperatures these physical changes, e.g., electrical resistance, are used [14]. Figure 2.7 shows results of such a measurement in Fe-29.5 Ni at. % alloy. As it is obvious from the figure, at the transformation start temperature shape and slope of the curves are changed.

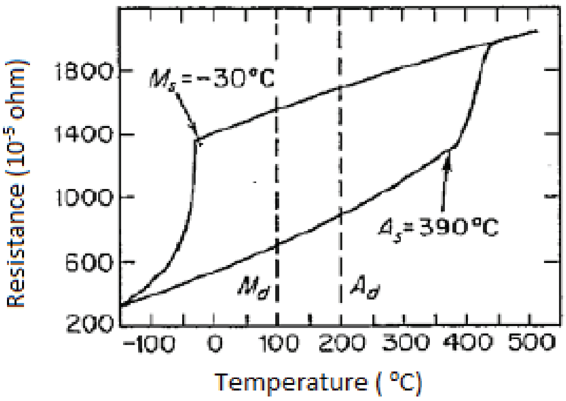

Figure 2.7 Resistance versus temperature curve for Fe-29.5 at. % Ni alloy [15].

Also, there are two other important temperatures to be mentioned. One of these temperature is M_d and it is the highest temperature at which martensite can form by application of stress [16-18]. Stress applied below this temperature make the martensitic transformations start at temperatures even above M_s because, below M_d the Gibbs free energy of martensite is lower than that of austenite, however shear strains induced by transformation prevents nucleation. When the stress is applied the energy required for nucleation of martensite decreases [16, 17]. On the other hand, if deformation takes place at a temperature above M_d, dislocation formation takes place instead of martensite formation. The effect of dislocations on transformation can be both positive and negative. Up to a critical level of deformation, the transformation is favored via increasing M_s; however, deformations higher than the critical level decreases M_s and thus make the transformation difficult. On the other hand, A_d is known as the lowest temperature at which reverse irreversible transformation is possible [16].

Gibbs free energy change involved in martensitic transformation is given as:

$$\Delta G = \Delta G_c + \Delta G_s + \Delta G_e \tag{2.1}$$

Here, ΔG_c refers to the chemical energy change associated with martensitic transformation, while ΔG_s gives the surface energy term related to the interface between martensite and austenite phases and ΔG_e stands for energy increase resulted from shear strains. The terms other than ΔG_c are named as ΔG_{nc} . Generally, chemical and nonchemical energy constituents are nearly equal to each other.

Classification of reversible martensites yields two different type of transformation: thermoelastic and non-thermoelastic. In thermoelastic martensites, since the driving force required for transformation and therefore the required undercooling and superheating is very small, there is a little difference between forward and reverse transformation temperatures, Figure 2.8 [19]. The interface between martensite and austenite phases remains highly mobile both upon heating and cooling in contrast to that in non-thermoelastic martensites. On the other hand, non-thermoelastic martensites require much higher driving force due to large transformation strains encountered and when martensite reaches to a critical size, the interface between parent and martensite phases becomes immobile due to its interaction with matrix dislocations generated. This requires new nucleation for the transformation to continue and also for the reverse transformation [20].

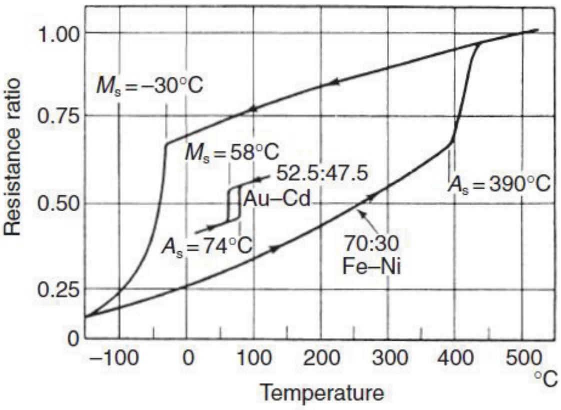

Figure 2.8 Electric resistance versus temperature curves for thermoelastic (Au-Cd) and non-thermoelastic (Fe-Ni) martensites [19].

2.1.2. Shape Memory and Superelasticity Behaviors

Shape memory behavior is observed in definite number of metals and alloys associated with their martensitic transformation characteristics. This unique behavior can be shortly defined as the recovering the shape change created in the martensite phase, up on heating and transforming back into austenite. This type of behavior is not possible for diffusional transformation. For this reason, metals and alloys which show shape memory behavior reverse transformation materializes via atomic shears exactly like forward, i.e. martensitic, transformation. In other words, for reverse shear transformation renucleation and growth are not required. This is only possible with mobile interface between austenite and martensite phase upon both cooling and heating.

Shape memory behavior was observed in Au-Cd alloys by Ölender in 1932 and Grenninger and Moordian in 1938. However, the understanding of this behavior has not been possible up to the studies of Kudjumov and Khandras in 1949 and Chang and Read in 1951 [21]. The first successful industrial application was use of shape memory material in Cryrofit

Tube couplings in F-14 fighter aircraft of the U.S.A Navy [22, 23]. The mechanism of shape memory effect and treatments providing this mechanism are shown on figure 2.9. In this figure, (a) shows the single crystal of austenite phase, while (b) shows the single crystal of martensite. The crystal of martensite, including two different variants, occurs upon cooling to temperatures below M_f. The shape change in the martensite phase is acquired with stress. The applied stress leads an interface motion like twinning between variants of the martensite resulting in the deformation of martensite (c-d). In ideal condition, martensite variants are expected to transform into a single variant with continuously applied stress. However, transforming into a single variant and shape memory effect as a result of this is not generally possible due to already present and deformation induced defects in the material. On the other hand, figure 2.9 (e) transforming back to the austenite single crystal as a result of heating is shown. The strain reducing mechanism in shape memory alloys appears as twinning instead of slip and this mechanism provides mobility of the austenite-martensite interface [24].

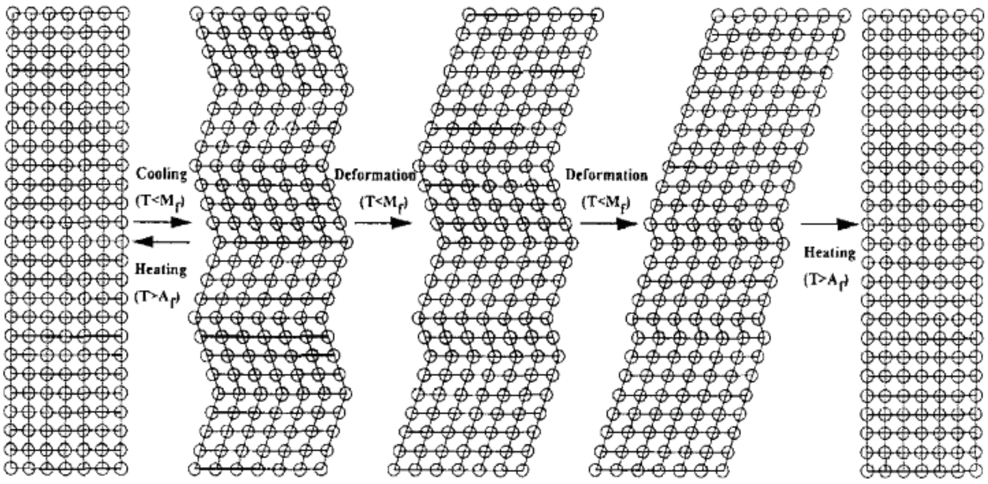

(a) (b) (c) (d) (e)

Figure 2.9 Shape memory effect mechanism (a) Austenite single crystal (b) Martensite single crystal with two variants (c-d) Deformation of martensite single crystal by growing of one variant at the expense of the others. (e) Transformation into the austenite single crystal upon heating [25].

Another unique behavior observed in shape memory alloys is superelasticity. This property is observed when the material in austenite phase is deformed at temperatures above A_f and below M_d. The deformation result in martensite formation and upon unloading reverse transformation takes place. Here, M_d temperature refers to a temperature where the austenite phase is stable below this temperature and under stress martensite phase becomes stable. In short, M_d is highest temperature where stress induced martensitic deformation can take place. In Figure 2.10, the regions of superelasticity and shape memory effect are shown on a temperature versus stress diagram. Also, critical stresses for dislocation formation of two different alloys are shown.

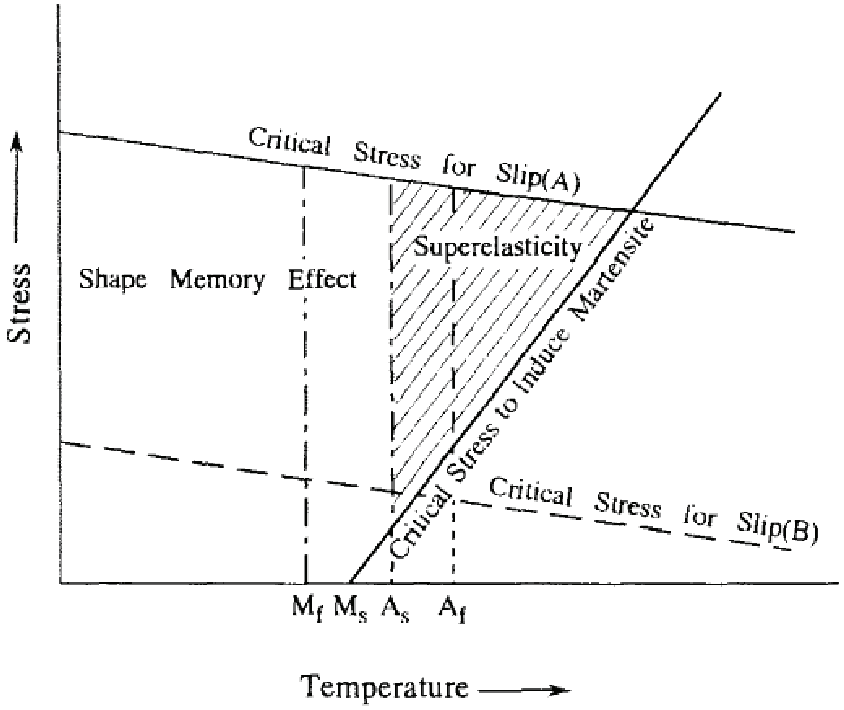

Figure 2.10 Schematic shape memory and superelasticity regions in temperature-stress coordinate. Critical stress for slip (A) and (B) refers to high and low critical stress cases, respectively [26].

For inducing transformation, also a critical stress should be exceeded. This critical stress is determined by the stability of the austenite phase. As stability of austenite compared to martensite increases, in other words as the temperature increases, the critical stress for transformation also increases. Actually, M_d depends on this criterion. If the temperature is higher than M_d the critical stress increases for inducing martensitic transformation increases such that it becomes higher than critical stress for slip and slip takes place before the transformation. The relationship given below gives the change in critical stress for transformation with temperature.

$$\frac{d\sigma}{dT} = -\frac{\Delta H^{A-M}}{T_0\,\varepsilon^{A-M}} \tag{2.2}$$

This relationship, which is a modified form of Clausius-Clapeyron equation, shows that the critical stress for inducing martensitic transformation increases linearly with increasing temperature [14].

Figure 2.11 demonstrates the superelasticity and shape memory effect. Thermomechanical treatments of shape memory alloys are free recovery and constrained recovery. Free recovery is recovering the shape of shape memory alloys which are deformed in martensitic state, upon heating without applying stress. This can be seen on figure 2.12 in the grey colored area. The alloy is deformed up to 4.5 % below M_f, upon unloading; it recovers 0.5 % of the strain elastically. When the alloy is heated to A_s reverse transformation starts to take place and recovery starts. When the temperature is reached to A_f for this situation full recovery and under certain conditions partial recovery is maintained. The amount of recovered strain depends on the amount of deformation of martensite. When the deformation is applied to levels which are exceeding a critical one, the unrecovered strain starts to increase rapidly. This is named as memory loss. Actually, amount of deformation is not only effective on unrecovered stress but also on transformation temperatures. In other words, as a result of irreversible deformation in the martensitic state, A_s and A_f change, the change is in a way that they nearly increases linearly with increasing percent deformation.

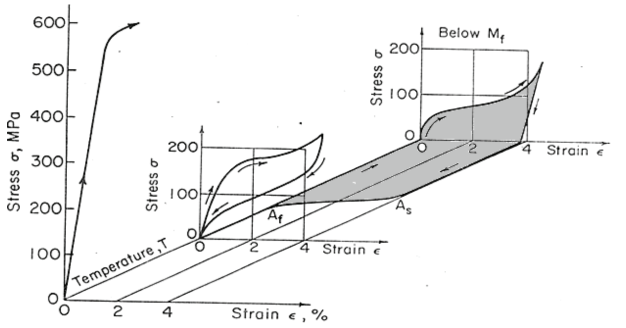

Figure 2.11 Representation of shape memory and superelasticity effects on temperature-stress-strain diagram.

Constrained recovery provides elastic or plastic strains as a result of limiting macroscopic volume change during transformation. During process, after deformation of alloy in martensitic state, it is placed in a constrained volume which is smaller than its own. Subsequent to this, alloy is heated with limiting volume change. Upon heating, additional strains are created on the surface of the material. These additional strains cause irreversible or reversible shape change [27]. This constrained recovery can be shortly defined as hindering shape recovery upon heating of a previously deformed alloy.

Generally, the term shape memory effect refers to one way shape memory behavior which is defined as remembering the shape of the high temperature phase. On the other side, two way shape memory effect can be observed in shape memory alloys as a result of mechanical or thermal processes. The term two way shape memory refers remembering of not only high temperature but also low temperature shape. Requiring the presence of internal strains, dislocation substructures, retained martensite or austenite phase and/or secondary precipitates in the austenite phase make this effect only observable subsequent to thermal or mechanical treatments [28-32]. Remembering the shape of martensite phase is associated with anisotropy in the substructure provided by the microstructural features mentioned above [28, 32].

The mechanical treatment applied for inducing two-way shape memory effect is mainly severe plastic deformation of martensite phase. Cyclic loading and unloading are applied for severe deformation. As a result of these deformation cycles dislocation arrays are created in the structure. Also, thermal treatments applied for gaining two-way shape memory effect is generally restrained heating of the previously deformed shape memory alloy. In figure 2.12 mechanical and thermal processes for inducing two-way shape memory effect are shown.

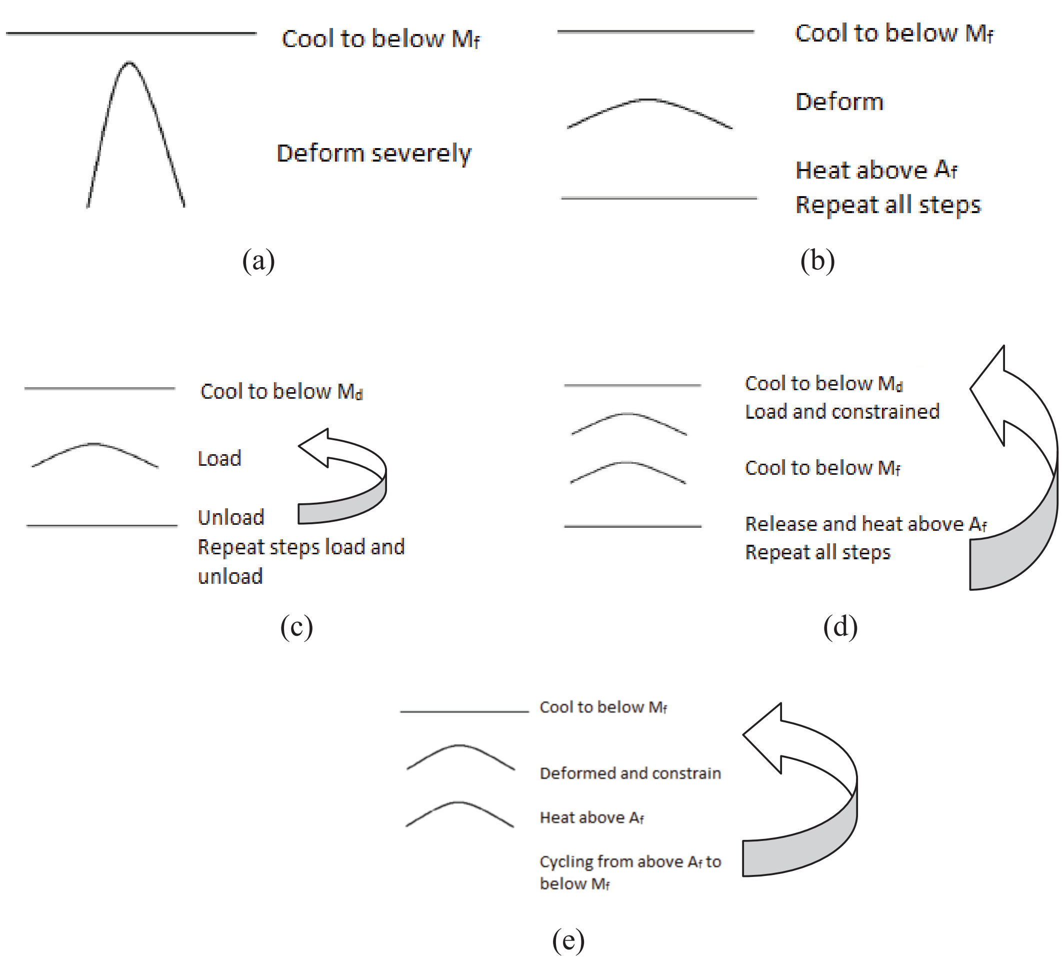

Figure 2.12 Different procedures for inducing two way shape memory effect (a) severe deformation of martensite phase, (b) repeated shape memory cycles, (c) repeated superelasticity cycles, (d) combined shape memory and superelasticity cycles, (e) constrained thermal cycling of deformed martensite [33].

Two-way shape memory behavior is observed as a result of formation of some martensite variants preferably. The dislocation arrays centered on grain boundaries due to deformation are the basic effect leading to this variant selection [34]. Dislocations formed at low temperature stay in the matrix although the phase transformation takes place upon heating. As a result of this, the boundaries of the martensite plates which formed at low temperature or when the material is under constraint are preserved by dislocation loops and residual strains when the alloy transformations into the austenite. Due to these substructures, martensite plates prefer to form with the same orientation upon cooling [27].

2.2. Ni-Ti Based Shape Memory Alloys

2.2.1. History and General Characteristics

Nickel – titanium based shape memory alloys are attractive for both industrial application and research areas firstly due to their comparatively superior mechanical properties. However, not only for mechanical properties but also for both diffusional and non-diffusional phase transformations that they can go through, they are appealing. Because, mechanical properties and shape memory characteristics can be modified and improved via these phase transformations.

This unique shape memory alloy was firstly found by Buehler et. al. in 1963. Although, the shape memory behavior was previously observed in Au-Cd and In-Tl system, Ni-Ti alloys got the priority in shape memory research and industrial application in a very short time [35]. The alloy was called as Ni-Ti-NOL or Nitinol since it was invented in Naval Ordnance Laboratory (NOL).

Besides, the Ni-Ti based shape memory alloys show two-way shape memory effect. In addition, the elastic anisotropy of these alloys are lower compared the other shape memory alloys. Also, having monoclinic martensite structure is not common in shape memory alloys. Furthermore, it has excellent corrosion and wear resistance.

Ni-Ti based shape memory alloys are classified according to their composition. NiTi is an equiatomic intermetallic compound. The alloys with nickel amount between 50.0 at. % and 50.7 at. % are called as near-equiatomic, while the alloys with the higher nickel content are named as Ni-rich [36]. Besides this, Ni-Ti shape memory alloys are classified according to their transformation temperatures and in result application environment temperatures.

NiTi alloys produced in industrial quantities may have transformation temperatures in a range of -150 °C to +100 °C. Generally, binary Ni-Ti alloys have transformation temperatures between -30 °C and +100 °C. The nickel –titanium shape memory alloys with transformation temperatures lower than -50 °C are called cryogenic alloys [22]. On the other hand, alloys with stable reverse transformation temperatures above 120 °C are called high-temperature shape memory alloys [37].

Transformation temperatures are highly composition dependent**.** The effect is such powerful that a 1% change in the atomic concentration may result in change of transformation temperatures by about 100 °K [38]. Although NiTi is an intermetallic, it can solve excess amount Ni at high temperatures. Transformation temperatures are strongly dependent on Ni-content. The effect of Ni-content is seen as a drastic decrease in transformation temperatures with increasing Ni-content. Figure 2.13 shows the change in M_s with respect to Ni content for binary Ni-Ti alloys. On the other hand, on the Ti-rich side, transformation temperatures are almost constant around 60 °C because there is no solubility on this side. Although, composition is Ti-rich the alloy behaves as NiTi phase.

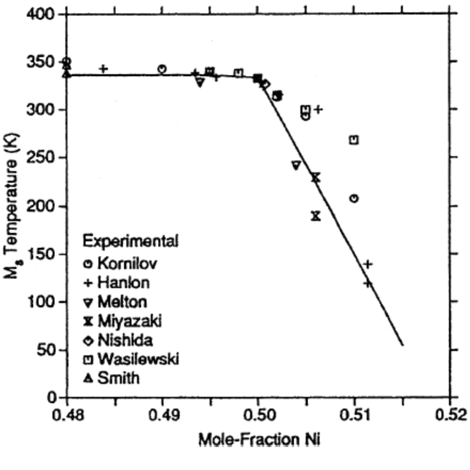

Figure 2.13 M_s as a function of Ni-content in binary Ni-Ti alloys [39].

2.2.2. Titanium- Nickel Phase Diagram

Figure 2.14 shows the Ti-Ni phase diagram revised in 2007 by Zhang [40]. There are three stable intermetallic, namely Ti_2Ni, NiTi and $TiNi_3$ and two intermediate metastable intermetallics between NiTi and $TiNi_3$ which are Ti_3Ni_4 and Ti_2Ni_3. The solubility of Ni in NiTi is a function of temperature and below 500 °C, it diminishes.

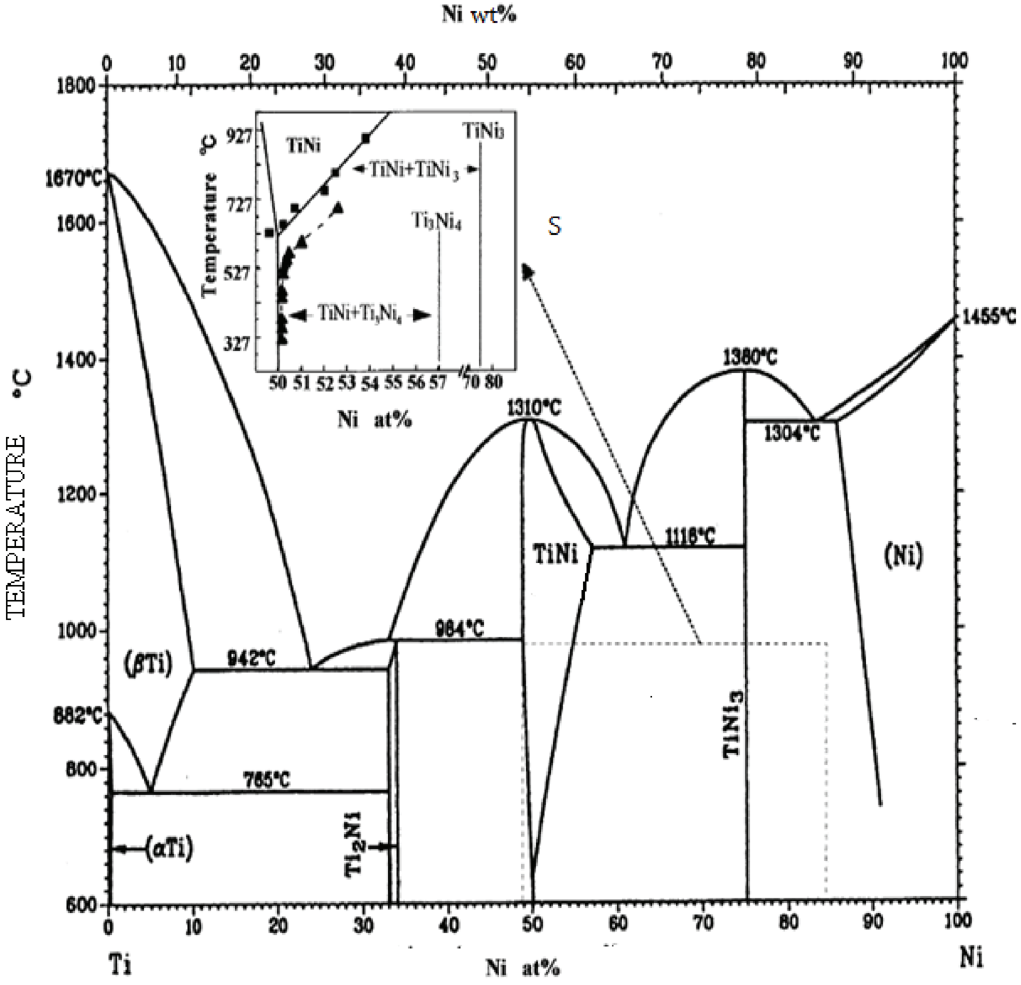

Figure 2.14 Ti-Ni phase diagram with enlarged region of metastable intermetallics [40].

2.2.3. Martensitic Transformations in Ni-Ti Based Alloys

NiTi alloys transform via different routes as a result of alloying, mechanical and thermal treatment [41-44]. Figure 2.15 shows the different transformation routes and their conditions.

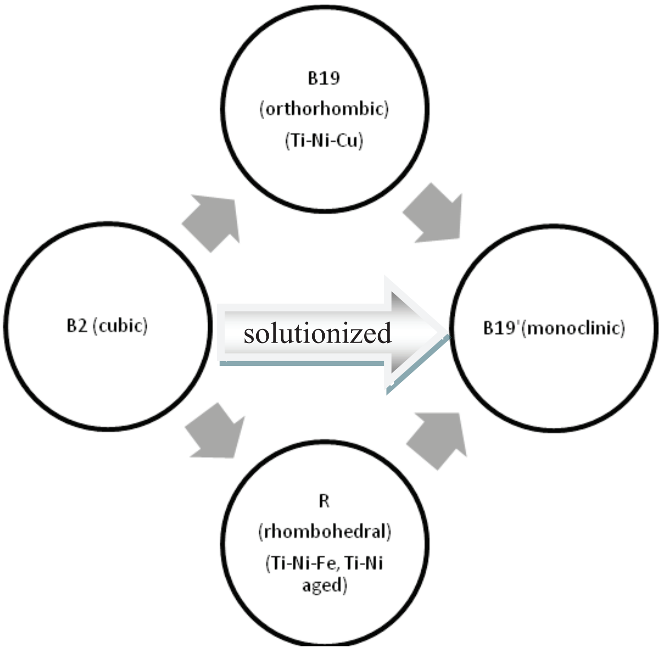

Figure 2.15 Different transformation routes observed in Ni-Ti based shape memory alloys.

2.2.3.1. $B2 \rightarrow B19'$ Transformation

Equiatomic NiTi has a parent phase with a CsCl type B2 (BCC) structure with lattice constant of 0.3015 nm at room temperature. When the binary Ni-Ti alloys are quenched from high temperature B2 phase to temperatures below M_s, $B2 \rightarrow B19'$ transformation takes place. B19' refers to a monoclinic crystal structure and has lattice parameters of a=0.2889 nm, b=0.4120 nm, c=0.4622 nm, and $\beta = 96.8^o$ for binary NiTi alloys [45].

Figure 2.16 represents the lattice change during the $B2 \rightarrow B19'$ martensitic transformation. (a) shows the lattice consisting of 4 unit cells of the parent phase with B2 structure. Tetragonal unit cell associated with Bain distortion is shown with bold lines. On the other hand, (b) shows the lattice of the martensite phase. The dotted lines seen on the figure 2.16 (b) is exactly same with (a) and drawn to show the lattice change more obvious. During the transformation, simultaneously, $[\bar{1}00]_P$ vector and $[01\bar{1}]_P$ vectors shrink and become a and b axes of the martensite, respectively. In the meanwhile, with a shear which is introduced on $(001)_P$ plane in $[100]_P$ direction to change β angle from 90^o to 96.8^o.

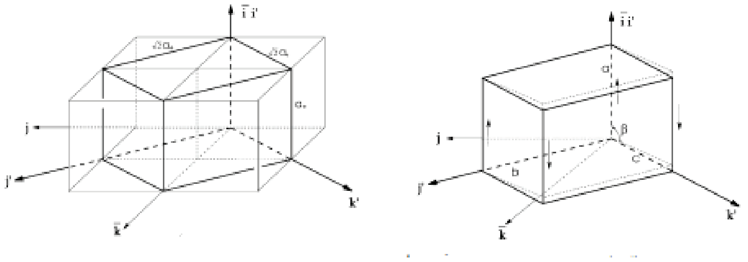

(a) (b)

Figure 2.16 Lattice change during (a) B2 to (b) B19' transformation. i, j and k represents parent lattice and i', j' and k' represents the martensite lattice [38].

Due to the low symmetry of monoclinic structure, it is expected that there are many lattice invariant shear candidates. However, $<011>_m$ Type II twinning is found to be dominant among observed twinning modes which are $\{\bar{1}\,\bar{1}\,1\}$ Type I, {111} Type I, {011} Type I, <011> Type II and compound twin [46].

2.2.3.2. B2 → B19 Transformation

Alloying elements, mechanical and thermal treatments may change the resultant martensite structure and transformation routes [38, 47, 48]. When Cu is added as alloying element, the transformation route changes from $B2 \rightarrow B19'$ to $B2 \rightarrow B19$ or to $B2 \rightarrow B19 \rightarrow B19'$ according to the amount of addition. In $Ti_{50\text{-}x}Ni_{50}Cu_x$ when $x \geq 7.5$; transformation takes place. In a rigorous manner, when x=5, the transformation turns into a two step; $B2 \rightarrow B19 \rightarrow B19'$ [38]. B19 has an orthorhombic structure. Figure 2.17 summarizes the transformation routes changing with Cu content.

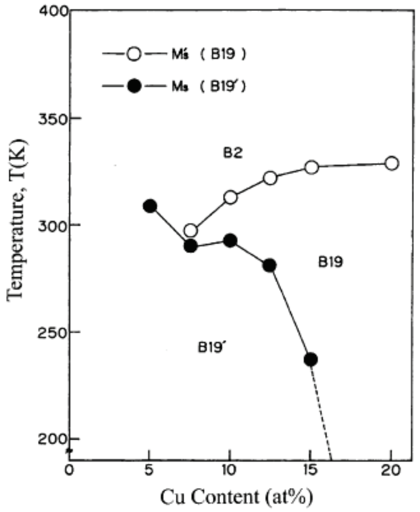

Figure 2.17 Effect of Cu amount on transformation temperatures [41].

The structure of martensite in the first stage of $Ti_{50}Ni_{50-x}Cu_x$ (x is between 10 and 30) is B19. It is orthorhombic and lattice parameters are composition dependent [49-51].

There is no lattice invariant shear related to this transformation [50, 52]. There are two twinning modes in B19 martensite; $\{111\}_o$ Type I and $\{011\}_o$ compound which are originated from $\{011\}_p$ and $\{001\}_p$ planes of the parent phase, respectively. The common point of these twins is that both associated with small twinning shears [38].

2.2.3.3. $B2 \rightarrow B19 \rightarrow B19'$ Transformation

The in-situ TEM studies of Fukudo et. al. revealed that transformation from B19 to B19' takes places without presence of a fixed habit plane. B19' structure forms by $[100]_o$ shear on $(001)_o$ plane. This invariant shear leads to formation of $(001)_m$ compound twinning [53]. During $B2 \rightarrow B19 \rightarrow B19'$, two successive transformations actualized in very near temperature and they coincide with each other. As a result of this, a decrease in resistance is observed. Actually, this is a reflection of the $B2 \rightarrow B19$ transformation. However, the expected increase in resistivity as a result of $B2 \rightarrow B19'$ is not observed because the effect of former transformation on resistivity dominates and makes the latter transformation difficult to observe [38].

2.2.3.4. $B2 \rightarrow R$ Transformation

R-phase is generally accepted as an intermediate phase between $B2 \rightarrow B19'$ transformations. It is seen under certain conditions with a sharp increase of electrical resistivity with extremely small temperature hysteresis which is around 1-2 ^oK [38] and sharp superlattice reflections in diffraction patterns at 1/3 positions along <110> and <111> [54]. The conditions that lead to R-phase formation are substitution of a few percentage of Ni in Ti-50Ni alloy by Fe or Al, precipitation of Ti_3Ni_4 and arranged dislocation structures as a result of cold work and subsequent heat treatment. Presence of substitutional alloying elements, stress field created by precipitates and dislocations are effective on both $B2 \rightarrow R$ and $B2 \rightarrow B19'$ transformations. However, effect on the latter one is more pronounced [55].

R-phase lattice is rhombohedral and it can be described by the stretching of parent lattice along <111> diagonal direction. Figure 2.18 shows the lattice change during $B2 \rightarrow R$ transformation. α-angle deviates from 90^o with decreasing temperature. R-phase strains are very small, below 1%, and change with temperature [56]. It is expected to change with stress; however this is not experimentally proven [57].

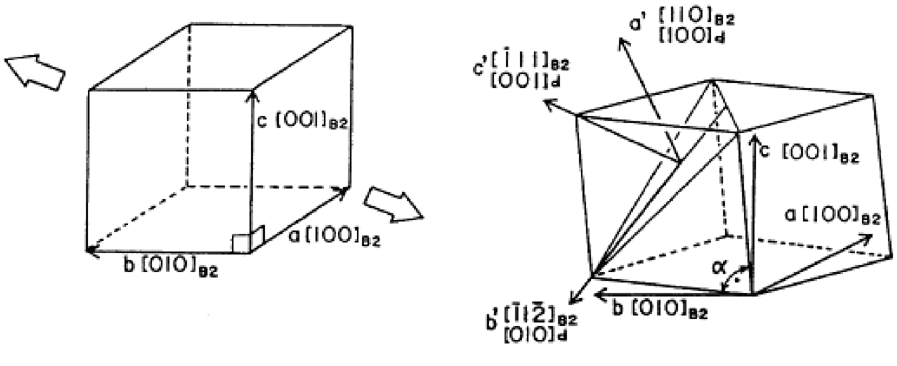

(a) (b)

Figure 2.18 Changes in lattice from (a) B2 to (b) R-phase [58].

Although, $B2 \rightarrow R$ was once considered as a premartensitic phenomenon [59], its clearly seen plates [60], shape memory and superelasticity behavior reveal that it is also a martensitic transformation [61-65]. Just like $B2 \rightarrow B19'$; this transformation is also a thermoelastic one proceeding with nucleation and growth steps. Figure 2.19 shows the growing R-phase plates upon cooling. (b) shows that upon cooling R-phase plates grow from the dislocations 1 and 2 which are shown in (a). These plates grow and join together with further cooling (c). As temperatures decreases more, other R-plates form and grow and upon heating they get smaller and disappear [47].

(a) (b) (c)

Figure 2.19 Electron micrographs showing R-phase nucleation from single dislocations (Ti48Ni-2Al alloy) [66].

It is possible to observe R-phase with two different morphologies, namely straight band and herring bone, according to view direction of austenite phase. The straight band morphology is view from $[100]_{B2}$ and the latter one is view from $[001]_{B2}$ [47]. The self accommodation of R-phase actually determines the morphology. A schematic representation of this can be seen in figure 2.20. The axes on the figure refer to the parent lattice.

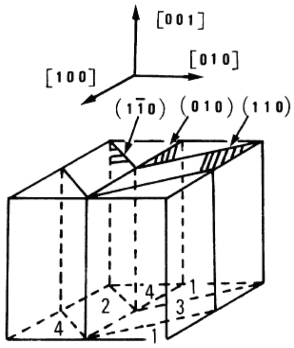

Figure 2.20 Three dimensional schematic representation of self-accommodation of R-phase [66].

2.2.3.5. $B2 \rightarrow R \rightarrow B19'$ Transformation

In $Ti_{50}Ni_{47}Fe_3$ alloy which has gone through $B2 \rightarrow R \rightarrow B19'$ transformation, the lattice defects in B19' martensites are reported as $(11\bar{1})_m$ twins and stacking faults on $(001)_m$ basal plane [67]. On the other hand, in aged Ti-51Ni alloy again after $B2 \rightarrow R \rightarrow B19'$ transformation $(001)_m$ twinning is observed by Nishida et.al. [68].

2.2.4. Diffusional Transformations in Ni-Ti Based Alloys

Diffusional transformations of Ni-Ti system include formation of metastable and stable intermetallics as a result of aging in Ni-rich Ni-Ti alloys. TTT diagram for Ti-52 at.% Ni alloy given in Figure 2.21 shows that Ti_3Ni_4 forms as a result of aging at low temperatures and/or for short times, while aging at high temperatures and/or for long time lead to formation of stable phase $TiNi_3$. On the other hand, moderate aging temperatures and times yield Ti_2Ni_3 [69]. This aging behavior is very similar to that observed in Al-Cu alloys. For this case, the first intermediate intermetallic to form is Ti_3Ni_4. Even at low aging temperatures for prolonged aging times Ti_3Ni_4 dissolves in the matrix and simultaneously formation of Ti_2Ni_3 phase is observed. When the isothermal treatment continues, the dissolution of Ti_2Ni_3 and formation of $TiNi_3$ take place concurrently. Later studies have shown that the maximum temperature where the formation of Ti_3Ni_4 possible is 680°C

[70]. The crystal structures and lattice parameters of the intermetallics are given in Table 2.1.

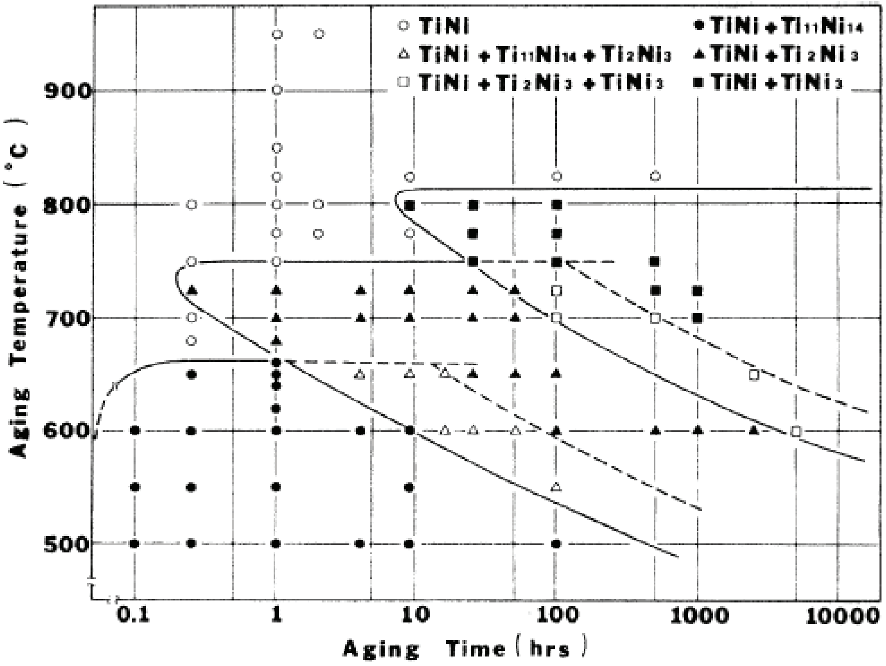

Figure 2.21 TTT diagram of Ti-52 at. % Ni [69].

Table 2.1 Crystal structures and lattice parameters of precipitate candidates in Ni-Ti system.

Phase	Ni_4Ti_3	Ni_3Ti_2 [74]		Ni_3Ti
		Low temp.	High temp	
Crystal Structure	Rhombohedral [71,72]	Orthorhombic	Tetragonal	Hexagonal DO_{24}
a	0.670 nm[72,73]	0.4398nm	0.3095nm	0.51010nm[75]
b		0.4370nm		
c		1.3544nm	1.3585nm	0.83067nm[75]
α	113.8° [72,73]			

2.3. Aging of Ni-Ti Shape Memory Alloys

For achieving the aim of optimizing and improving shape memory and other related behaviors in Ni-Ti alloy system, aging is a very common method. Figure 2.22 recalls the portion of the phase diagram associated with aging treatment. Subsequent to quenching from single B2 region NiTi shape memory alloys with nickel content higher than 50.5 at. % decomposes into metastable and stable phases at temperatures below 800°C [38].

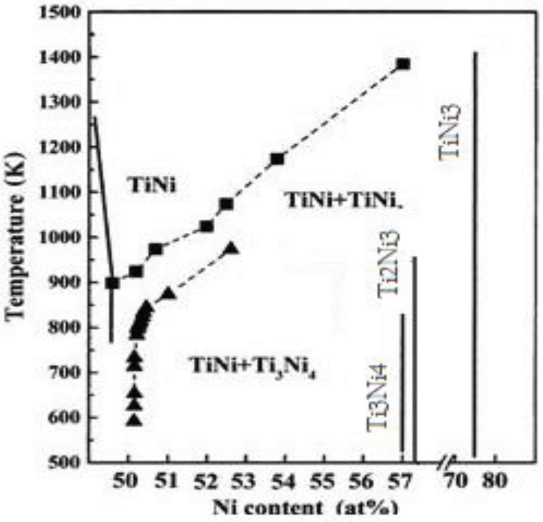

Figure 2.22 Portion of the phase diagram related to the aging treatment [76].

2.3.1. Resultant Microstructures

The austenite to martensite transformation temperatures are highly dependent on Ni content of the austenite. Aging treatment is applied in order to stabilize and modify transformation temperatures by adjusting the Ni-content of the NiTi matrix through a metastable equilibrium between Ti_3Ni_4 and NiTi phases [77]. From Figure 2.22, the composition of matrix which is in equilibrium with Ti_3Ni_4 can be estimated following to aging. During aging with formation of Ti_3Ni_4 precipitates, the nickel content of the matrix decreases. As a result of this, transformation temperatures increase until the metastable equilibrium is reached. After equilibrium is achieved the transformation temperatures are stabilized. Another important point is that the transformation temperatures achieved because of equilibrium between these two phases are composition independent. The only factor affecting these temperatures is the aging temperature. Upon examination of the solvus between Ti_3Ni_4 and NiTi, it is seen that higher aging temperatures results in a matrix with a higher nickel content.

However, this is a rough approach and does not completely explain the aging phenomena in Ni-Ti alloys because transformation temperatures change also with microstructural features like precipitation size, volume fraction and interparticle spacing [79].

As stated above, Ti_3Ni_4 phase has a rhombohedral crystal structure and this structure can more easily be understood by consideration of hexagonal axes [72]. In the B2 type matrix phase, (111) planes consist of alternate Ti and Ni hexagonal layers, and by such six layers a period is formed. The basal planes of Ti_3Ni_4 arrange in similar stacking but excess Ni atoms are distributed in each original Ti layers. Figure 2.23 shows the arrangement of Ni and Ti atoms in Ti_3Ni_4 and B2.

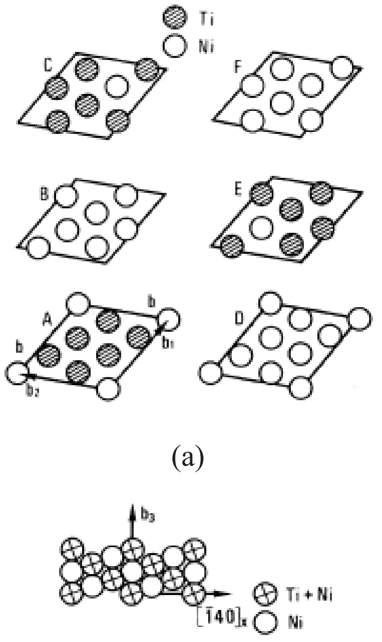

(a)

(b)

Figure 2.23 Arrangement of Ni and Ti in (a) Ti_3Ni_4 unit cell (b) B2 along <111> direction [72].

Lenticular (disc) shaped coherent Ti_3Ni_4 precipitates can form eight variants which grow on the {111} habit planes of the NiTi B2 [79]. Figure 2.24 is a TEM micrograph showing lenticular Ti_3Ni_4 precipitates labeled as p1, p2, p3 and p4 corresponding to the $(1\bar{1}\bar{1})$, $(\bar{1}1\bar{1})$, $(\bar{1}\bar{1}1)$, (111) plane groups, respectively.

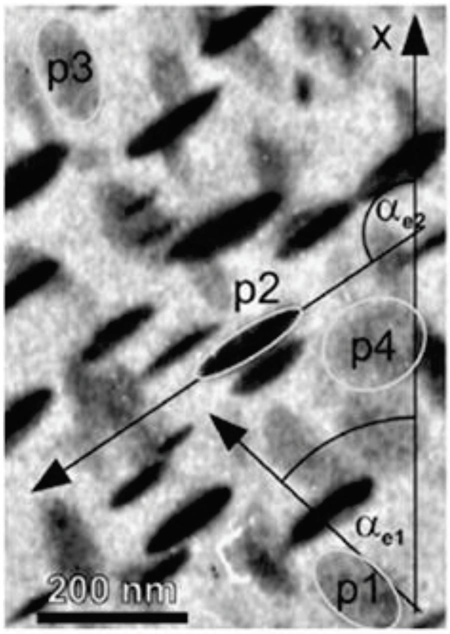

Figure 2.24 Experimental projections of Ti_3Ni_4 particle discs [79].

From the above discussion and lattice parameters, the strains in the B2 lattice created by formation of Ti_3Ni_4 can be calculated. Tadaki et.al. presented strains as -2.3% in the direction of habit plane normal; and -0.5% in the habit plane for fully coherent interface. The figure 2.25 schematically shows the strained lattice around a Ti_3Ni_4 precipitate [71].

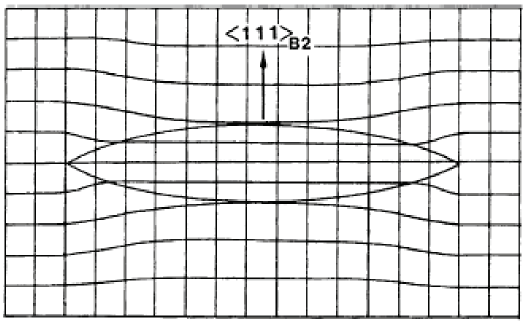

Figure 2.25 Schematic presentation of lattice distortion around a Ti_3 Ni_4 precipitate [71].

The interface characteristics are affected from the size of the precipitate. With increasing size of the precipitates the coherency loss starts and formation of interface dislocations take place [80]. The size of precipitates is also effective on the size of the strain field. As the precipitate grows, strain field enlarges since it compensates only for mismatch between precipitates and the matrix. In other words, the overall deformation is zero and as the maximum strain increases, the strain field gets smaller.

The shape of the strain field can be estimated from figure 2.26. The shape has a similar trend for both small and large precipitates. The maximum strain is not observed at the particle-matrix interface instead it is observed at a distance from the interface and after reaching maximum it continually decreases [80].

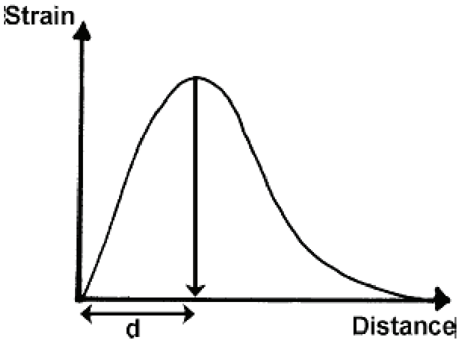

Figure 2.26 Shape of the strain field created by the presence of Ti_3Ni_4 precipitates along the direction perpendicular to or at a wide angle with the interface plane and close to the central area of the precipitate [80].

Recalling figure 2.24, at the tips, compression may be expected for providing the continuity of coherency due to the smaller interplanar spacing of precipitates, whereas at the side of the precipitates perpendicular to the central part of the interface, expansion is seen. [80].

2.3.1.1. Parameters Affecting the Resultant Microstructure

It is known that the driving force for precipitation is the degree of supersaturation. Thus, the rate of precipitation as well as the amount of precipitates to be formed increases with increasing Ni content. As aging time increases, due to growth governed by the square root time law, precipitate size and interparticle spacing increase. The effect of temperature in enhancing mobility during precipitation is exponential. On the other hand, with increasing temperature degree of supersaturation and in result driving force for precipitation is lowered. These competing effects of the two terms result in C shaped TTT diagrams.

Figure 2.27 summarizes the effect of temperature via microstructure of aged Ti–51 at % Ni single crystals. The number of precipitates subsequent to aging at lower temperatures is higher than that subsequent to aging at higher temperatures.

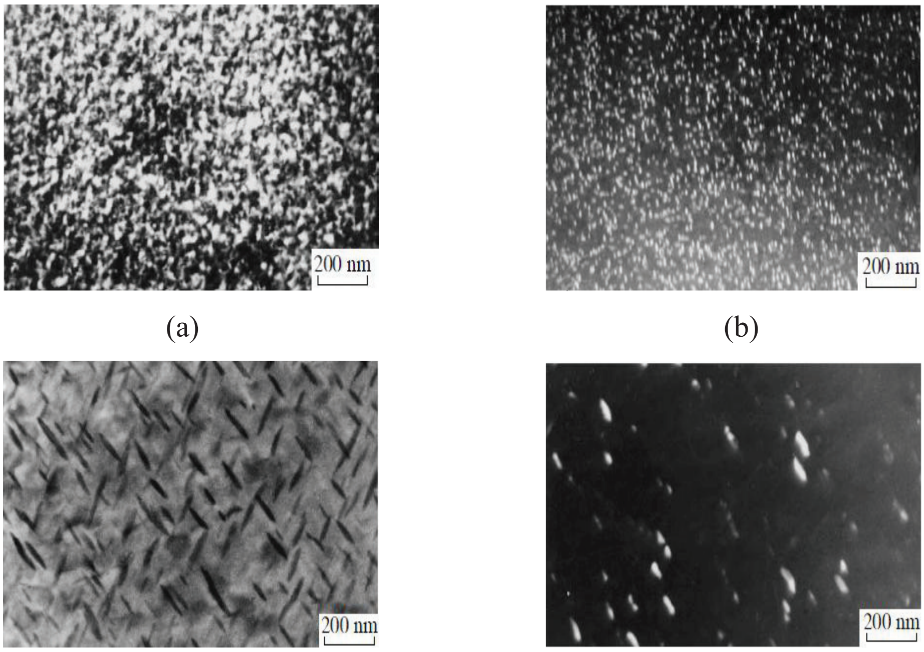

(a) (b)

(c) (d)

Figure 2.27 Microstructure of aged Ti–51 at. % Ni single crystals: (a, c) bright-field images, (b, d) dark-field images taken with a particle reflection, (a, b) after aging at 400 ^{o}C for 1 hour, (c, d) after aging at 500 ^{o}C for 1 hour [78].

2.3.2. Aging Induced $\mathbf{B2 \rightarrow R \rightarrow B19'}$ Transformation

The studies by Ren et. al. showed that the alloys with certain thermomechanical histories and compositions experience a decrease in resistance to {001}<100> shear which is equal to the resistance to the {001}<110> shear in cubic crystals. Actually, the shear stated latterly is the non-basal monoclinic shear required for formation of B19'. Thus, all binary and ternary NiTi-based alloys with different thermomechanical treatment histories have a tendency to transform into B19' martensite phase eventually [81].

Actually, R-phase, B19 and B19' martensites are possible candidate martensites of NiTi-based shape memory alloys following to any mechanical and thermal treatments. The candidates compete with each other in terms of intrinsic and extrinsic energies. In other words, lattice dynamics and resistance to the lattice distortion determines whether and which intermediate phase will form [81].

The conditions inducing formation of intermediate martensite phases should suppress the formation of B19'. Presence of fine Ti_3Ni_4 precipitates is one of these conditions inducing an intermediate martensite, namely R-phase [43]. The suppression of B19' martensite formation is not related to the any intrinsic energy change of the mentioned martensite or R-phase. This is obvious from the softening of c_{44} in the same manner prior to B19' and R-phase formation from the parent B2 phase [81]. To state differently, there is no change in the intrinsic stabilities of the competing martensite phases. So, the change in relative stability of the martensites should be the reason for the change in transformation path. In terms of precipitation, inducing of extra coherent strain energy with lattice distortion during martensitic transformations leads the change in relative stabilities. From a thermodynamical point of view, entropy change associated with martensitic transformation is

$$\Delta S = -\alpha \eta_M^2 \text{ [81]} \qquad (2.3)$$

Here η is the transformation strain at transformation temperature. Presence of minus sign in the equation reveals that martensitic transformations always result in decrease in entropy. Another important consequence; entropy change associated with a martensitic transformation is proportional to the square of the transformation strain.

With a rough approach, free energy versus temperature curve of the parent phase can be taken as a straight line with a slope of entropy (fig. 2.28). When the same approach is applied to the martensites, ΔS associated with the martensitic transformation will be equal to the difference between slopes of curves of parent and martensite. Smaller ΔS means the martensite free energy line is closer to that of the parent.

The transformation strains associated with the $B2 \rightarrow R$ transformation and $B2 \rightarrow B19'$ transformation are approximately 1% and 10%, respectively. So, the entropy change associated with the former transformation is smaller than the entropy change associated with latter one. Since, the entropy change determines the how close will be the free energy versus temperature line to that of parent phase, it is expected that free energy line of R-phase will be closer to the that of parent phase compared to the one belongs to B19'. From Figure 2.28 given below, the transformation sequence comes out as $B2 \rightarrow R \rightarrow B19'$. In short, if transformation is set to be multistep, the sequence will follow the sequence of increasing transformation strain sequence [81,82].

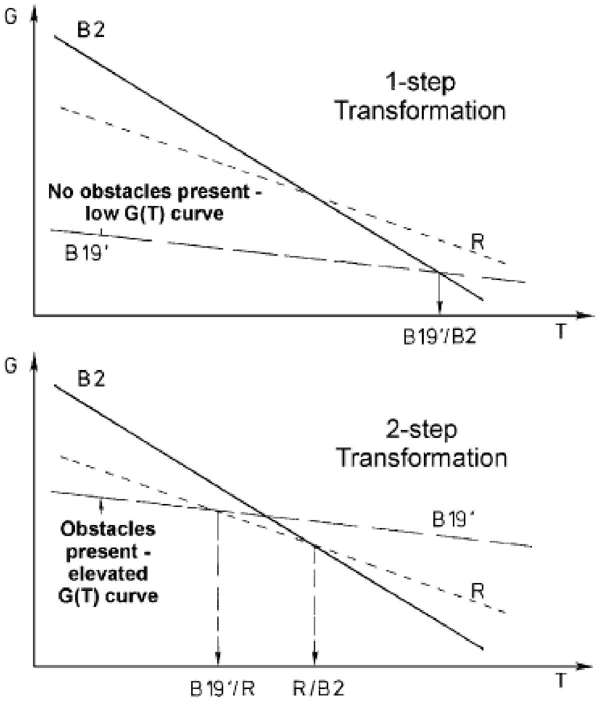

Figure 2.28 Schematic representation of transformation paths of Ti-Ni based alloys in relation to relative stability of R-phase and B19'with B2 parent phase [82].

Transformation temperatures (A_s, A_f, M_s, M_f) change with changing precipitate size and volume fraction in aged NiTi alloys, whereas, R-phase transformation start temperature is not highly dependent on the mentioned microstructural features. Also, the effect of precipitates is not in the same manner on all of the transformation temperatures. Without application of stress, the driving force for martensitic transformations is required for overcoming the energy generated by elastic and surface energies, and friction forces during interface or phase boundary motion [78]. To formulate;

$$-\Delta G_{ch}^{A-M} + \Delta G_{rev}^{A-M} + \Delta G_{fr}^{A-M} = 0 \qquad (2.4)$$

$$-\Delta G_{ch}^{M-A} + \Delta G_{rev}^{M-A} + \Delta G_{fr}^{M-A} = 0 \qquad (2.5)$$

Here, the chemical energy term, ΔG_{ch} is the driving force required for martensitic transformation whereas, the reversible energy term, ΔG_{rev} consists of elastic and surface energies. These energies depend on the volume fraction of the martensites. On the other hand, frictional energy term stands for the friction stresses required for interface motion and plastic relaxation of the stored elastic energy via dislocation formation. In other words, this term refers for dissipated energy during martensitic transformation. When the material is single phase, i.e., there are no precipitates, the change in martensitic transformation is determined by Ni at.% of the matrix. However, when Ti_3Ni_4 is precipitated, the change in martensite start temperature is represented as [83-85] ;

$$\Delta M_s = \frac{\delta T_o}{\delta C_{Ni}} \Delta C_{Ni} - \frac{\delta \Delta T}{\delta \Delta \sigma_{0.1}} \Delta \sigma_{0.1} - \frac{\delta \Delta T}{\delta \Delta \sigma_i} \Delta \sigma_i + \frac{\Delta S}{\varepsilon_o} \Delta \sigma_{in} \tag{2.6}$$

In this formula, the first term shows the change in martensitic transformation start temperature with change in the composition of the matrix and since Ni at.% decreases with the formation of Ti_3Ni_4, it has a positive sign, meaning that it causes an increase in the transformation temperature. The Ni content of the matrix subsequent to aging is given as [86,87]

$$C_{Ni}^{'} = \frac{C_{Ni} - Af}{1-f} \tag{2.7}$$

Here C_{Ni} is the composition of the matrix prior to aging, whereas A is the Ni at.% of the Ti_3Ni_4 which is approximately 56 at.%Ni and f is the volume fraction of the precipitates.

The second term, decreasing the transformation temperature, stands for the increase in yield strength of B2 matrix as a result of precipitation. The increase in the strength of B2 matrix can be formulated as [85, 88]

$$\Delta \sigma_{0.1} = \sigma_{0.1}^{aged} (B2) - \sigma_{0.1}^{sp} (B2) \tag{2.8}$$

The third term again decreasing M_s decreasing the transformation temperature shows the increase in required supercooling due to increase in elastic energy associated with precipitates which do not go through martensitic transformation.

As the strength of B2 phase increases, resistance to the interface motion during martensitic transformation increases [78]. So, the second term does not cause a decrease in the stability of R-phase because the lattice deformation associated with R-phase is very small (1%) [38,78,80]. Also, precipitates does not cause a considerable increase in required supercooling for $B2 \rightarrow R$ transformation, because the increase in undercooling stems from the additional elastic energy which is generated when the precipitates elastically deform in order to keep the coherency with the new martensitic matrix [89]. In addition, in NiTi alloys with Ti_3Ni_4 precipitates instead of type II twinning compound twin is observed, and the surface energy required for formation of compound twins is also taken into consideration under this term. The compound twins are actually generated in order to compensate the elastic deformation of precipitates with martensitic transformation. Figure 2.29 shows the formation of compound twins with martensitic transformation in an aged NiTi crystal

The final term in equation 2.6 shows the increase in martensitic start temperature due to easier nucleation of martensites. Since the local internal stresses ($\Delta\sigma_{in}$) due to differences between lattice parameters of B2 matrix and precipitates make the particle matrix interface preferable nucleation site for the martensite plates. As it is stated above, second and third terms do not play an important role in determination of R-phase formation start temperature, however the final term has a strong influence. Such that Bataillard et.al. observed that R-phases preferably forms around the precipitates [90].

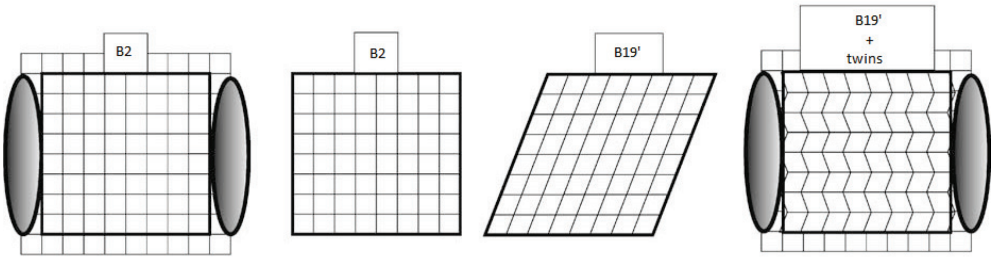

Figure 2.29 Schematic diagram for the formation B19' and compound twins in the space between tow Ti_3Ni_4 precipitate [78].

The effect of precipitates on transformation behavior is not straightforward. Actually, according to the microstructural features, namely precipitate size, interparticle spacing and fraction of the precipitates, the effect shows variations. The importance in those microstructural features is actually related to the increase in surface energy due to requirement of generation of compound twins, additional stored energy with martensitic transformations induced by elastic deformation of the precipitates and increase in resistance to the interface motion during martensitic transformations as a result of presence of precipitates. Above, these are stated as effects suppressing martensitic transformation and causing the appearance of R-phase prior to formation of B19'. However, these influence also other transformation temperatures. The additional elastic and surface energies cause the appearance of an energy barrier for reverse transformation. This energy barrier is required for detwinning of compound twins and the overcoming this is only possible with remarkable overheating. When detwinning takes place, the elastic energy is observed to increase in the area between precipitates and this causes a sudden increase in the kinetics of the reverse transformation. In other words, the stored elastic energy is released via detwinning [78]. Figure 2.30 summaries the effect of precipitate size and volume fraction of precipitates (f) on the transformation temperatures. As it is seen from the figure, R-phase transformation temperatures weakly depend on the size and fraction of precipitates. Although effect on other transformation temperatures are larger compared to those related to the R-phase, the influence is not same on all other transformation temperatures. When the volume fraction of precipitate is around 4% or 5% the start and finish temperatures of $R \rightarrow B19'$ transformation (M_s and M_f, respectively) increases with increasing precipitate size from 25 to 100 nm indicating that the first and final terms of the equation 2.6 are dominant. In other words, the strengthening of the matrix and stored elastic energy has less influence on transformation temperature than decrease in Ni content of the matrix and local internal strains created by precipitates.

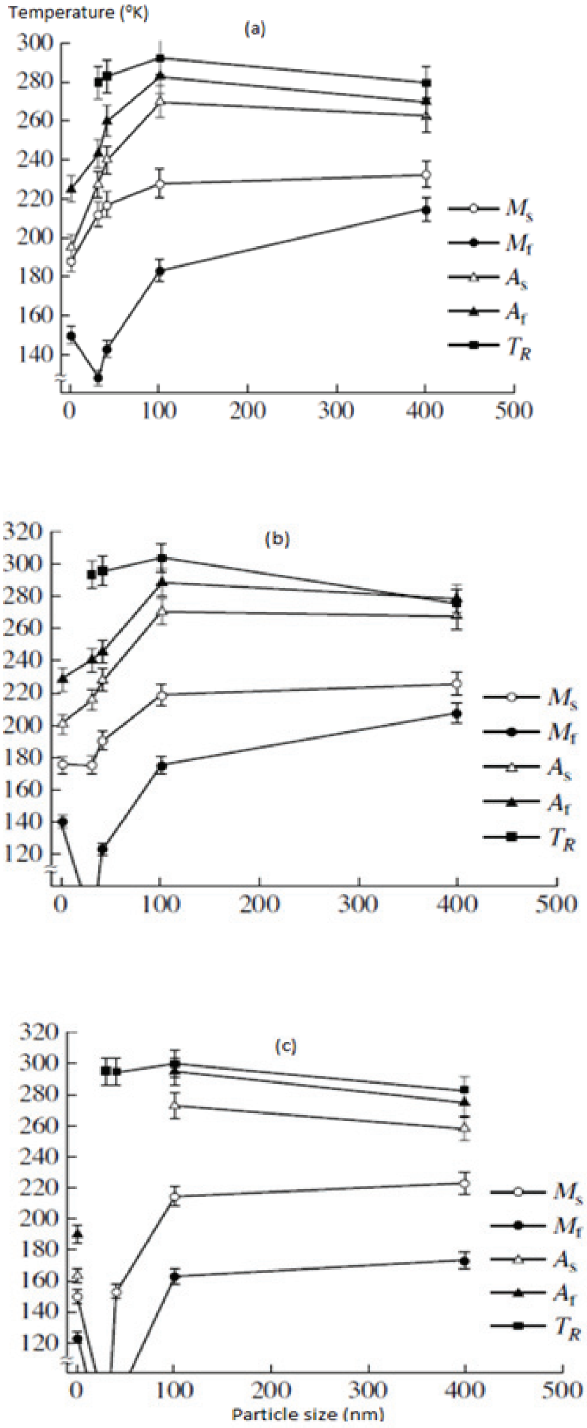

Figure 2.30 Change in transformation temperatures with precipitate size for different volume fraction of precipitates in Ti–(50.7–51.0) at % Ni single crystals (a) Ti–50.7 at % Ni, (f= 4%), (b) Ti–50.8 at % Ni (f = 5%), and (c) Ti–51.0 at % Ni (f= 9%) [78].

The increase in these temperatures with increasing precipitate size from 100 nm to 400 nm declines due to the coherency loss of the precipitates after exceeding the size of 100 nm [91]. The relatively rapid increase of the transformation temperatures can be explained as that with the further growth of the coherent precipitates, a larger volume of the matrix is affected by the induced local strain fields [91]. In short, when the precipitates are smaller and coherent, the increase in transformation temperature is associated with compositional and strain related effects. However, after the loss of coherency the dominating effect on transformation temperature becomes the decrease of nickel content of the matrix. As a result of this, the change in transformation temperatures is not different from that of single phase NiTi with respect to nickel content. When the fraction of the precipitates is higher (f=9%) and the precipitate size is smaller, the interparticle distance decreases below 40 nm. In result, $R \rightarrow B19'$ is suppressed to temperatures lower than 77 ^{o}K, because when the interparticle distance becomes lower than 40 nm, it also becomes smaller than the critical nucleus size of the B19' crystals which is 15-50 nm [78]. In addition, the study of Panchenco et.al. revealed that the maximum compound twin density is observed for the mentioned precipitate size [78]. Finally, for almost all given fraction of precipitates, reverse transformation start and finish temperature change in a qualitatively same manner.

When the interface between precipitates and matrix is semicoherent, they still trigger the R-phase transformation. However, when they completely lose their coherency, instead of an intermediate R-phase transformation a single step transformation takes place [92]. Also, in this state, the decrease in transformation temperature with increasing aging is also observed when the latent heat of transformation is increased. By recalling of TTT diagram for precipitation of Ni-rich NiTi alloy (figure 2.22), this can be interpreted as dissolution of Ti_3Ni_4 particles and formation of a more stable one which is Ti_2Ni_3 [92]. However, due to higher nickel content of the latter one an increase in transformation temperature is expected. The presence of a reverse situation shows that the dissolution of the Ti_3Ni_4 has faster kinetics than the formation of Ti_2Ni_3.

2.3.3. Aging Induced Multistep Transformation

In aged Ni-rich NiTi shape memory alloys instead of two step transformations, it is possible to observe three or even more step transformations. The reason behind this phenomenon has been tried to be explained by many studies. Bataillard et.al studied the multi-step transformation in a 51.14 at.% Ni-Ti alloy via differential thermal analysis and in-situ TEM. They stated that transformation in multi-step is related to the local stress fields created by coherent Ti_3Ni_4 precipitates [90]. They observed that R-phase clearly nucleates around precipitates and grows through the matrix, whereas during martensite with B19' crystal structure formation, after the martensites formed around precipitates, the transformation does not continue in the surrounding matrix because formation of martensite results in a stress relaxation and since the transformation is induced by local stress fields, it stops with relaxation until the temperature is decreased more. As a result of this, upon cooling a single step $B2 \rightarrow R$ transformation is followed by a two step $R \rightarrow B19'$ transformation. Figure 2.31 summaries the model they proposed. The stress around precipitates are calculated as 76 MPa, which creates a 20 ^{o}K difference in martensitic transformation temperatures of B19' whereas, it creates only 5.7 ^{o}K for R-phase transformation between stressed and unstressed region. Bataillard et.al. denoted that the change in R-phase transformation temperature is out of the resolution limits of their DTA equipment so that they could not detect the R-phase transformation associated with the unstressed regions. Upon heating, the reverse transformation starts in the regions which are not affected by the stress fields of precipitates. Firstly, the mentioned regions transform from B19' to B2. Upon further heating, the stressed regions transformed form B19' to R - phase and R- phase to B2, successively.

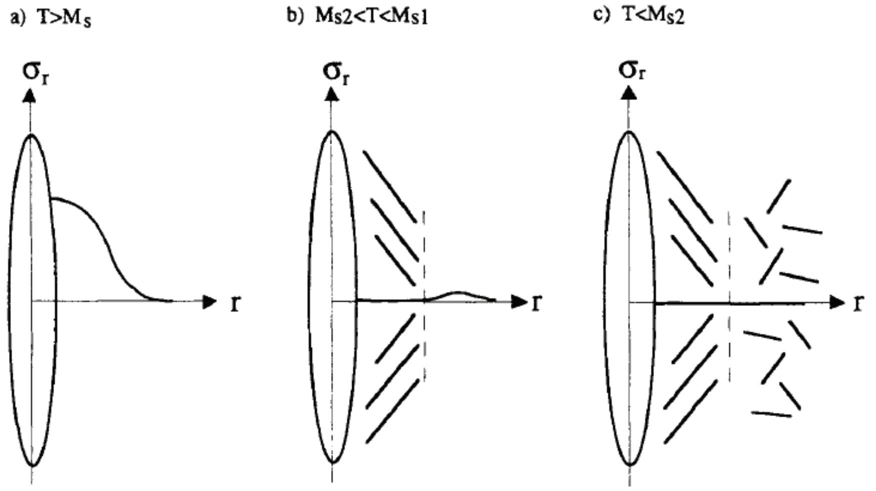

Figure 2.31 The model proposed for formation of martensitic phases around precipitates [90]

Allafi et.al. explained the multi step transformation with a similar approach to the Bataillard et.al. [93]. The only difference is that they aged the materials for different aging times and suggested that multistep transformation is observed after intermediate aging times (10 and 50 hours) due to the compositional inhomogeneity in the matrix associated with precipitation. The model they proposed is summarized in figure 2.32. The first row belongs to short aging time (1 hour), second and third row belongs to intermediate aging times (10 and 50 hours, respectively). The third row represents the aging for long times (100 hours). The first column shows the concentration profile between two precipitates, the second column is the transformation temperatures, the third and fourth columns are local latent heats of the reactions and resulted DSC curves, respectively. The schematic figure explains that for short aging times, since the precipitates are small, they do not consume much nickel and as a result of this, R-phase starts to form at precipitate-matrix interface when the temperature is reached to the highest R_s , but since the transformed volume is so small and the change between minimum R_s (labeled as T_o^R) and the maximum R_s is very near, it cannot give a distinct peak in the differential scanning calorimetry curve. As a result of this, the first transformation peak is observed at the minimum R_s temperature. At the martensitic transformation temperature which determined without the consideration of suppressing effects of precipitates ($T_o^{B19'}$), there is no transformation, since no undercooling is given. The temperature where the martensitic transformation starts given as M_s. When intermediate aging times are applied, R-phase transformation starts at the maximum R_s at both sides of the graph representing growth from two precipitates to the interparticle space. The transformation to B19' does not start until the maximum M_s is reached. After the region near precipitates transform, the transformation stops and cannot continue until a further undercooling is given. After long aging times, since the compositional homogenization maintained between precipitates a regular two- step $B2 \rightarrow R \rightarrow B19'$ is observed.

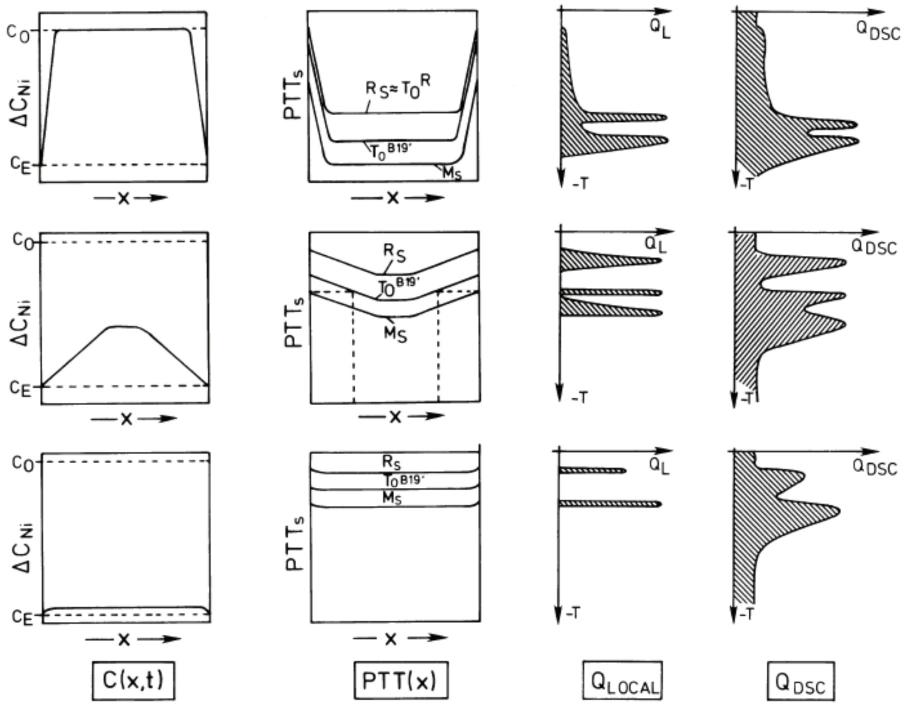

Figure 2.32 The model proposed by Allafi et. al [93] for explanation of multi step transformation.

Another explanation of the multiple stage transformation was again declared by Allafi et.al. Their studies with 50.7 at. % Ni-Ti alloy aged at 500 ^{o}C with and without stress application stress for various times revealed that again at intermediate aging times for both conditions multistep transformation is observed [94]. They showed that as aging time changes not only size and interparticle spacing changes but also their distribution changes when the samples aged without application of stress. The Figure 2.33 (a) and (b) show the microstructure of the samples aged freely at 500^{o}C for 1 hour and 10 hours, respectively. After 1 hour of aging the precipitates are located only on and near grain boundaries. With prolonged aging time, as expected there is an enormous increase in size of precipitates. In addition, although the most of the grains are precipitate free, large precipitates form an irregular network inside of the grains around the defects. In addition, they have stated that the variants of precipitates changes according to their spatial location. The precipitates on and near grain boundaries grow in only one variant, whereas it is possible to observe two different variant of the precipitates growing in the grains. The differential scanning calorimetry curves with the associated microstructures are also given in the figure 2.33. The columns c and d show the transformations upon cooling and heating, respectively, for solution annealed, 1 hour and 10 hours aged alloys. The last peak upon cooling for both aging times and the single peak of the solutionized material are at the same temperature. This transformation is $B2 \rightarrow B19'$. This transformation is believed to be taking place in the regions which are not affected by the presence of precipitates. The first peak upon cooling after 1 hour of aging is a mixture of $B2 \rightarrow R$ and $R \rightarrow B19'$ transformations. Since the precipitate volume is small and so is the region transformed under the effect of precipitates, the peaks of these two transformations cannot be differentiated. On the other hand, the first two peaks upon cooling of 10 hours aged specimens belong to regular $B2 \rightarrow R \rightarrow B19'$ transformation. Upon heating the first peaks of the aged specimens and the single peak of the solution annealed specimen are at the same temperature and represents the reverse transformation from B19’ to B2 in the unaffected regions. The regions with precipitates go through the same transformation at different temperature due to local stress created by precipitates. Intermediate R-phase does not form upon heating because transformation strains for transformation from B19’ to R-phase or B2 are almost same. In the same study, the multistep transformation in stress assisted aged specimens were associated with the different variants of precipitates along grain boundaries and grain interiors since precipitate size and distribution is almost homogeneous throughout the microstructure [94].

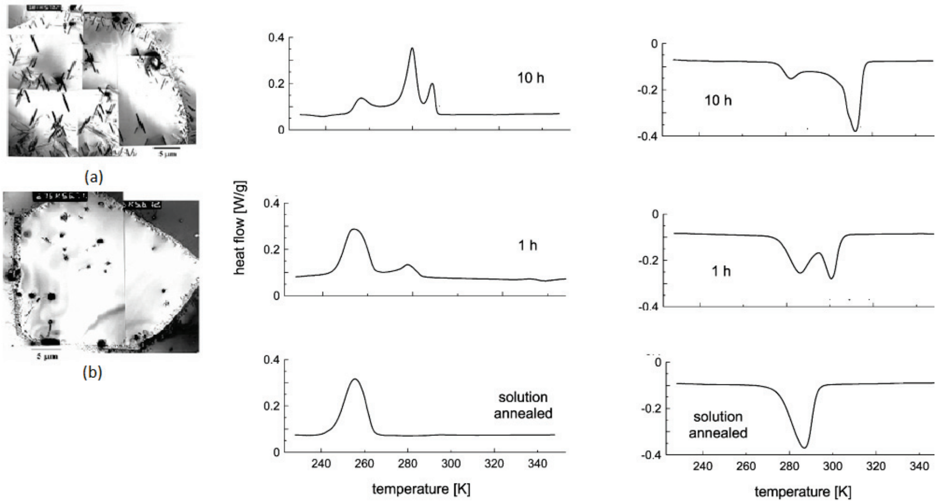

(c) (d)

Figure 2.33 The microstructures of the specimens aged at 500°C for (a) 1hour and (b) 10 hours with (c,d) associated differential scanning calorimetry curves [94].

Another study to explain the reason behind the multistep transformation was done via in-situ transmission electron microscopy by Dlouhy et.al. [95]. The findings were parallel to the results of Allafi et.al. [94]. Their study is summarized in Figures 2.34 and 2.35. Figure 2.34 (a) shows the phase transformation in a 50.7 at.% Ni-Ti alloy aged at 500 °C for an hour. Before any transformation upon cooling at room temperature, it is seen that the microstructure is characterized by a heterogeneous distribution of precipitates with average size of 230 ± 150 nm near grain boundaries. Besides this, the matrix is fully B2. Upon cooling to -5°C, the region near precipitates transformed into R-phase, whereas other regions remained as B2. With decrease of temperature to -20 °C, all B2 and R-phase regions transform into B19'. Therefore, the first peak upon cooling is $B2 \rightarrow R$, whereas the second peak is a mixture $R \rightarrow B19'$ and direct $B2 \rightarrow 19'$. The figure 2.34 (b) shows the temperature induced transformation of the alloy with the same composition which is aged at 500 °C for 10 hours. Before any transformation, the microstructure consists of large precipitates, size of which is 900 ±340 nm. The precipitates near grain boundaries are dominated the volume of the precipitated region, whereas the ones in the grains form an irregular network around the Ti_4Ni_2O particles. The transformation is three-step upon cooling. The first step is formation of R-phase from the parent B2 around the grain boundaries between precipitates. On the other hand, the second peak shows the transformation of R-phase into B19’ in the space between precipitates. The final peak shows the transformation from B2 into B19’ of unstressed region, in other words regions which are not affected by the presence of precipitates.

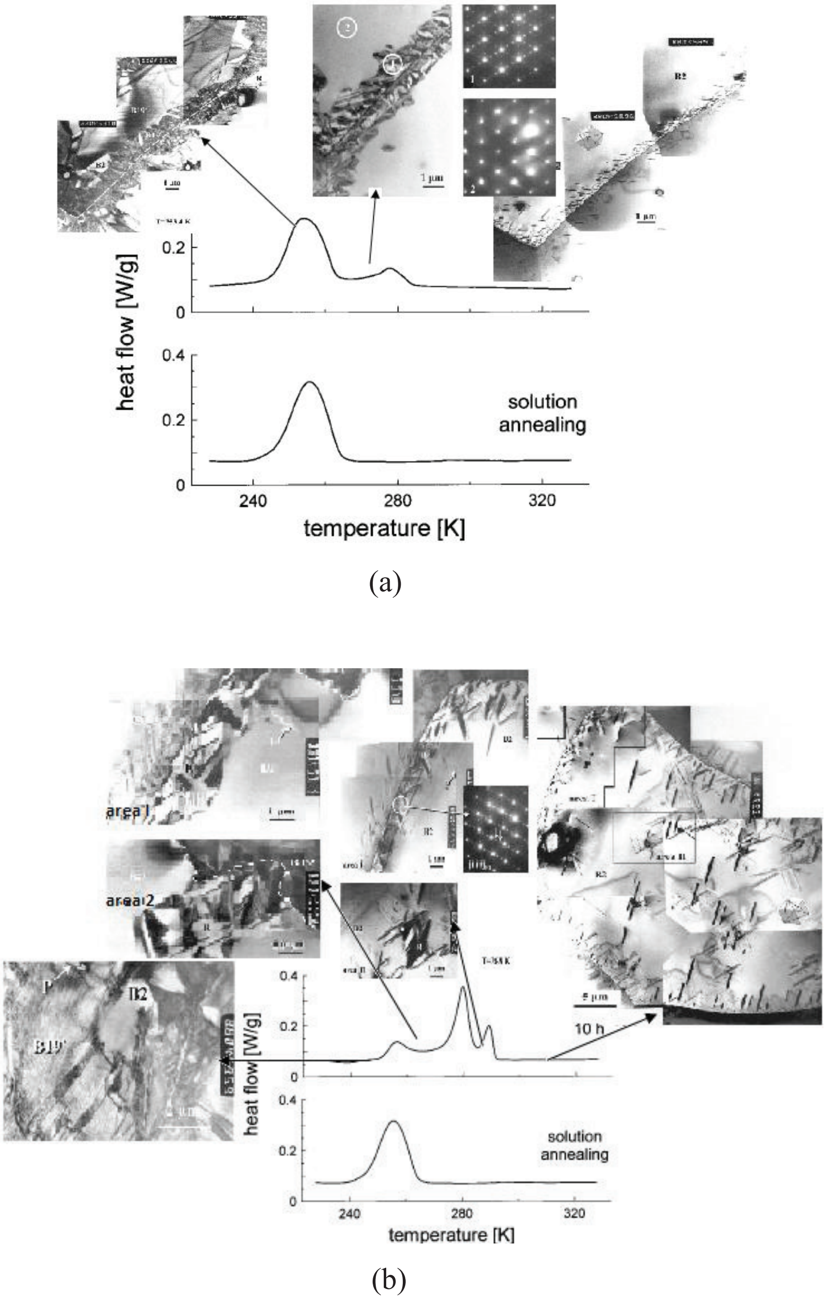

(a)

(b)

Figure 2.34 The microstructures and differential scanning calorimetry curves of the specimens aged at 500^{o}C for 1hour (a) and 10 hours (b) at various temperatures in transformation ranges upon cooling [95].

Figure 2.35 shows the reverse transformation behavior of the same materials. For the alloy aged for an hour and 10 hours, the transformation upon heating is not different from each other. The first peak is the transformation of precipitate free regions from B19’ into B2. The second peak belongs to same transformation of near precipitate regions. Just like Allafi et.al, they stated that the multistep transformation is a result of inhomogeneous distribution of precipitates between grain boundaries and grain interior. In addition, they added that the other explanation can be valid when the distribution is homogeneous; however, when the precipitates are not distributed evenly the other explanations are ruled out [95].

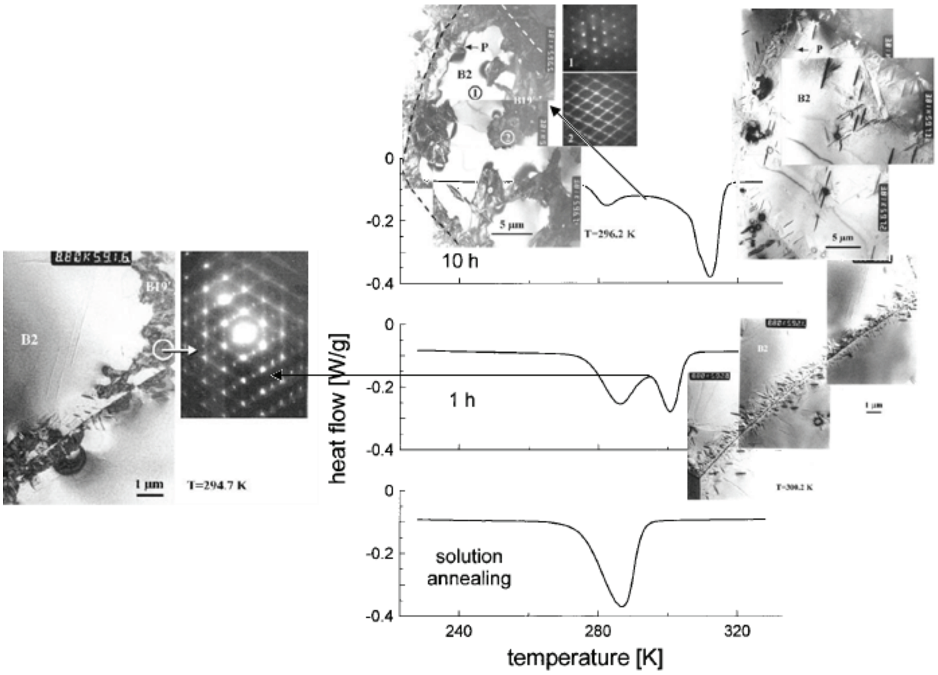

Figure 2.35 The microstructures and differential scanning calorimetry curves of the specimens aged at 500°C for 1hour (a) and 10 hours (b) at various temperatures in transformation ranges upon heating [95].

Fan et. al. explained the multistep transformation as a result of large scale inhomogeneities, in other words, grain boundaries like Allafi et.al and Dlouhy et.al. [94, 95]. However, they also showed that the effect of grain boundaries is composition dependent and ineffective when Ni content is high [96,97]. So, presence of grain boundaries is a necessary condition for multistep transformation but it is actually not sufficient. The main parameter determining the transformation behavior is distribution of Ti_3Ni_4 precipitates between grain boundary and grain interior. The main difference between specimens with low nickel content and high nickel content is actually rate of precipitation. Recalling that grain boundaries are preferred sites for nucleation, effect of composition on distribution of precipitate can be understood from the figure 2.36. Figure shows that at low supersaturation, grain boundary nucleation rate is significantly higher than grain interior, whereas at high supersaturation the differences in rates of nucleation at grain boundary and grain interior is not such obvious.

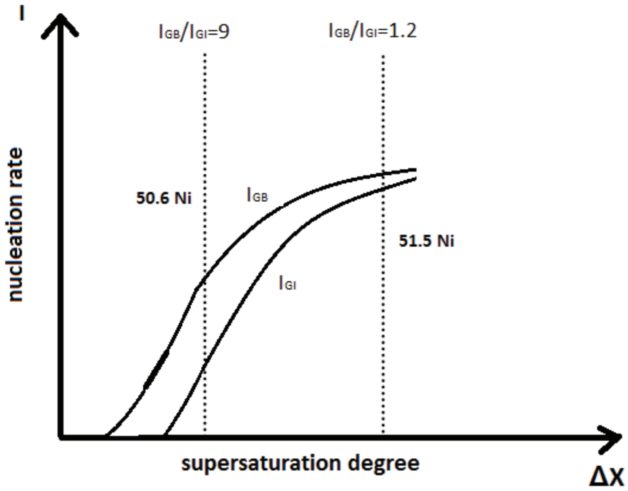

Figure 2.36 Schematic illustration of the relation between nucleation rate and supersaturation degree in grain interior region and grain boundary region. Supersaturation degree ΔX is defined by the solute (Ni) concentration beyond its solubility limit in B2. Ti–Ni phase at given aging temperature. The nucleation rate at grain boundary and at grain interior is indicated by I_{GB} and I_{GI}, respectively [96].

There are actually competing factors in determining the distribution of Ti_3Ni_4 precipitates between grain boundary and grain interiors. The first one is presence of grain boundaries which favors heterogeneous distribution whereas; degree of supersaturation as being the second one favors a homogeneous distribution. By using the proposed mechanism above the multistep and two-step transformation is understandable. When the nickel content is low preferential grain boundary nucleation is dominant. As a result, grain boundary regions undergo $B2 \rightarrow R \rightarrow B19'$ transformation, while precipitate free grain interiors undergo direct $B2 \rightarrow B19'$ transformation. In this three step transformation the first peak upon cooling corresponds to $B2 \rightarrow R$, the second corresponds to $B2 \rightarrow B19'$ and the final one corresponds to $R \rightarrow B19'$. On the other hand, if nickel content is high, distribution of precipitates is homogeneous. So, two step transformation, $B2 \rightarrow R$, $R \rightarrow B19'$ is observed. Figure 2.37 given below summaries effect of nickel content and aging time on the size and distribution of precipitates. It also explains both three-stage and two-stage transformation behavior of supersaturated Ti–Ni solid solution. In the figure, $C_{initial}$ and C_{aged} curves represent the Ni profile of initial (as-quenched) state and that after aging, respectively. GB denotes grain boundary.

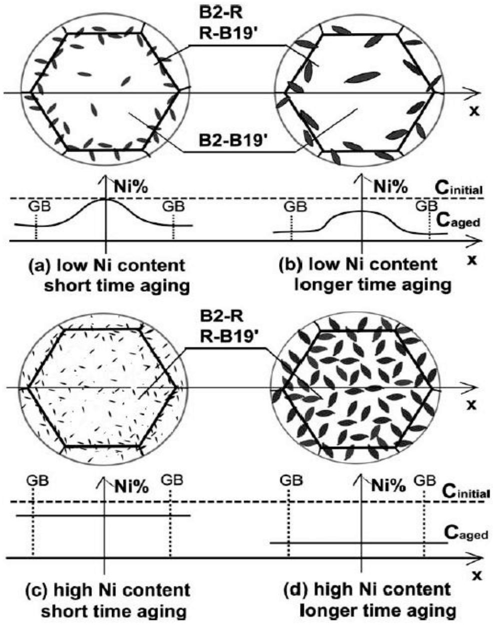

Figure 2.37 A unified model for explaining the microstructure evolution at low Ni supersaturation (a and b) and high Ni supersaturation (c and d) [96].

Michutta et.al showed that it is possible to observe multistep transformation in single crystal NiTi alloy with a homogeneous distribution of Ti_3Ni_4 precipitates [98]. They applied various aging conditions to a 51.3 at. % Ni-Ti alloy to form different microstructures. The transformation behavior is changed between two-step and three-step according to interparticle distance. When it is smaller than 200 nm, 2-step transformation is observed. The first step is the formation of R-phase. R-phase grows continuously from particle-matrix interface through the matrix between precipitates. On the other hand, the second step is the growth of B19' with rapid jumps in a manner which is called burst-like. When the interparticle distance exceeds 200 nm, the transformation is completed in three steps. Again, the first step is formation of R-phase without showing any difference with the smaller interparticle spacing. On the other hand, the $\mathrm{R} \to \mathrm{B19'}$ transformation splits into two stages. Firstly, B19' forms in the precipitate matrix interface. Following to this, the interparticle matrix transforms from R-phase to B19' [98].

Another study on single NiTi crystals showing multistep transformation was done by Johnson et. al. According to their findings, the single crystals with low Ni (50.1at Ni) content shows a four step transformation upon both cooling and heating whereas the ones with high Ni content (50.8 at.% and 51.5 at.%) two-step or one-step transformation is observed [99]. They stated that in single crystals dendrites and low-angle tilt boundaries are present as defects and their presence is related to the compositional variations. When the Ni content is low, compositional variations lead to formation of precipitate free regions during aging. As a result of this, multistep transformation is observed. Regions with precipitates go through $\mathrm{B2} \to \mathrm{R} \to \mathrm{B19'}$ whereas precipitate free regions transforms into B19' from B2 directly. On the other hand, when the Ni content is high, in spite of the defects a significantly more homogeneous distribution of precipitates is observed. The two-step transformation is $\mathrm{B2} \to \mathrm{R} \to \mathrm{B19'}$. The single peak observed in some aged NiTi single crystals with high Ni contents is $\mathrm{B2} \to \mathrm{R}$ and the second peak associated with $\mathrm{R} \to \mathrm{B19'}$ is suppressed below detection limits [99].

Zheng and his co-workers summarized the effects aging temperature and time for a 51.0 at.Ni% [92]. According to their findings the transformation behavior evolved through five different stages. Figure 2.38 shows these regions and corresponding schematic microstructures (a and b, respectively). In the first region, single step $\mathrm{B2} \to \mathrm{B19'}$ transformation is observed after aging at low temperatures and/or for short time. Following the aging under these conditions, instead of precipitation, atomic arrangements as a precursor of precipitation is expected. Going to higher aging temperatures or longer aging times, only $B2 \rightarrow R$ is observed along the grain boundaries where the precipitation of small sized Ti_3Ni_4 took place. On the other hand, transformation of precipitate free grains from B2 to B19’ is believed to be suppressed. In region three which can be named as intermediate aging times and temperatures, a homogeneous distribution of coherent Ti_3Ni_4 precipitates is achieved and as a result of this two-step $B2 \rightarrow R \rightarrow B19'$ transformation is observed. When the higher temperatures or prolonged aging times are chosen as conditions, formation of more stable intermediate precipitates (Ti_2Ni_3) takes place without fully elimination of Ti_3Ni_4 precipitates. As a result of a heterogeneous microstructure is obtained. Multistage transformation behavior is observed in result of such a microstructure. The regions where coherent precipitates present go through $B2 \rightarrow R \rightarrow B19'$ transformation, whereas matrix between large incoherent Ti_2Ni_3 precipitates go through $B2 \rightarrow B19'$ transformation. In the figure M1 stands for B19’ transformed from R-phase and M2 stands for B19’ formed directly from B2. In the fifth region where the dissolution of Ti_3Ni_4 is completed and only Ti_2Ni_3 precipitations are present, single stage $B2 \rightarrow B19'$ takes place [92].

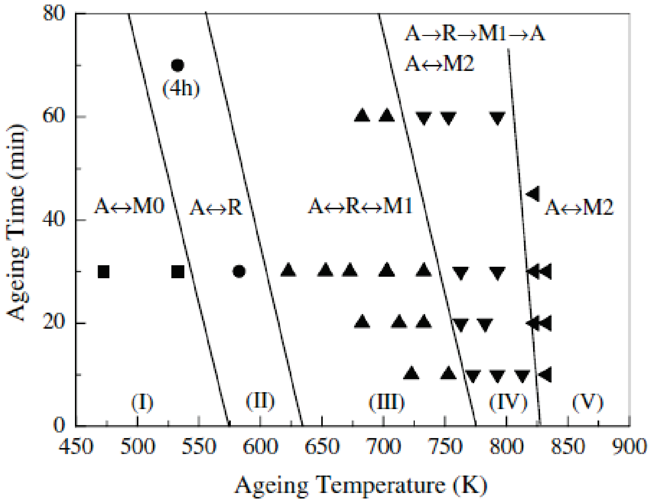

(a)

Figure 2.38 Effect of aging time and temperature on (a) transformation behavior and (b) microstructures of a 51.0 at. %-Ti alloy [92].

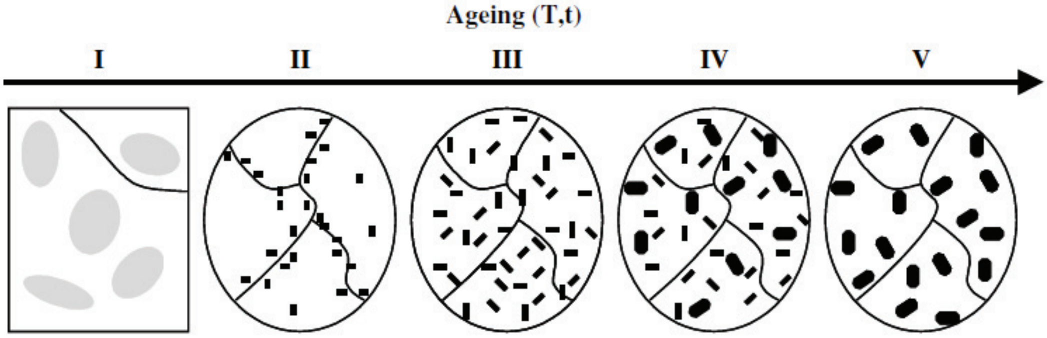

(b)

Figure 2.38 (continued)

Besides these studies, there are different approaches for explanation of multistep transformation observed in Ni-rich precipitate hardened NiTi alloys. Fujishima et.al studied the effect of solutionizing and aging atmosphere [97]. Actually, the reason behind the observation of multistep transformation was explained as the non-homogeneous distribution of precipitates, which can be avoided by the inhibition of the evaporation of Ni or Ti and oxidation of Ti. They declared that with better atmosphere conditions which can be obtained by vacuum, using of Ni and/or Ti foils and Ti getter, the difference between grain boundaries and interiors with respect to distribution and size of the precipitates decrease and even diminishes. The different heat treatment atmospheres and obtained thermally induced transformation behavior as a result of these are shown in Figure 2.39. In the figure, the first letter on the DSC curves represents the solutionizing atmosphere while the second one shows the aging atmosphere. From the figure, it is seen that when the vacuum, Ni/or Ti foil and Ti getter applied alone, they are not sufficient for providing homogeneous distribution of precipitates and in result hindering for multistep transformation.

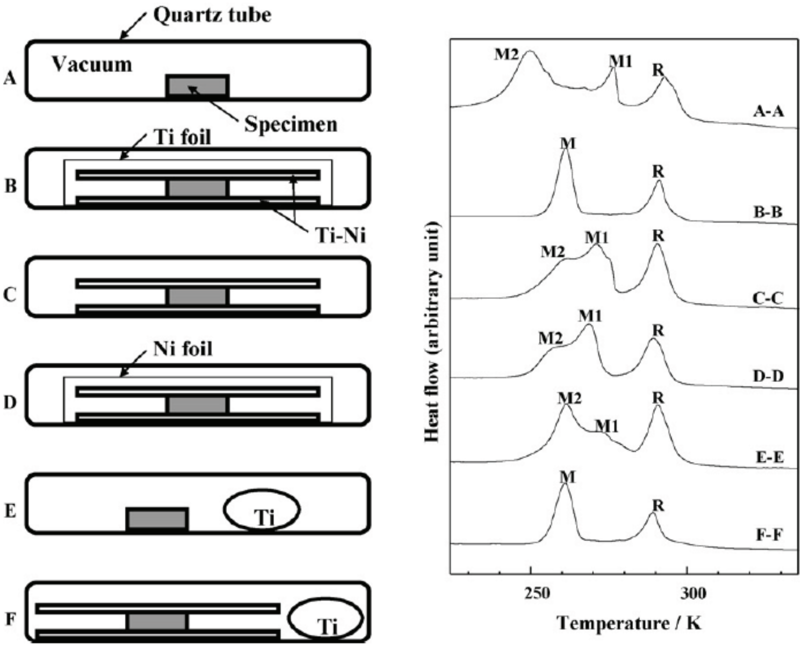

Figure 2.39 Schematic representation of heat treatment conditions with corresponding DSC cooling curves of Ti–50. 6 at.% Ni alloy solutionized at 1000^{o}C for 1 hour and subsequently aged at 500 ^{o}C for 2 hours [97].

Although many studies claim that multistep transformation is related to the formation of B19' in two steps [90, 92-102], it is possible to observe such transformation behavior as a result of formation of R-phase from B2 in two steps [103]. The study which is carried out by Kim et.al revealed that presence of very fine precipitates with size various between 2 nm to 40 nm leads to two-stage R-phase transformation [103]. The two R-phase transformations are determined by their very low thermal hysteresis (5-6 ^{o}C). According to their DSC results, the first R –phase transformation takes place around Ti_3Ni_4 precipitates whereas the second takes place at regions away from precipitates, because for shorter aging times, the dominant one is the second R-phase transformation with higher intensity compared to the first one. With prolonged aging time as expected the regions which are not affected by presence of precipitates decreases and so does the intensity of the second R-phase transformation, while the intensity of the first one increases. The DSC curves of the specimens aged for different times at 200 ^{o}C and 300 ^{o}C upon cooling is given in figure 2.40 a and b, respectively. In Figure 2.41, the microstructures of the specimens showing two–stage R-phase transformation can be seen.

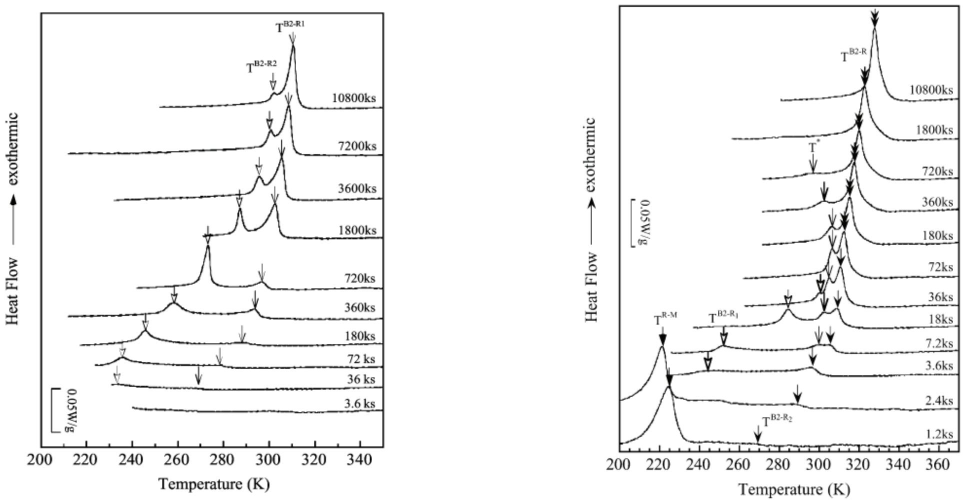

(a) (b)

Figure 2.40 DSC cooling curves of the 50.9 at. % Ni -Ti alloys aged for various times at (a) 200 °C and (b) 300 °C [103].

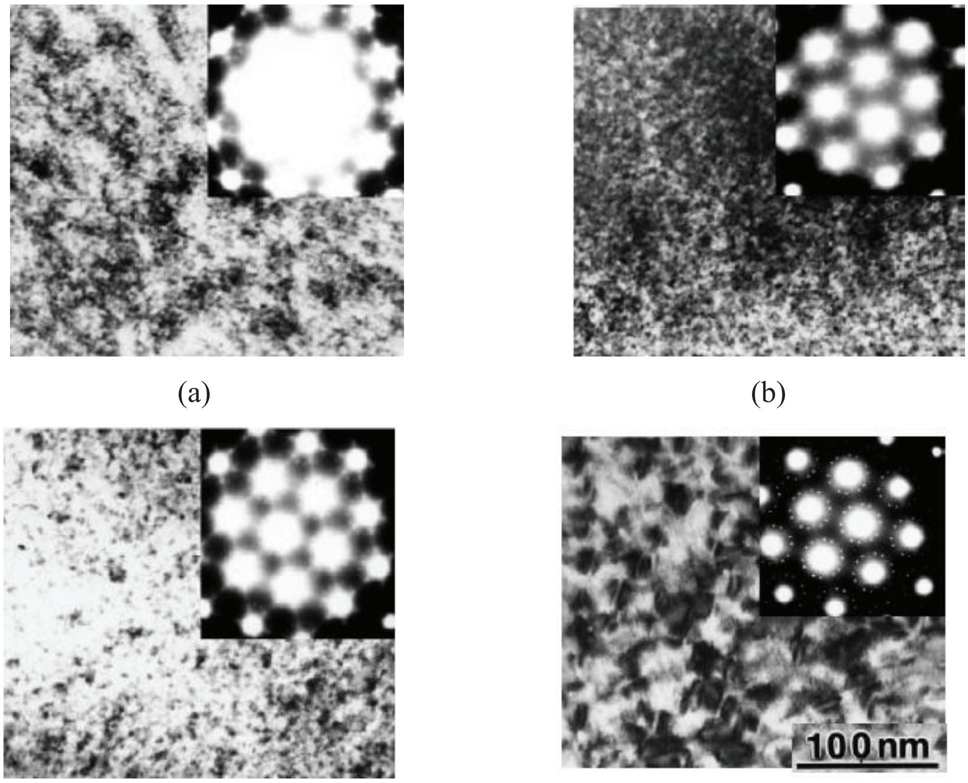

(a) (b)

(c) (d)

Figure 2.41 Electron microscope images of the 50.9 Ni at.% alloy at (a) 200 °C for 360 ks, (b) 200 °C for 7200 ks, (c) 300 °C for 1.2 ks (d) 300 °C for 1800 ks [103].

2.4. Stress-Assisted Aging of Ni-Ti Shape Memory Alloys

The distribution of precipitate variants is determined by the self-accommodation in such a way that minimizes the strain energy generated by the presence of precipitates. The number of possible variants is determined by symmetries of the parent and precipitated phases [104]. When a constraint is applied during aging the number of variants is smaller than the number determined by the symmetry relationship between the parent and precipitate phases because symmetry of the stress environment also acts as a parameter. Under the effect of constraint selective variant growth takes place [105,106]. In other words, the most important effect of the constraint is deterioration of the self-accommodative distribution of precipitate variants. However, the main criteria for variant selection is again the minimizing the total resultant strain energy of the system.

Actually, there are two types of constraints that can be applied during aging [107]. The first type is the strain constraint, in which, prior to aging, the boundaries of the strained specimen are immobilized. So, the aging takes place under constant volume and constant temperature condition. As a result of this, the aging is driven according to the minimization of Helmholtz Free Energy [108]. The second type of constraint, stress constraint, is achieved by application of a constant stress with mobile boundaries during aging so that aging takes place under constant pressure and constant temperature condition. Thus, the system is governed by the Gibbs Free Energy [108].

The strain related to presence of precipitates is actually created by the lattice mismatch between precipitates and parent phase. It is maximum along $<111>_{B2}$ for Ti_3Ni_4 precipitates with a value of -2.9% [106]. When stress is applied the strain contour changes direction and as a result of this variant selection due to minimization of energy takes place. The change in the direction of strain contour of a variant with application of stress can be understood from Figure 2.42, which shows the variation of strain energy contour as a function of angle, β, between the direction of the applied stress with z axis, $<111>_{B2}$. Here the dashed line, designated as 2, shows the strain created only by the precipitate. Lines 1 and 3 show the change due to applied tensile and compressive stresses, respectively. When the angle β is small compressive stress favors the growth of the variant and the situation is reverse for tensile stress.

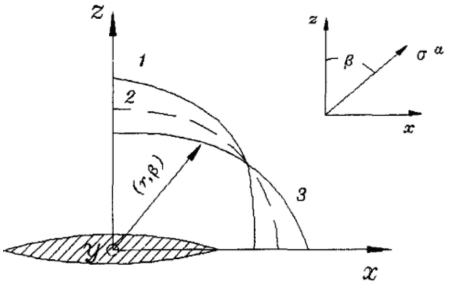

Figure 2.42 Schematic representation of strain energy around a Ti_3Ni_4 precipitate [109].

With growth of selected variants, the microstructures of an aged alloy is changed and as a result, it is even possible to observe precipitates with only one family of variants [110]. The drawings given below in Figure 2.43 represents the selective growth of two variants of which [111] axis are parallel to the $[111]_{B2}$ and $[11\bar{1}]_{B2}$ (a), under tensile (b), and compressive (c) stresses applied along x-axis which is parallel to the $[1\bar{1}0]_{B2}$. When a tensile stress is applied; the variant which is nearly perpendicular to the direction of applied stress grows preferentially, whereas under the application of compressive stress, the one which is nearly parallel to the applied stress direction is the selective one.

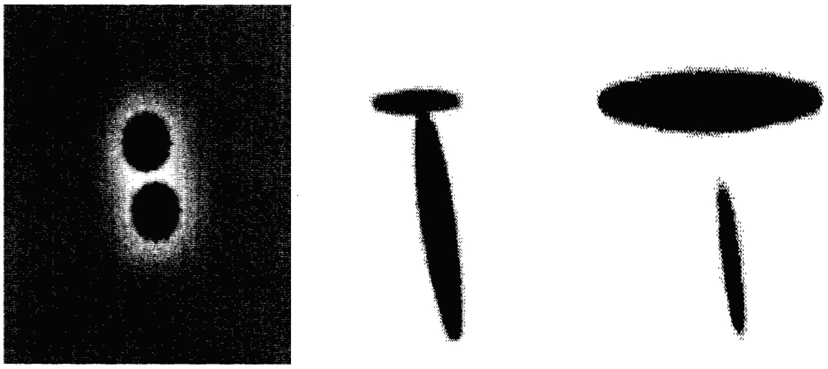

(a) (b) (c)

Figure 2.43 Representation of the growth of (a) two Ti_3Ni_4 particles with different variants (b) under tensile stress and (c) under compressive stress [108].

Stress and its magnitude affect the nucleation and growth processes. However, they influence the kinetics of nucleation and growth differently. Although, stress has a more pronounced effect on nucleation rate compared to the growth, stress level is not effective on nucleation of Ti_3Ni_4 precipitates. On the other hand, as stress level increases a small increase in growth rate is observed [94]. The increase in growth rate during stress assisted aging is ascribed to increase in diffusion rate due to the expansion of matrix under elastic strain [111]. Figure 2.44 summaries the effects of aging time and stress on final microstructure.

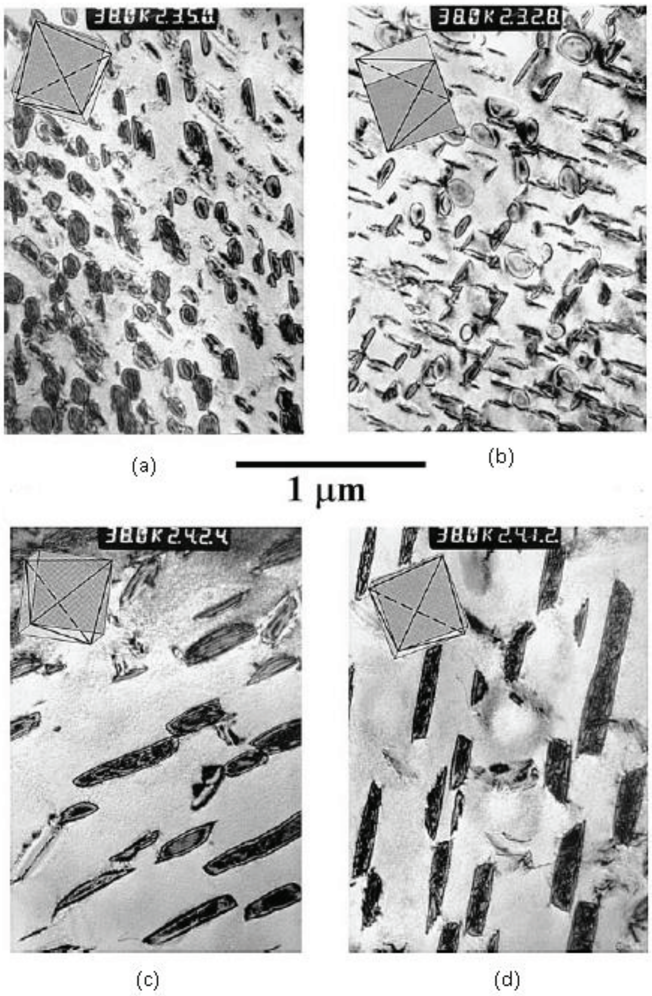

Figure 2.44 Microstructures of a 50.7 at. % Ni-Ti alloy which is aged at 500 °C (a) for an hour under 2 MPa of compressive stress (b) for an hour under 20 MPa of compressive stress (c) for 10 hours under 2 MPa (d) for 10 hours under 20 MPa [94].

By application of stress it is possible to obtain a homogeneous distribution of precipitates with respect to density and size of the throughout the microstructure. Under free aging conditions, the precipitates preferentially nucleate on grain boundaries due to decrease in surface energy. In addition, the stress induced by grain boundaries to the lattice near grain boundary regions aid precipitation. When stress is applied during aging, homogeneous distribution of precipitates is achieved because the applied stress overwhelms grain boundary stresses [94]. Figure 2.45 shows that the size and distribution of precipitates do not differ between grain boundary and grain interior.

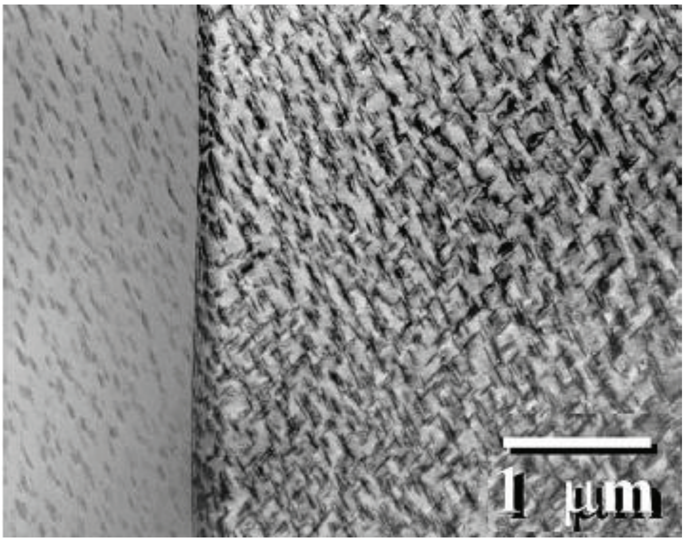

Figure 2.45 The distribution of Ti_3Ni_4 precipitates after aging at 500 °C for 1 hour under 20 MPa [94].

Also, the variants of precipitates differ according to their spatial location. The selection of different variants in different grains is related to different orientation of grains. On the other hand, the strain created by interaction of applied stress, grain boundary stress and presence of precipitate lead to different variant selection near grain boundaries and grains. In Figure 2.46, the volume fraction of different variants is given with respect to distance from grain boundary. The volume percentage of v1, v2, v3 and v4 belong to variants shown in figure 2.24.

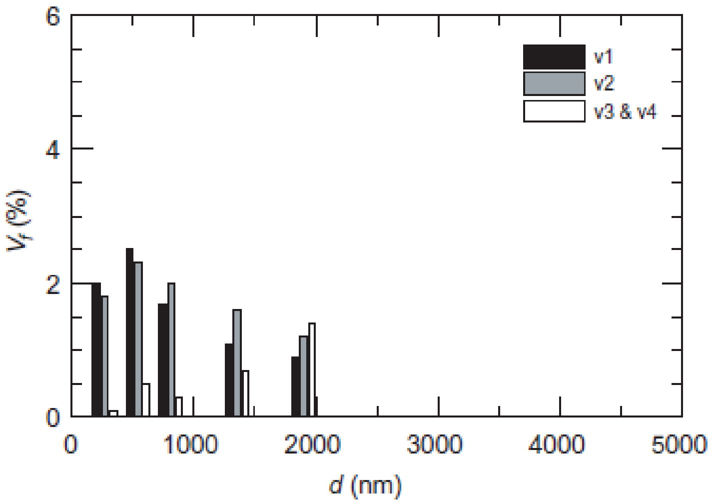

Figure 2.46 The change in volume percentage of precipitates formed during aging at 500 ^{o}C for 1 hour under 8 MPa with respect to distance from grain boundary [112].

The precipitates formed under stress are smaller than those formed in the absence of stress, because the applied stress brings competitive growth as an obstacle for the growth of precipitation. For the same aging time and temperature, stress free aging results in precipitates at grain boundaries which are in size comparable to precipitates formed during stress assisted aging in grain interiors [94].

The effect of aging on transformation temperature depends on stress due to changes in microstructure. The application of stress during aging results in increase in transformation temperatures. Up to very long aging times, the change in transformation temperature with stress level is not large. Also, the areas under the peaks of DSC charts are larger due to homogeneous microstructure [82]. DSC charts given below show the effect of stress, stress level and aging time on transformation behavior of 50.7 at.% Ni NiTi alloy which was solution treated at 900 ^{o}C for 15 minutes.

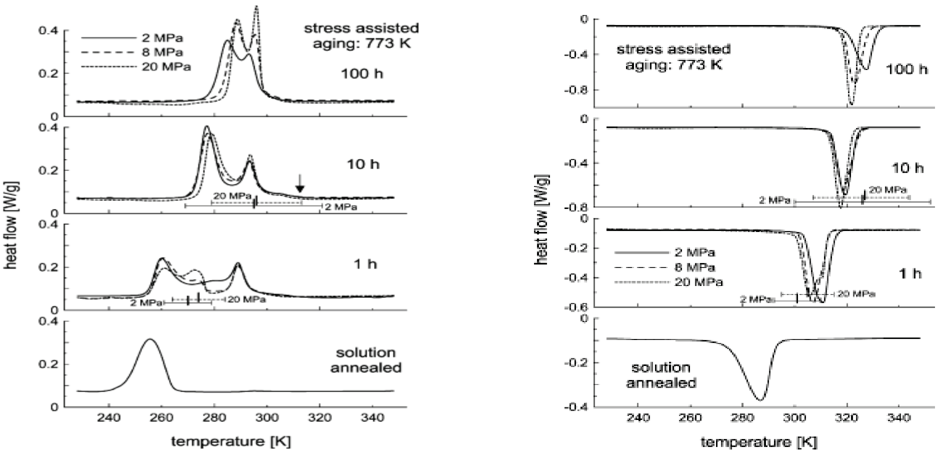

Figure 2.47 Effect of stress assisted aging on transformation behavior on cooling from B2 and heating from B19' [94].

When the aging time is short multiple-step transformation is observed. This is an indication of some sort of inhomogeneity. The dominated precipitate variants on grain boundary region and in grain interior change from the grain to grain. In addition, when the stress level is increased the area where the variants dominating on grain boundary region is higher [79]. According to Allafi et.al., the observation of multistep transformation is related to the number of variants of Ti_3Ni_4 precipitates present. The number of precipitate variant in grains is higher than that along grain boundaries or near-grain boundary regions. When all types of variants are present, the aid of precipitates to the martensite nucleation is larger, so in the grain interiors the formation of B19' from R-phase takes place at higher temperatures compared to the transformation along or near grain boundaries. Recalling Figure 2.47, the transformation sequence following to constrained aging at 500 ^{o}C for an hour is declared as the first transformation is $B2 \rightarrow R$ and the second and the third transformations are the transformation from R-phase to B19' inside of the grains and on and along the grain boundaries, respectively [94].

The reason for modifying microstructure and transformation behavior is improving functional properties such as superelasticity or shape memory behavior. Favier et.al.studied effect of aging conditions on superelastic behavior in Ni-rich NiTi alloys. In this study aging temperature was kept constant at 500^{o}C, and instead of applying constant stress, they studied constrained aging with constant strains of 2.5%, 5% and 7.5%, and aging times changing from 1 to 15 minutes. As a result of this study, they have revealed that recovered and unrecovered strain do not change with aging with these parameters [111]. Although, there is no discussion on that in the study, presence of unrecovered strains may be attributed to the local plastic deformation during aging under stress. Also, being more pronounced for constraint aging, critical stress for transformation decreases both upon loading and unloading subsequent to aging treatment. However, Favier et.al. reported that pseudoelastic hystresis does not change after neither stress free nor stress assisted aging.

Recalling equation 2.2, by use of the linearity constant obtained from the Clausius-Clapeyron Equation critical transformation stress at a given temperature can be calculated by using equation 2.9 given below.

$$\sigma_{A-M} = k(T - T_{A-M}) \text{ [111]} \qquad (2.9)$$

By use of this formula, Favier et.al. predicted the mechanism of critical stress increase subsequent to the stress-free and stress-assisted aging. According to them, the effective reason of the decrease in critical stress is the decrease in transformation temperature, and there is a perfect agreement between experimental and calculated data for stress assisted aging. On the other hand, experimental data deviates from the calculated one in stress free aging. For aging times less than 5 minutes, calculated data gives higher values compared to the experimental one, but as the aging time exceeds 5 minutes the situation is reversed. So, for aging times less than 5 minutes the formation of precipitates provides matrix softening, for longer times, formation of precipitates starts to provide matrix hardening. So, constrained aging inhibits or neutralizes the matrix hardening/softening mechanism, while after stress free aging matrix softening and hardening work in a competitive manner and the dominated one is determined by aging time and precipitation kinetics. The Figure 2.48 given below compares the experimental and calculated critical stresses subsequent to the two types of aging.

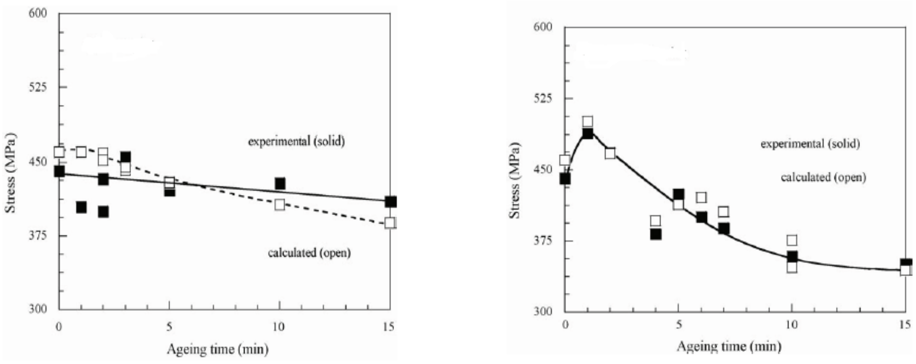

(a) (b)

Figure 2.48 Comparison of experimental and calculated critical stress as a function of aging time subsequent to (a) Free aging, (b) Constraint aging [111].

Table 2.2 given below summaries the differences between microstructures of a Ni-Ti alloy aged free and under stress.

Table 2.2 Comparison of Resultant Microstructures following to stress-free and stress-assisted and resultant transformation behavior.

	Stress Free Aging	**Stress Assisted Aging**
Precipitate Size [94]	Large	Small
Precipitate Size distribution [94]	Precipitate size increases with increasing distance from grain boundary	Homogeneous distribution
Precipitate Density distribution [94]	Fraction of precipitates are larger in regions near grain boundary	Homogeneous distribution
Transformation behavior [94,111]	On cooling: two step for short times & multistep for intermediate time	Multistep for short times at high stresses, two step for intermediate aging times
	On heating: two step	Single step
	Lower temperatures	Higher temperatures
Critical Stress [111]	Decreases with increasing aging time higher compared to stress assisted aging	Decreases with increasing aging time
Reason for critical stress change [111]	Matrix softening & change in transformation temperature	Change in transformation temperature

2.5. Hot-Rolling of Ni-Ti Shape Memory Alloys

NiTi-based shape memory alloys are subjected to various processing procedures. One of the most widely used procedures is hot-rolling. During hot-rolling not only shape change is maintained but also microstructure and in result transformation temperatures and mechanical properties are modified and optimized [113,114].

Hot rolling temperatures of NiTi alloys are determined by the requirement of good workability and inhibition of severe oxidation [115]. The general trend is working at temperatures higher than 600 ^{o}C and the mostly used temperatures are in the range of 800^{o}C-900^{o}C, where recrystallization and recovery takes place [116,117]. Due to high deformation rate (short times involved) and fast kinetics, recovery and recrystallization of the hot-rolled NiTi shape memory alloys are usually incomplete [117]. This was also confirmed by a TEM study of Gall et. al. [118].

Besides, generation of dislocations, hot working of NiTi based shape memory alloys results in texture formation [113,114,116-118]. The crystallography of texturing in hot-rolled NiTi alloys is observed to have spatial dependence which increases with increasing deformation. Texture along the rolling direction is dominated by <111> with an increasing <110> texture in the center of the bar as the percent deformation increases [118]. In most of the numerous studies on the subject the dominated texture parallel to the rolling direction was declared as <111> [114,116,117]. However, Robertson et. al stated that during production of endovascular stents the maximum texturing is along the <110> direction, whereas it is minimum along <111> and <100> in the rolling direction. Along the direction normal to the rolling one, texture maxima converts to <111> [113]. They have also stated that the texture in rolled plates are participated equally among three different crystallographic systems which are namely {111}<112>, {223}<110} and {122}<110>.

The hot-rolling performed at high temperatures causes dynamic recovery and recrystallization [114,116-118]. In addition, due to low driving force for precipitation at high temperatures the precipitate formation is reduced. Even, the dissolution of the existing precipitates is observed [114,116,118]. In other words, the microstructures of the hot-rolled NiTi alloys are reported as being in a near solutionized state with very low dislocation and nearly precipitate free. Furthermore, Gall et.al. stated that the percent deformation causes very slight changes in microstructure of the hot-rolled material and this slight change does not create any difference following the aging since the aging is much more dominant process for changing the microstructure and related transformation behavior and mechanical properties [118]. However, heat treatments which can create multistep transformation do not lead to this type of thermal behavior in hot-rolled NiTi alloys. According to Filip et.al, this is related to the presence of hot-rolling induced dislocations. They stated that the low defect density in the bulk makes precipitation take place dominantly at grain boundaries. In addition, due to dislocations the diffusion and in result precipitation kinetics are faster in hot-rolled Ni-rich alloys [119]. The dislocations in the bulk act as nucleation sites just like grain boundaries and as a result of this, the precipitate distribution is homogeneous. In their study, the hot-rolled specimens are firstly annealed at 900 ^{o}C, as a result of this there is no precipitation. However, if the temperature for recrystallization is coinciding with the regime of aging then different situations are possible. When the peak aging temperature of slightly Ni-rich NiTi is considered, precipitation is expected to take place before recrystallization and therefore, recrystallization is delayed [120].

The presence of defects, namely dislocations, does not only affect aging behavior, but also it changes transformation temperatures in such a way that with increasing percent deformation transformation temperatures decrease [116-118]. In addition, the decreasing rolling temperature creates the same effect [117]. This decrease in transformation temperature with increasing deformation is illustrated by Figure 2.49. The figure shows the decrease of the peak temperature of martensitic and reverse transformation with increasing hardness. As it is obvious, transformation temperatures are inversely proportional to the hardness and in result yield stress. The relationship can be expressed as [121]

$$M_s = T_o - K\Delta\sigma_y \tag{2.10}$$

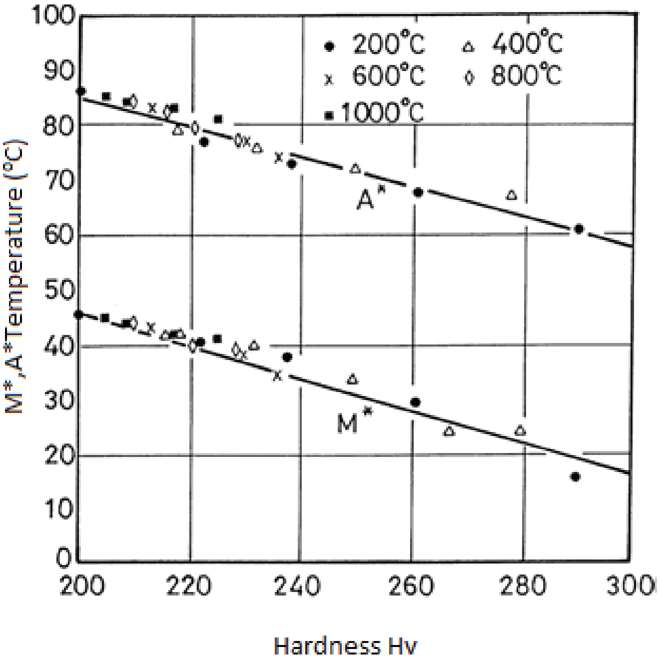

Figure 2.49 The peak temperatures of martensitic and reverse transformation [M* and A*,respectively) vs hardness (H_v) of the hot-rolled equiatomic NiTi alloy [117].

This decrease in transformation temperatures is related to the prevention of reorientation of martensite plates and in result hindering of martensitic transformations by dislocations [116]. Gall et.al. stated that the transformation temperature decrease associated with strain hardening is also observable after aging [118]. Even the hot-rolled bars with different percent deformation, have slightly different transformation temperatures after they are aged under exactly the same conditions. The difference is such that the one with higher percent deformation has lower transformation temperature [118]. However, if dislocation densities prior to aging are very different from each other, kinetics of aging will be highly influenced and as a result of this the difference between transformation temperatures will increase.

CHAPTER 3

EXPERIMENTAL PROCEDURE

3.1. As-received material

Ti - 50.7 at. % Ni alloys used in the present study were supplied by SAES Smart Materials. They were produced by vacuum induction melting and then hot-rolled at 900^{o}C to a diameter of 93 mm.

3.2. Experimental Method

In the scope of this study, the hot rolled Ni-rich specimens were aged both with and without application of stress. The stress levels and aging temperatures were determined considering the characteristics of the as-received material and outcome of the literature survey. Effect of applied heat treatment (aging with and without stress) on microstructure and thermally and mechanically induced transformation were examined.

3.2.1. Specimen Size and Shape

Specimen size and shape was determined according to the ASTM E209-00; Standard Practice for Compression Tests of Metallic Materials at Elevated Temperatures with Conventional or Rapid Heating Rates and Strain Rates [122] . Specimens were tetragonal prism shaped with a height of 8 mm and width of 4 mm. The specimens with given dimensions were extracted from the main piece by wire electrical discharge machining. The hot-rolling direction corresponds to the heigth, loading direction, of the specimens.

The surfaces of the specimens in contact with compression plates were grounded mechanically to provide parallelism, since lack of parallelism may result in wrong data and increased buckling effects.

3.2.2. Free Aging Experiments

The free aging (without stress) experiments were done at 400 ^{o}C for 1.5 hour in a Instron M3/SF-16 Split Tube Furnace. The deviation from the set temperature of the furnace at the test temperature was less than ± 2 ^{o}C after the stabilization of the specimen chamber due to the three zone design of it. The temperature control of the furnace is done by one K-type thermocouple which is mounted in the walls of the furnace. Figure 3.1 shows the furnace used with the specimen mounted in it.

Figure 3.1 Furnace used for free aging experiments with the specimen.

The procedure of the free aging experiments consisted of stabilizing the furnace at the heat treatment temperature, placing the specimen, waiting for five minutes for ensuring thermal homogeneity along the specimen, holding at the temperature for predetermined aging time and finally, water quenching. Prior to free aging, no solutionizing treatment was applied assuming that in hot rolled state, Ni-rich NiTi alloys were supersaturated solid solutions with negligible amount of precipitates [118]. In addition, the X-Ray Diffraction (XRD), Differential Scanning Calorimetry (DSC), Scanning Electron Microscopy (SEM) and Transmission Electron Microscopy (TEM) results also confirmed that there is no secondary phases in the microsructure of the as-received material.

The temperature and time for free aging is chosen as 400 ^{o}C and 1.5 hour, respectively. Since some dislocations and inhomogenities may be present in the hot-rolled structure, it is believed that aging times less than 90 minutes may lead to inhomogeneous material properties as a result of increased sensitivity to slight experimental variations. Aging temperature is limited to 400 ^{o}C for 90 minutes to prevent loss of coherency due to excess growth of the precipitates. [118,123]. The effect of aging time and temperature will be discussed further in the following.

3.2.3. Stress-Assisted Aging Experiments

Stress-assisted aging experiments were performed on 30 kN capacity Instron 3367 Creep Tester which is a screw driven universal tension-compression test machine- equipped with a three zone split furnace- as shown in Figure 3.2.

Figure 3.2 Instron 3367 Creep Tester with split furnace and chamber facilities.

For the stress-assisted aging experiments, subsequent to heating the furnace and stabilization of the temperature at 400 ^{o}C, which took around 5 minutes, specimen was inserted between the compression plates and load was applied at a rate of 0.1 mm/min. Figure 3.3 which shows the stress time diagrams for stress-assisted aging experiments indicates that there is no deviation from the predetermined stress level during aging. Once the predetermined stress was achieved, the specimen was held at 400 ^{o}C and under the test stress for 90 minutes and then immediately water quenched.

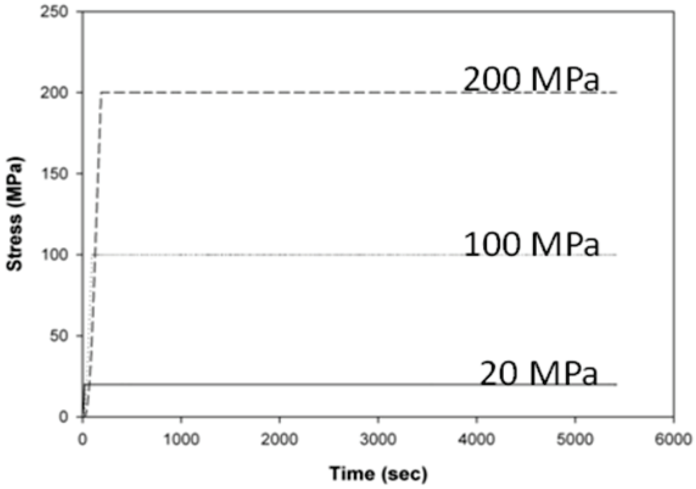

Figure 3.3 Stress and time diagram for stress-assisted aging experiments.

The stresses applied for stress assisted aging were 20, 100 and 200 MPa. The stress levels were determined such for comparison with literature, 20 MPa, and for observing the effect of higher stress levels, 100 and 200 MPa. Higher stress levels were decided based on the superelasticity and fracture tests on the specimens of as-received material so that no plastic deformation occurs during stress assisted aging.

3.3. Characterization Studies

In order to examine microstructure and relate this to final mechanical and thermal transformation behavior various characterization methods were used.

3.3.1. Microstructure

3.3.1.1. X-Ray Diffraction

For determining the phases present at room temperature, Rigaku D/Max 2200/PC model X-Ray Diffractometer with CuK$_\alpha$ radiation (λ=1.54178Å) at 40kV, 40 mA was used within a range of diffraction angles 2θ from 20^o to 90^o by continious scanning at a scan speed of 2 degree/min. As-received, free aged, stress-assisted specimens were examined by means of XRD. Ambient temperature during XRD studies was 22 ± 2 ^{o}C.

3.3.1.2. Metallographic Examination

The mounted specimens were mechanically ground and polished following to mounting. Grinding was done via SiC emery papers. As polishing material different size Al_2O_3 slurries, namely 5, 3, 1 and 0.3 µm were used. The etching was done with a solution of 10 ml HF + 5 ml HNO_3 + 85 ml for 5 minutes.

Microscopic visualization was performed by optical microscope and Jeol JSM 6400 SEM equipped with Noran System 6 (X-ray micro analyzer). In addition to this, transmission electron microscope studies were carried out to reveal precipitate morphology, size and distribution. TEM specimens were cut from the section perpendicular and parallel to the hot-rolling direction via a diamond coated copper disk 100 mm in diameter and 0.2 mm in thickness. The thickness of the specimens after sectioning was around 500 µm. The specimens were mechanically ground to 70 µm. Discs with a diameter of 3 mm were extracted from ground samples with a punch. The discs were electropolished to provide electron transparency. As electrolyte 5 vol% perchloric acid and 95% methanol solution was used. Electropolishing was performed at -20 ^{o}C, with 15 volt for 2.5 minutes via twin-jet. The TEM examinations were performed with Jeol JEM 2100 F using a double tilt holder.

3.3.2. Thermal Characterization

The specimens were cut using the aforementioned diamond coated copper disk 100 mm in diameter and 0.2 mm in thickness but at slower cutting speeds not to alter the phases present. To remove the damaged surface layer and ensure parallelism, the specimens were mechanically ground with fine emery papers.

A Perkin Elmer Diamond DSC was used for observing thermal transformation behavior. The tests were conducted under nitrogen atmosphere with heating and cooling rates of 10 ^{o}C/min. To study full transformation, the temperature range was chosen as -65 ^{o}C-+100 ^{o}C and five cycles were done in this temperature range to observe the effect of thermal cycling. Transformation temperatures and enthalpy of transformation were determined on the second cycle to get rid of one time effect according to the procedure described in the ASTM F2004-05 Standard Test Method for Transformation Temperature of Nickel-Titanium Alloys by Thermal Analysis [124].

3.3.3. Mechanical Characterization

Mechanical tests consisting of uniaxial compression, which was applied only to the as-received specimen at ambient temperature with a loading rate of 0.1 mm/ min, and the superelasticity tests were performed using the Creep Tester mentioned previously.
The specimens used for mechanical testing were with dimensions 8x4x4 mm. As in the stress-assisted aging the surface of the specimens in contact with compression plates were mechanically ground to prevent any deviation from parallelism between surfaces of the specimen.

3.3.3.1. Pseudoelasticity Tests

Samples were subjected to superelasticity tests under uniaxial compression at different temperatures, namely, room temperature, which is below the A_f, and 20 ^{o}C above room temperature, 40 ^{o}C above room temperature and 60 ^{o}C above room temperature, which are above the A_f. Superelasticity tests were conducted at strain levels in the range of 0 to 4% since the hot-rolled specimens can recover strains up to 3.5 % at maximum under compression [123]. For temperatures other than room temperature chamber of the creep tester is used. The deviation from the set temperatures was around ±2 ^{o}C after stabilization of the chamber temperature. Strain measurements during superelasticity tests were done with an extensometer with gauge length of 25 mm and operation temperature range of -100 ^{o}C - +200 ^{o}C.

3.3.3.2. Microhardness Tests

Since the hardness of the specimen can be related to the size and distribution of precipitates, Vickers microhardness tests were performed by Schimadzu Microhardness equipment. In addition, a mechanical data for comparison of the superelastic characteristics was obtained. All of the specimens were heated to 80^{o}C and held there for 10 minutes in order to relieve the stress induced by mechanical grinding and polishing, and then air cooled. During testing a Vickers 136^{o} face angle diamond indenter is used by loading 980.7 mN in 20 seconds. Each sample was indented for 5 times and the average values were used for illustrating the effect of stress level applied during aging on hardness of the specimen.

CHAPTER 4

RESULTS AND DISCUSSION

4.1. Microstructural Characterization

4.1.1. As-received Material

Ti - 50.7 at. % Ni alloys used in the present study were supplied by SAES Smart Materials. They were produced by vacuum induction melting and then hot-rolled at 900^{o}C to a diameter of 93 mm.

As can be seen in Figure 4.1 (a), some of the grains of the as received alloy were aligned in the hot rolling direction. Hot rolling texture present is expected to be strong along <111> direction and moderate along <101> direction as it is common in hot-rolled Ni-rich Ni-Ti alloys [114,117,118]. Figure 4.1 (b) and (c) show that the substructure of the grains is composed of austenite and martensite lamellas. Martensite is believed to be stress induced during mechanical grinding and polishing stages of metallographic specimen preparation. The selected area $[\bar{1}11]$ zone diffraction pattern, Figure 4.2, shows that the material has only the austenite phase of NiTi alloys with B2 crystal structure.

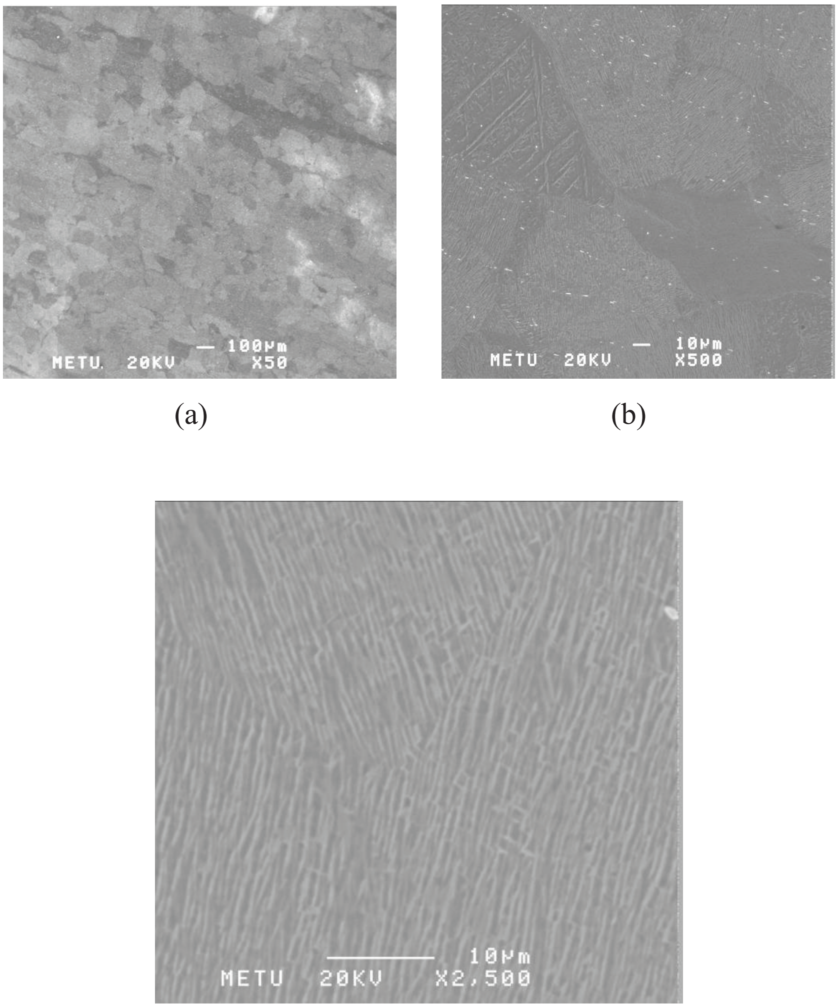

(a)

(b)

(c)

Figure 4.1 The microstructure of as-received material, a) The grain structure b) austenite and martensite phases c) martensite substructures.

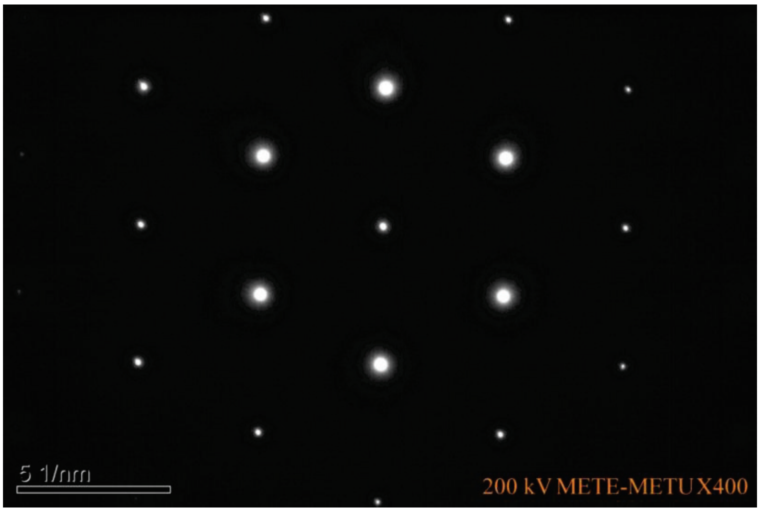

Figure 4.2 The selected area diffraction pattern of as hot-rolled 50.7 at.% Ni-Ti alloy perpendicular to the rolling direction showing the $[\bar{1}11]$ zone.

4.1.2. Aged Specimens

The aging time and temperature, 90 minutes and 400 ^{o}C, respectively, are constant for all aging experiments. The microstructural examinations were done along the direction perpendicular to the rolling and loading directions during aging. In all of the specimens both martensite and austenite phases are observed together. In optical micrographs, there are a number of grains with higher contrast compared to the others. The higher contrast of these grains stems from preferential etching due to their orientations.

From Figure 4.3 to 4.7, the microstructures of the aged specimens are shown. There is no difference between specimens with respect to grain size. On the other hand, the martensite amounts are different due to different transformation temperatures.

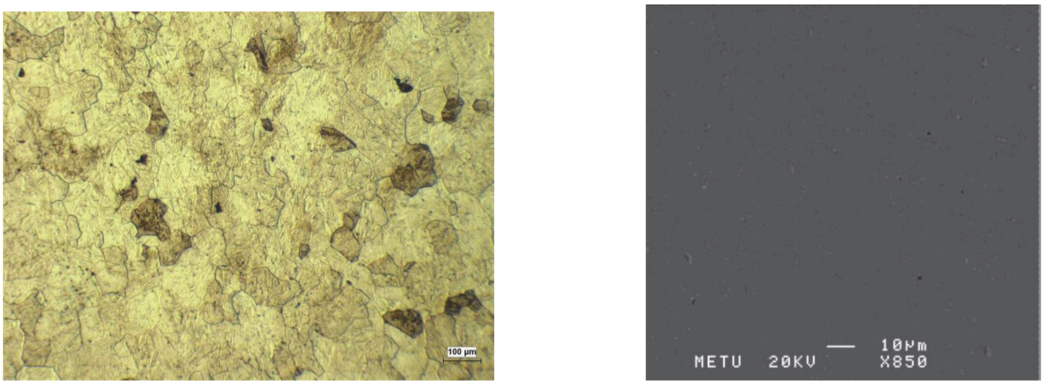

(a) (b)

Figure 4.3 (a) Optical microscopy image (b) Scanning electron microscopy image of the free aged specimen.

Figure 4.4 (a) shows the bright field TEM image of the free aged sample perpendicular to the rolling direction. The precipitates that appear darker probably due to absorption contrast have a size around 10 nm. In addition, Figure 4.4 (b) shows the $[111]_{B2}$ zone diffraction pattern of the same specimen. The bright dots are due to the austenite phase whereas the satellite spots around the matrix spots are due to the R-phase. The precipitates are coherent and very small.

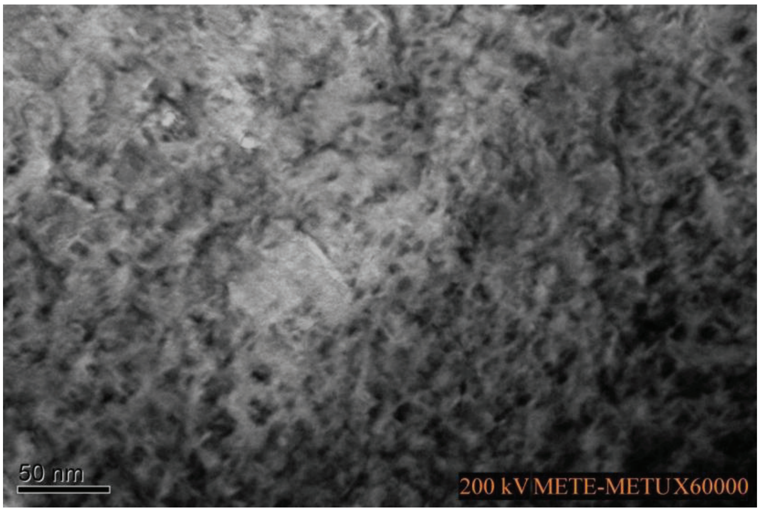

(a)

Figure 4.4 Electron microscopy images of the free aged specimen. (a) distribution of Ti_3Ni_4 precipitates (b) Selected area $(111)_{B2}$ zone diffraction pattern showing the presence of austenite and R-phase.

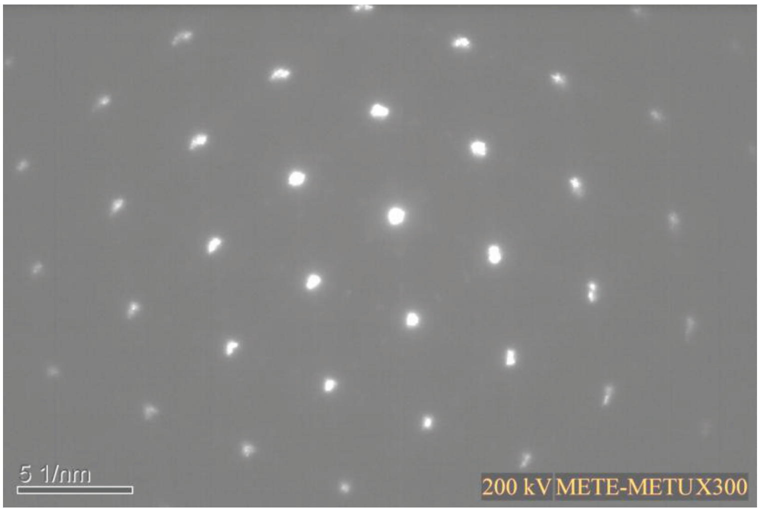

(b)

Figure 4.4 (continued)

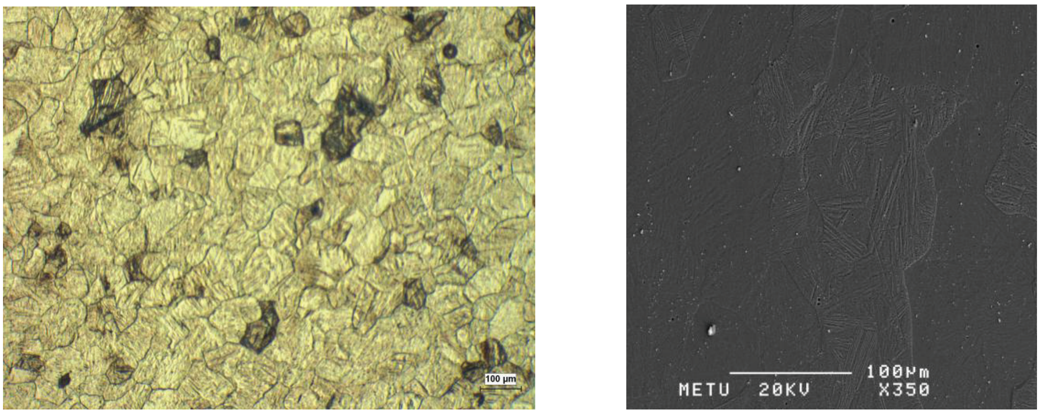

(a) (b)

Figure 4.5 (a) Optical microscopy image (b) Scanning electron microscopy image of the specimen aged under 20 MPa specimen.

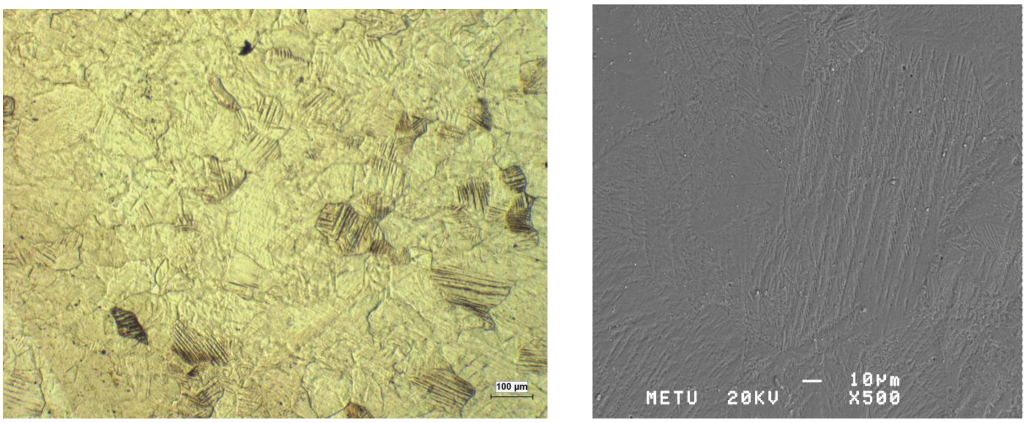

(a) (b)

Figure 4.6 (a) Optical microscopy image (b) Scanning electron microscopy image of the specimen aged under 100 MPa.

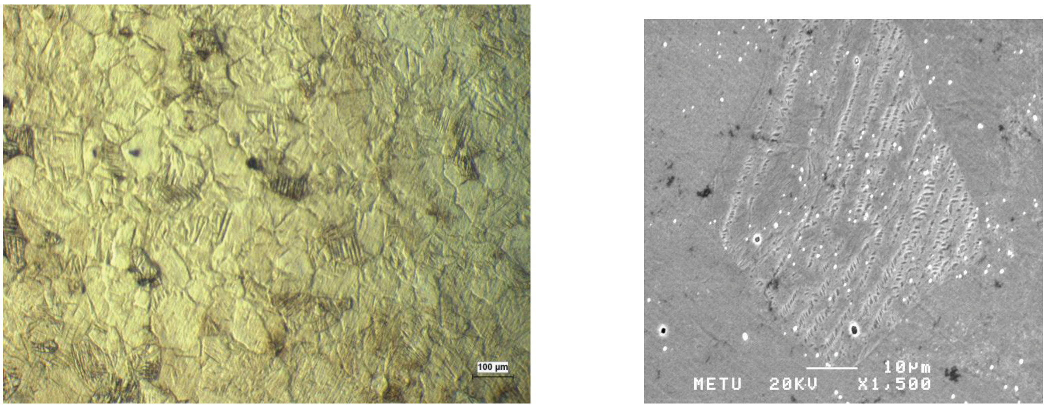

(a) (b)

Figure 4.7 (a) Optical microscopy image (b) Scanning electron microscopy image of the specimen aged under 200 MPa.

4.2. Phase Analysis

4.2.1. As-Received Material

Figure 4.8 shows the X-Ray diffraction pattern of the as-hot-rolled specimen before and after metallographic specimen preparation. The peaks of the sample subjected to metallographic specimen preparation are increased by 5000 cps in intensity and shifted 25°

right during graphical demonstration for the sake of clarity. The analyses are made from the surface parallel to the rolling direction. The dominant peak with much higher intensity with respect to the other ones belongs to $[110]_{B2}$ before metallographic specimen preparation, whereas the intensity of the $[1\bar{1}1]_{B19'}$ peak increases at the expense of the mentioned $[110]_{B2}$ peak after metallographic specimen preparation. The results indicate formation of martensite lamella with $[110]_{B2}//[1\bar{1}1]_{B19'}$ orientation, which are also observed in SEM micrograph, due to metallographic specimen preparation. In addition, there are no observable secondary phases such as Ti_4Ni_2O, $TiNi_3$, $TiNi_2$ or Ti_3Ni_4.

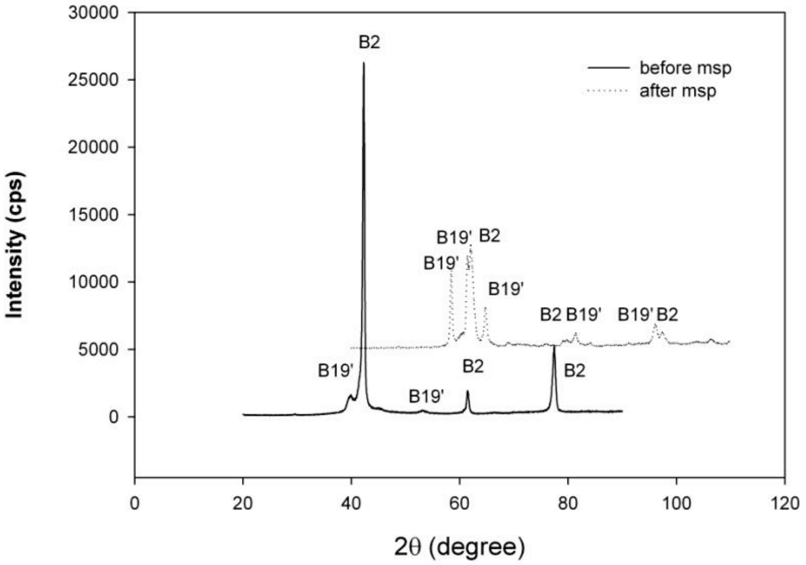

Figure 4.8 XRD patterns of the as-received Ni-rich specimen before and after metallographic specimen preparation (msp).

4.2.2. Aged Specimens

Figure 4.9 shows the XRD chart of the free aged specimen. The intensity of B2 austenite phase decreases at the expense of an increase in the intensity of martensite phase with B19' crystal structure and additionally, Ti_3Ni_4 peaks appear. The increase in the amount of B19' phase in aged alloys is a result of increase in transformation temperatures due to nickel depletion of the matrix upon precipitation of Ti_3Ni_4. XRD results also show that during aging process, no secondary phases other than Ti_3Ni_4, namely Ti_4Ni_2O, $TiNi_3$, or $TiNi_2$

have formed. The XRD pattern of the specimen aged under 20 MPa, given in Figure 4.10, is not very different from that of the free aged one.

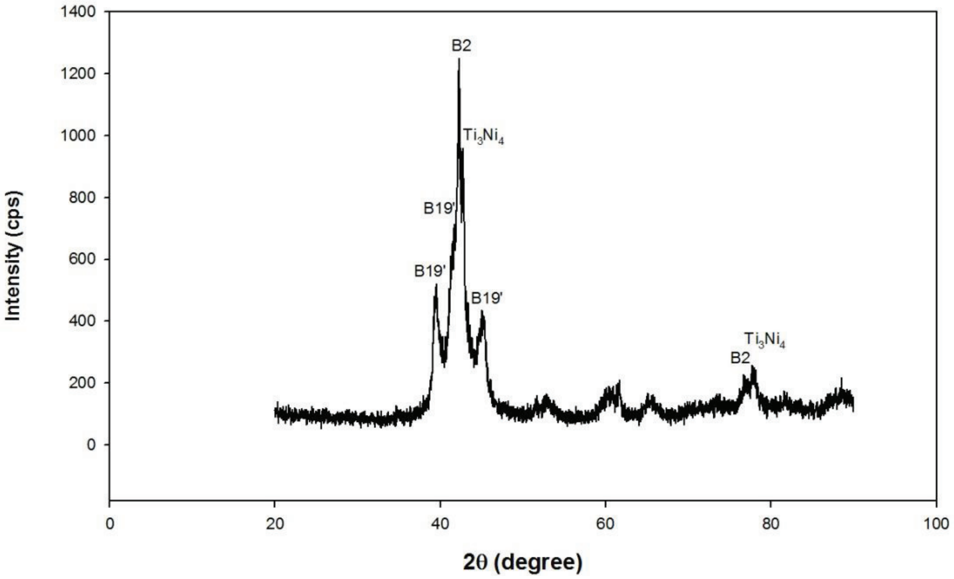

Figure 4.9 XRD patten of free aged specimen.

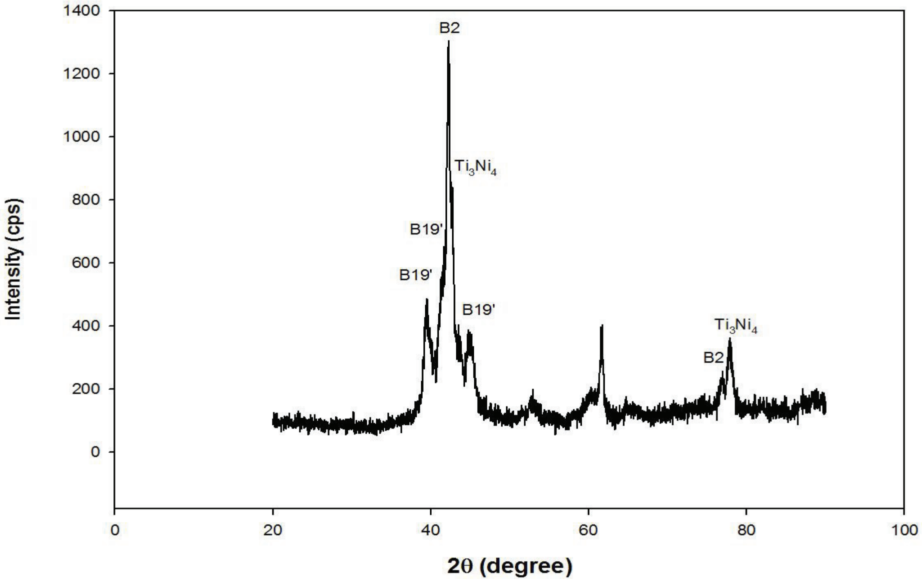

Figure 4.10 XRD pattern of specimen aged under 20 MPa.

Figure 4.11 shows the XRD chart of the aged specimen under 100 MPa of stress where the intensity of Ti_3Ni_4 peak is increased in a considerable manner.

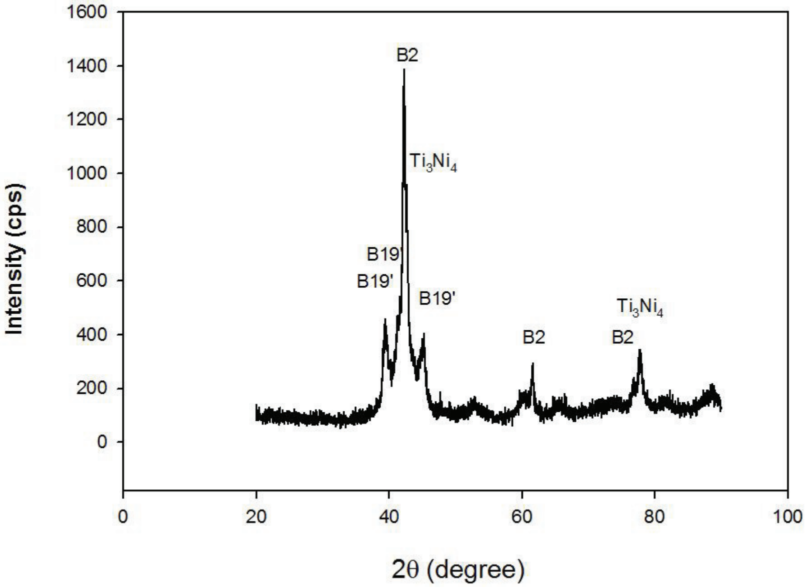

Figure 4.11 XRD pattern of the specimen aged under 100 MPa.

Figure 4.12 shows the XRD pattern of the specimen aged under 200 MPa. The same trend with the other aged samples is also observable in this specimen. The intensity of peaks due to B2 phase (austenite) decreases while the intensity of martensite phase increases and Ti_3Ni_4 emerges in comparison with the as-hot-rolled specimen. Nevertheless, the intensities of B2 phase and Ti_3Ni_4 are higher than that of observed in free aged and aged under 20 MPa sample but not different from that of the specimen aged under 100 MPa.

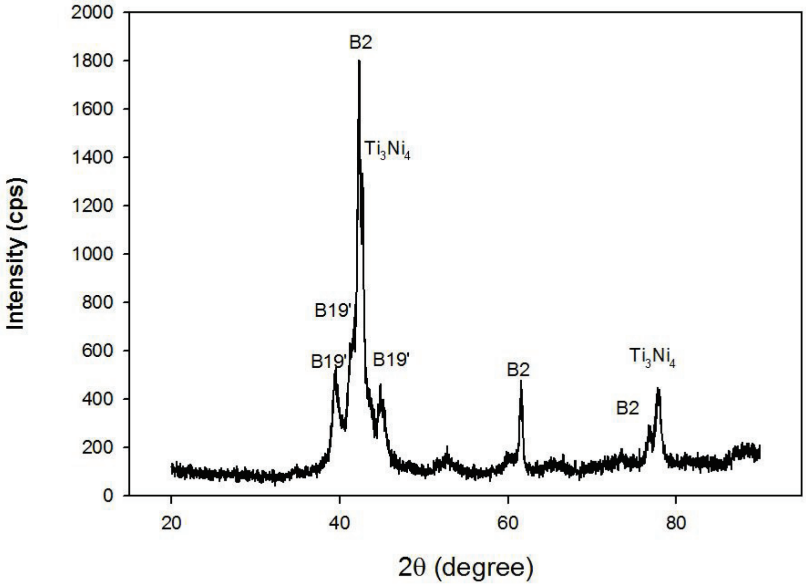

Figure 4.12 XRD pattern of the specimen aged under 200 MPa.

4.3. Thermal Analysis

4.3.1. As-received Material

DSC curves given in Figure 4.13 show the temperature induced phase transformations observed in as hot-rolled 50.7 at. % Ni-Ti alloy. The transformations are completed in one step both upon heating and cooling. These are $B2 \rightarrow B19'$ and $B19' \rightarrow B2$ transformations upon cooling and heating, respectively. The transformation temperatures are given in Table 4.1. However, M_f temperature could not be determined due to instability of DSC instrument at very low temperatures. The transformation peaks are very broad probably because transformation takes place at the adjacent regions at slightly different temperatures due to presence of nonuniformly distributed dislocations resulting from the incomplete dynamical recovery and recrystallization during hot rolling [117,118].

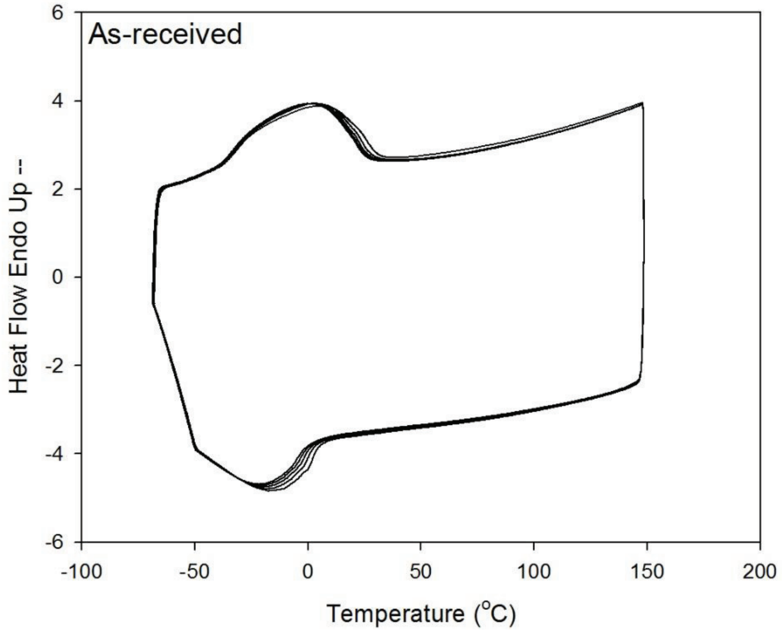

Figure 4.13 DSC curves of as hot-rolled NiTi alloy.

Table 4.1 Phase transformation temperatures as hot-rolled NiTi.

A_s	A_p	A_f	M_s	M_p	M_f
-38 °C	2 °C	29°C	4°C	-18°C	-

4.3.2. Aged Specimens

Figure 4.14 shows the DSC curves of thermally induced transformations observed in free aged specimen in the temperature range of -70 °C and +150 °C. In this temperature range, the specimen is heated and cooled for five cycles and cycling is observed not to affect the transformation behavior. In table 4.2, transformation temperatures and associated latent heat of the free aged sample are given.

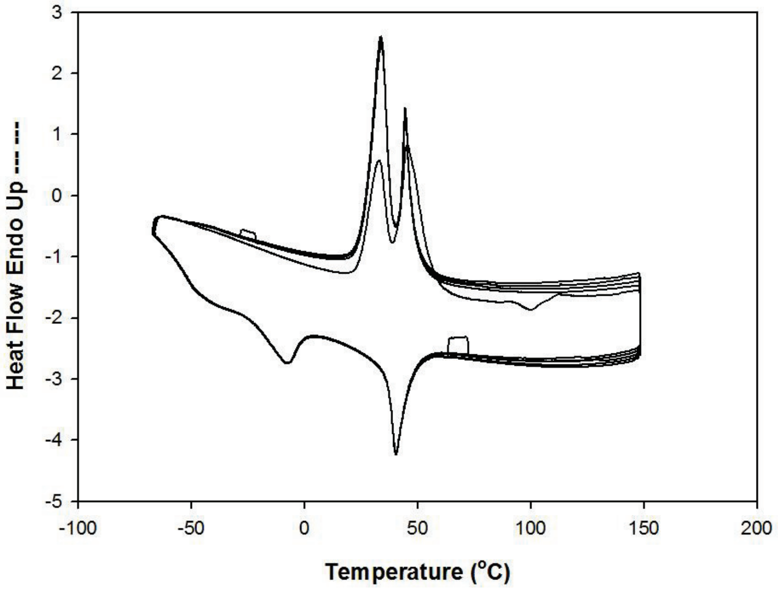

Figure 4.14 DSC curves of free aged sample.

Table 4.2 Phase transformation temperatures and associated latent heat of the free aged sample.

	HEATING		COOLING		
	$B19' \rightarrow R$	$R \rightarrow B2$	$B2 \rightarrow R$	$B2 \rightarrow B19'$	$R \rightarrow B19'$
Start (°C)	22	43	50	0	-
Finish (°C)	41	53	35	-27	-
ΔH (J/g)	11.23	5,97	-4.6	-3.14	-

Two transformations are observed during heating. In the literature, latent heats of $B19' \rightarrow R$ and $R \rightarrow B2$ transformations were reported to be 9.3 J/g and 6.5 J/g, respectively [92,125]. The latent heat of transformations upon heating of the free aged specimen being in good agreement with the values given above indicate that first $B19' \rightarrow R$ and then $R \rightarrow B2$ occur sequentially.

Upon cooling, the $B2 \rightarrow R$ transformation is observed with a peak at approximately 40 ^oC, where the transformation is expected for a Ti - 50.0 at. % Ni alloy [103,126] indicating that the metastable chemical equilibrium between precipitate and the matrix is maintained and the matrix composition is reduced to 50 at% Ni during aging [38].

On the other hand, $R \rightarrow B19'$ is not observed through the temperature range due to suppression effect of precipitates and associated strain field. However, the differences between complete latent heats of cooling and heating suggest that the transformation has probably occurred but cannot not be detected due to low temperature instability of DSC instrument. The second transformation upon heating and the first transformation upon cooling corresponds each other with transformation hysteresis of 6 ^oC. This low transformation hysteresis is also a sign of $B2 \leftrightarrow R$ transformation [92].

Figure 4.15 shows the thermal transformation behavior of the alloy aged under 20 MPa of stress during five cycles. Upon heating three transformations, first two of which overlapp, are observed. The small thermal hysteresis of the last transformation upon heating, (6^oC), shows that this is R to B2 transformation [92]. The first two transformations upon heating can be interpreted as $B19' \rightarrow R$ phase transformation splitting into two. However, the total latent heat of these transformations is higher than a complete $B19' \rightarrow R$ transformation indicating that the first two peaks upon heating cannot be associated with these transformations. Another possibility is that the first two transformations are associated with $B19' \rightarrow R \rightarrow B2$ transformation. However, it is known that transformation between R-phase and B2 is the least affected transformation from strain induced by precipitates. In addition to this, the peak of transformation from B2 to R-phase upon cooling shows that the metastable chemical equilibrium is achieved, the completion of $B19' \rightarrow B2$ transformation in two steps is not likely to occur. So, after application of 20 MPa of stress during aging, an inhomogeneous microstructure is formed with respect to precipitate distribution and in result there are stressed and unstressed regions. In the regions, where precipitates present and create strain field triggering R-phase transformation and the

$B19' \rightarrow R$ transformation takes place in these regions whereas the precipitate free regions go through $B19' \rightarrow B2$ transformation. At higher temperatures, the regions with precipitates go through $R \rightarrow B2$ transformation.

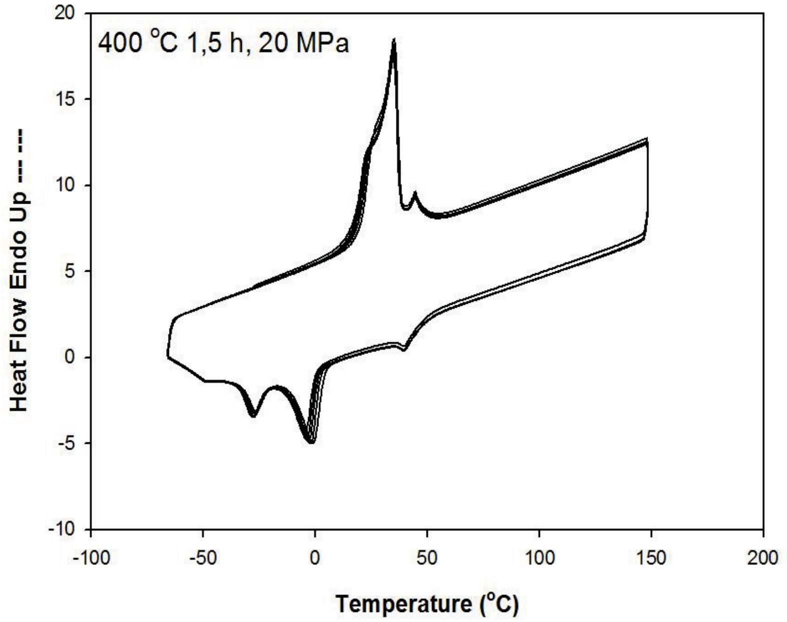

Figure 4.15 DSC curves of the sample aged under 20 MPa.

Table 4.4 Phase transformation temperatures and associated latent heat of the sample stress-assisted aged under 20 MPa.

	HEATING			COOLING		
	$B19' \rightarrow R$	$B19' \rightarrow B2$	$R \rightarrow B2$	$B2 \rightarrow R$	$B2 \rightarrow B19'$	$R \rightarrow B19'$
Start (°C)	19	-	40	52	3	-22
Finish (°C)	-	39	51	34	-13	-33
ΔH (J/g)	16.54		1.73	-0.84	-5.10	-1.62

Upon cooling three transformations are observed which are $B2 \rightarrow R$, $B2 \rightarrow B19'$ and $R \rightarrow B19'$. Due to inhomogeneous distribution of precipitates, strained regions go through $B2 \rightarrow R$ transformation at high temperatures. Subsequent to these, unstrained matrix goes through $B2 \rightarrow B19'$ transformations. The regions where precipitates are present transformed from R-phase to B19' finally due to suppressing effect of precipitates on this transformation.

The forward and reverse transformations are corresponding to each other. However, the difference between latent heat of transformations upon heating and cooling shows that the transformations upon cooling are incomplete. The two step behavior of forward and reverse martensitic transformations and low transformation enthalpies are believed to be related to the heterogeneous nucleation of precipitates on dislocations.

The thermally induced transformation behavior of the alloy aged under 100 MPa is shown in Figure 4.16. The transformation of the specimen is single step both upon cooling and heating. The R-phase transformation which was observed in other aged specimens around 40 ^{o}C did not take place during thermal cycling. The thermal hysteresis of the forward transformation (A_f-M_s) is 26 ^{o}C, whereas for reverse transformation (A_s-M_f) it is 24 ^{o}C. For single phase NiTi single crystals, these values are equal to each other. With increasing size and volume fractions of precipitates the ratio of thermal hysteresis of reverse transformation to that of forward transformation increases [78]. The small value of this ratio of this alloy and single step transformation shows that the precipitates lose the coherency inducing strain field and affecting transformation behavior. The decrease in thermal hysteresis with respect to as-received material is believed to be related to decrease in Ni content of the matrix and annihilation of some the dislocation and in result formation of a more homogeneous microstructure.

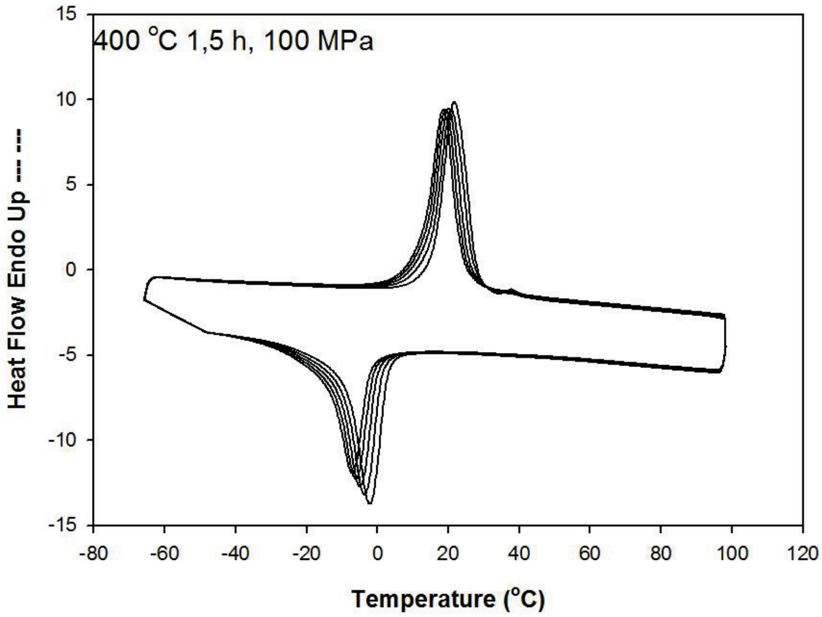

Figure 4.16 DSC curves of the sample aged under 100 MPa.

Table 4.4 Phase transformation temperatures and associated latent heat of the sample stress-assisted aged under 100 MPa.

	HEATING	COOLING
	$B19' \rightarrow B2$	$B2 \rightarrow B19'$
Start (°C)	13	2
Finish (°C)	28	-11
ΔH (J/g)	19.07	-13.20

On the other hand, when thermal transformation behavior of the alloy aged under 200 MPa of stress, which is given in Figure 4.17, is examined, again multistep transformation is observed. There are two transformations upon heating and one definite peak up on cooling, the transformation temperatures of which are given in Table 4.5. Upon heating, the transformations are characterized as $B19' \rightarrow B2$ and $R \rightarrow B2$, respectively. The latent heat of transformations indicate that both are incomplete.

Upon cooling the peak of $B2 \rightarrow R$ transformation is observed approximately at 40 °C just like in other specimens which go through R-phase transformation indicating that the matrix is in chemical equilibrium with Ti_3Ni_4 precipitates and has approximately 50 at. % Ni. Although the peaks are not definite, there seems to be a second transformation which is believed to be $R \rightarrow B19'$. The latent of the transformation indicates that transformation is not completed. The difference between complete latent heat of cooling and heating also suggests that the second transformation has occurred but could not be detected due to low temperature instability of the DSC instrument.

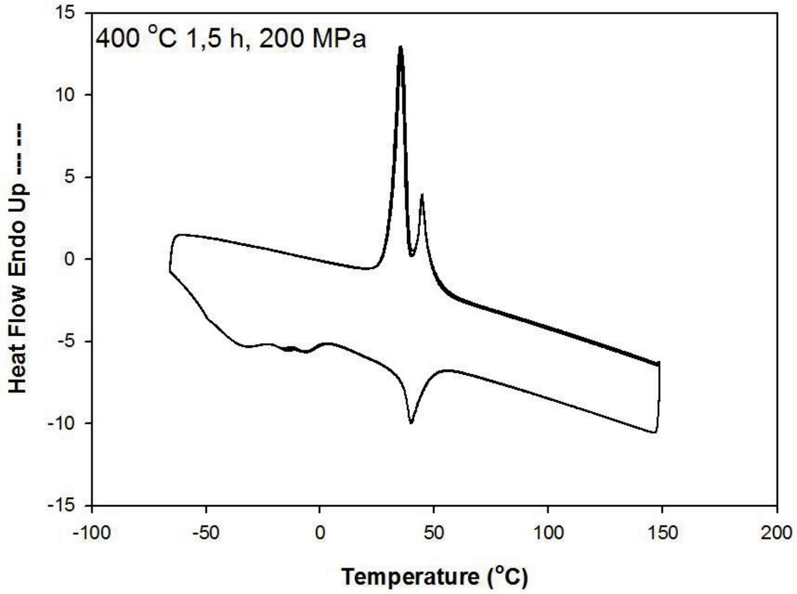

Figure 4.17 DSC curves of the sample aged under 200 MPa.

Table 4.5 Phase transformation temperatures and associated latent heat of the sample stress-assisted aged under 200 MPa.

	HEATING		COOLING	
	$B19' \rightarrow B2$	$R \rightarrow B2$	$B2 \rightarrow R$	$R \rightarrow B19'$
Start (°C)	28	41	51	-
Finish (°C)	39	51	35	-
ΔH (J/g)	9.720	3.750	-3.53	-

4.4. Mechanical and Superelastic Characterization

4.4.1. As-received Material

The compressive stress strain diagram of the as-received material loaded parallel to the rolling direction at room temperature is given in Figure 4.18 (a). The diagram consists of four regions. The first one is the elastic deformation of austenite phase, which continues up to a stress of 375 MPa and 1% strain. The stress induced transformation that follows lasts up to 475 MPa and 3% strain. The third region is the elastic and plastic deformation of the stress induced martensites. The deformations continue until 1000 MPa and 6% strain. Subsequent to these, plastic deformation of martensite takes place. The test was not ended up by fracture due to the buckling of the specimen. Figure 4.18 (b) shows the compressive response of the as-received specimen deformed only up to 5% strain to examine the transformation region in detail and also to observe unloading response before the yield of the martensite. The results show that the transformation plateau upon loading is nearly linear and slightly sloping up. The unloading curve on the other hand can be said to exhibit nearly linear elasticity for a great portion which can be interpreted as an indication that the stress induced martensites cannot transforms back to austenite due to dislocation slip that has taken place simultaneously with the transformation [127,128]. Also, the low value of the recovered strain, 27% of the total strain applied, verifies this interpretation. This limited recovery is expected because martensite formation under stress along the [111] direction is not much favored, whereas dislocation motion is favored [130]. In addition, effect of the test temperature should be mentioned. To observe complete pseudoelasticity, the test temperature should be above the A_f temperature so that the martensitic transformation is only due to the applied stress and when stress is removed austenite, which is the stable phase, forms again. However, the room temperature at which the tests are conducted is below the aforementioned temperature for Ti- 50.7at. % Ni alloy in hot-rolled condition rather than above that. So, as it is proved by SEM, DSC and XRD as well, the preexisting martensites do not wholly transforms back to austenite upon unloading and as a result the unrecovered strain level is quite high. However, high unrecovered strain level can be explained by the untransformed martensites and deformation induced by martensite formation. Another reason for high unrecovered strain is the dislocation slip which starts right after transformation at 3.5% strain and continues until end of loading.

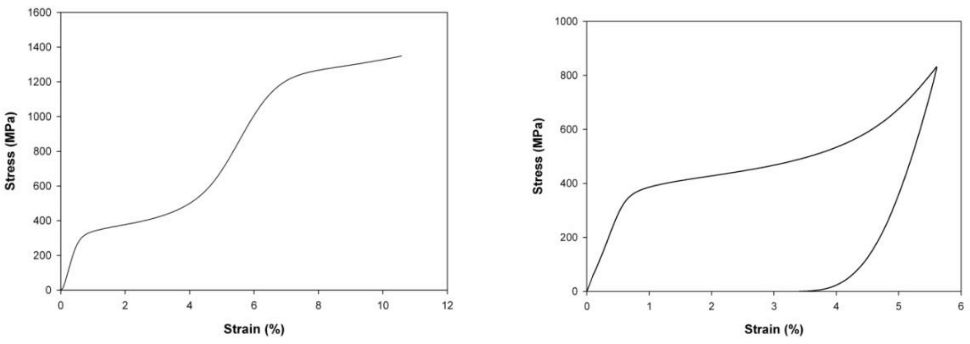

(a) (b)

Figure 4.18 Room temperature compressive stress-strain behavior of the as-hot-rolled material up to (a)11% (b) 5% total strain.

Effect of temperature on superelasticity characteristics of the as received alloy is shown in Figure 4.19 and Figure 4.20. In order to avoid plastic deformation, all specimens are loaded to around 600 MPa during all tests except the one at room temperature. The samples are recovered to a considerable extent but inconsistently because of different total strains at different temperatures under the same load. At 80^{o}C which is quite above A_f, elastic recovery dominates over the pseudoelastic one.

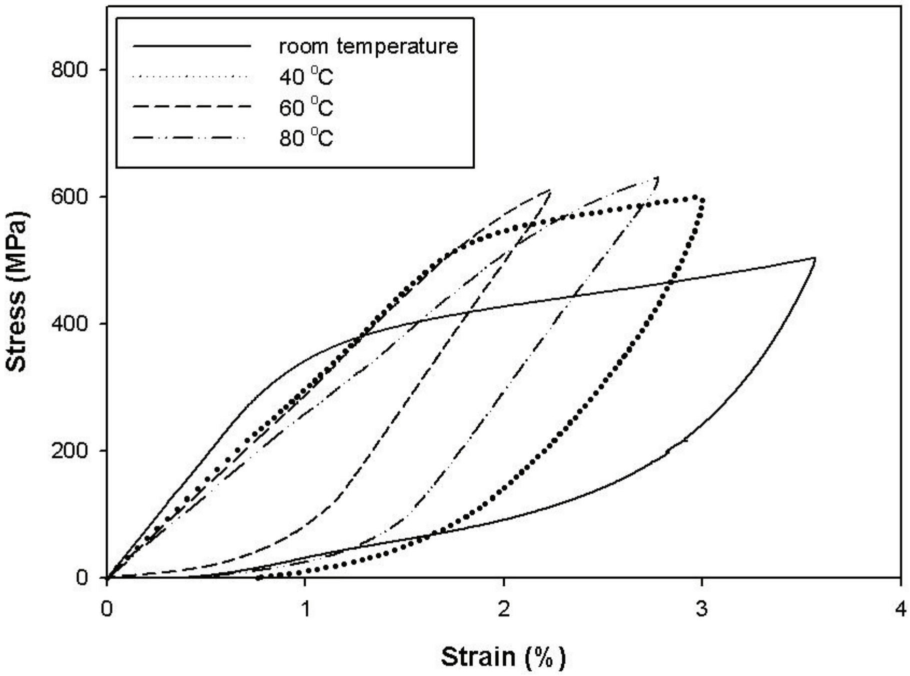

Figure 4.19 Stress-strain behavior of as hot-rolled 50.7at.% Ni- Ti alloys at different temperatures when a virgin specimen is used for each test.

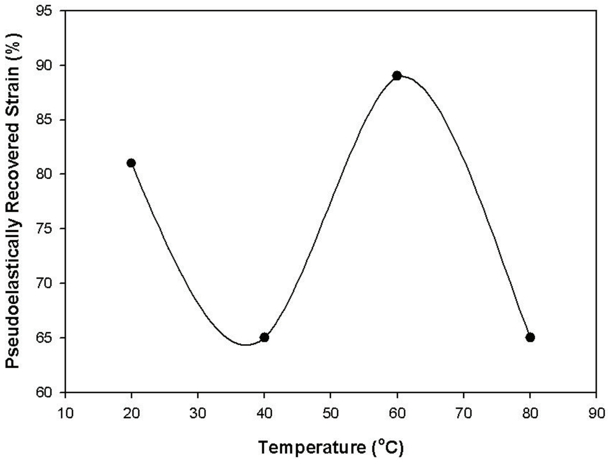

Figure 4.20 Dependence of pseudoelastically recovered strain on test temperature of as received samples.

Figure 4.21 shows the temperature dependence of the critical stress for forward transformation. The Clasisus-Clapeyron constant, found as 3.5 MPa/°C from the slope of

Figure 4.21, for single crystals under compression was reported to be between 4-8 MPa/ ^{o}C according to crystal orientation [130]. The above given calculated value is lower than the reported ones. The reason is that at 60^{o}C and 80 ^{o}C, since the temperatures are quite over A_f, the response to the applied stress involves mechanisms other than transformation induced deformation. When only 20^{o}C and 40 ^{o}C tests are considered the values raises to the 4.3 MPa/^{o}K and this is expected for a polycrystalline NiTi alloy [56,131-133] within limits of experimental error.

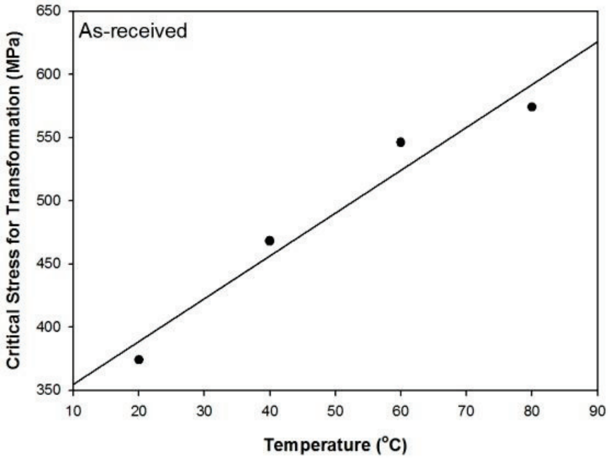

Figure 4.21 Dependence of the critical stress for forward transformation on temperature.

The loading and unloading moduli of the as-received material are given in Figure 4.22. The loading modulus decreases when the temperature is increased to 40 ^{o}C and then remains nearly the same. It is known that elastic constant of austenite decreases sharply as the temperature gets close to any of the martensitic transformation $(B2 \rightarrow B19^{'}, B2 \rightarrow B19, B2 \rightarrow R)$ temperature. However, the increase is slight for $B2 \rightarrow B19$ and $B2 \rightarrow R$ transformations [81]. So, decrease in elastic modulus of austenite at 40 ^{o}C is probably related to the formation of R-phase from B2. The formation of R-phase is related to the inherent dislocations from the hot-rolling. Since the increase in elastic modulus with increasing temperature is slight following to this transformation the elastic modulus is remained unchanged in the test temperature ranged in the study.

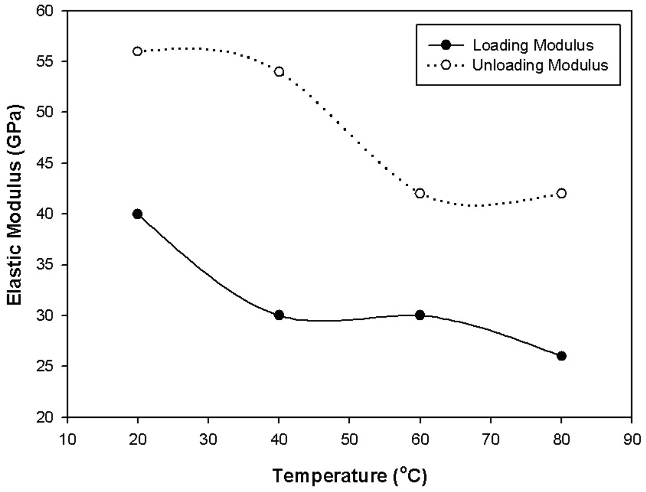

Figure 4.22 Dependence of the loading and unloading modulus on temperature.

The unloading modulus of the compression stress-strain diagram is an indication of stress-induced martensite amount if loading is limited to the transformation plateau [130,134]. So, the unloading modulus actually refers to the elastic modulus of martensite. The unloading modulus, i.e., amount of stress induced martensite is same for room temperature and 40 ^{o}C. However, the pseudoelastically recovered strain decreases when the temperature increased to 40 ^{o}C. The reason is that the deformation with stress induced martensitic transformation causes the stabilization of martensite and stabilization becomes more and more dominant as the deformation amount increases [135]. Since at 40 ^{o}C, the martensitic transformation taking place is $B2 \rightarrow R \rightarrow B19'$ and the strain associated with this transformation is higher than the one taking place at room temperature, $B2 \rightarrow B19'$, the stress induced martensite amount is lower at this temperature.

The unloading slope decreases above 40 ^{o}C and remains same indicating that the amount of martensite by application of stress is constant above that temperature. However, the recovered strains and shape of the stress-strain curves indicate that the deformation mechanism as a response to the applied stress changes with increasing temperature. At 60 ^{o}C, the most of the martensite formed transforms back and as a result of this, the recovered strain amount is higher than that at higher temperature. At 80 ^{o}C, the pseudoelastically recovered strain decreases abruptly, showing that at that temperature formation of stress induced martensite and dislocation slip takes place together, and dislocations prevent reverse transformation upon unloading. Also, the recovered strain at 60 ^{o}C is higher than that at room temperature and 40 ^{o}C. Since the room temperature is below A_f temperature, the amount of martensite to be recovered is lower. In comparison to 40 ^{o}C, the stabilization effect is lower at 60 ^{o}C.

The same superelasticity tests at different temperatures are also applied to a single specimen with intermediate anneals at 90 ^{o}C between each loading. The results of the superelasticity tests are given in Figure 4.23. Critical stress for transformation is observed to increase with increasing temperature due to the increased stability of austenite phase inherited from the previous loading step. The reason is that as dislocation slip takes place concurrently with the stress-induced transformation and annealing at 90 ^{o}C cannot eliminate the dislocations, the unrecovered strain increases at each step at higher temperature as can be seen in Figure 4.24. During loading at all temperatures, both mechanisms, namely dislocation slip and stress induced transformation, take place simultaneously because the testing temperatures are in partial pseudoelastic region. At room temperature, martensitic transformation is comparatively dominant mechanism with respect to dislocation slip, whereas with increasing temperature, slip starts to be more and more active. Also, the texture in specimen and large grain size (100-300μm) favor slip instead of stress-induced transformation [127]. In addition to this, it has been shown that the stress-induced transformation under compressive loading is not completed along the plateau. Maximum recovered strain values are achieved after an upward slope observed on the stress-strain diagram following the plateau. Along this part of the curve, stress induced martensitic transformation, elastic deformation of the martensites formed and probably some dislocation slip take place simultaneously [136].

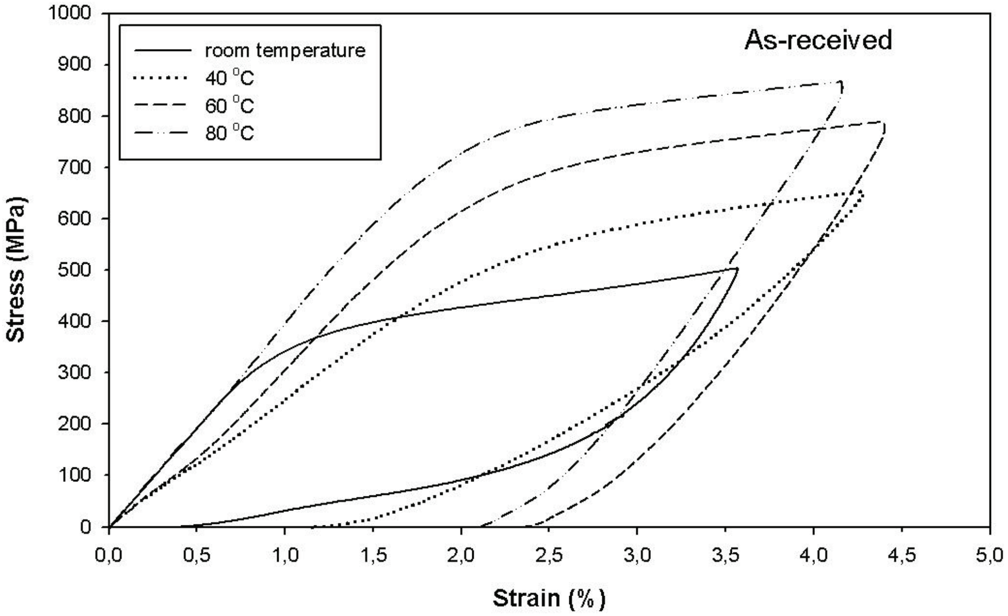

Figure 4.23 Stress-strain behaviour of as hot-rolled 50.7 at. % Ni- Ti alloy at different temperatures starting with room temperature but using a single specimen with intermediate anneals.

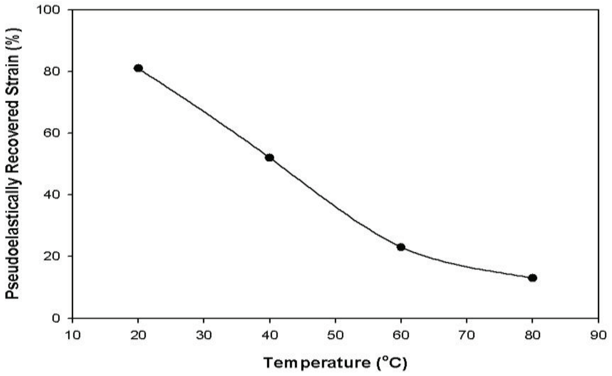

Figure 4.24 Dependence of pseudoleastically recovered strain on temperature.

Figure 4.25 shows the dependence of critical stress on temperature when a single specimen with intermediate anneals have been used. The slope of the critical stress versus temperature curve, which gives the Clausius- Clapeyron constant for forward transformation, is calculated as 6,4 MPa/^{o}K. In the literature, for Ni-rich NiTi alloys, it has been reported to be between 5-8 MPa/°K [56,131-133]. When the Clausius-Clapeyron constants of the two aforementioned cases, namely tests with single specimen subjected to intermediate anneals and tests with virgin samples at each temperature, are compared, it can be said that transformation strains of the virgin samples are larger as a result of this the constant gets smaller. Since some of the austenitic regions to be transformed are locked by dislocations created during former loading.

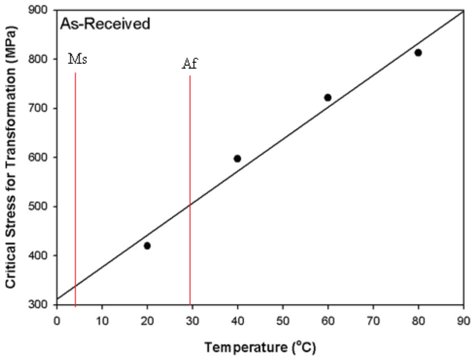

Figure 4.25 Dependence of critical stress for forward transformation on temperature.

The loading and unloading moduli of the as-received material are given in Figure 4.26. When the loading moduli of annealed and virgin samples are compared, it is seen that the annealed samples show less stiff behavior at 40°C upon loading. The reason may be the transformation of some amount of preexisting martensites to austenite during annealing and then transformation to R-phase at 40 °C. When the temperature is increased to 60 °C, loading modulus stays nearly constant as it is expected. At 80 °C, the loading modulus increases with respect to 60 °C. This can be interpreted as that the dislocation formed during previous three loading locked the martensites and as a result of this during annealing they cannot revert back. Actually, this is an expected result because even the deformation during transformation of stress induced martensite results in an increase reverse transformation temperature [135]. When this effect is combined with the dislocation slip created by applied stress martensite stabilization becomes unavoidable.

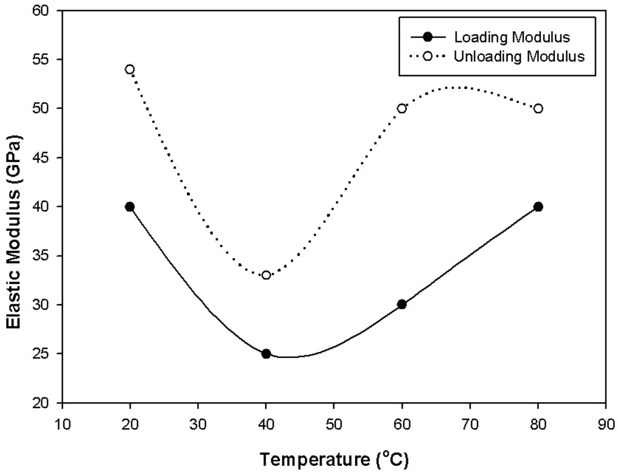

Figure 4.26 Loading and unloading moduli of the as-received material.

The unloading modulus at 40 °C is very low indicating that the amount of martensite formed by aid of stress is low compared to that of virgin sample and that at room temperature. The reason is that the dislocations created during the loading at room temperature remains in the sample. Furthermore, the pseudoelastically recovered strain decreases rapidly when the temperature is increased from 20 °C to 40 °C. This is again related to the stabilization of martensite following to $B2 \rightarrow R \rightarrow B19'$ and also dislocation slip. Since, at the initial state the amount of martensite is lower than the virgin specimen; dislocation slip takes place simultaneously with the stress induced transformation because of the fact that austenite yield point is much lower than that of martensite. As a result of this, the amount of stress induced martensite is lower and so is the unloading modulus. Further increase in temperature causes increase in unloading modulus. However, the recovered strain amount continues to decrease. So, although with increase in temperature the amount of martensite during loading is increased and stays same in the temperature range of 60 °C- 80 °C, the recovered amount decreases. This verifies that the dislocation slip and stress induced martensite formation takes place concurrently for annealed specimens.

4.4.2. Aged Specimens

Figure 4.27 shows the results of the superelasticity tests on free aged samples at four different temperatures with intermediate anneals. All of the specimens except 20 °C recovered significantly. The dependence of pseudoelastically recovered strain on testing temperature is given in Figure 4.28. Since, the room temperature is below the $A_{f,}$ stress induced martensites do not revert back completely upon unloading. The superelasticity behavior observed at 40 °C is superior such that the strain is almost fully recovered by reverse transformation. Also, at that temperature, reorientation of R-phase is observed during loading. The small plateau region on loading part of the stress-strain diagram can be seen in Figure 4.29. At 60 °C, a better recovery than 40 °C is expected, since this temperature is even higher. However, the increase in unrecovered strain indicates that at that temperature dislocation slip starts to take place in addition to stress induced transformation. There is no clear plateau on stress-strain diagram at 80 °C, indicating that upon loading elastic deformation of austenite is the main response mechanism to the stress and in result pseudoelastically recovered strain is slightly less than that of 60 °C test. Actually, it is expected because after observation of slip at 60 °C, a lower total strain is applied to the material at this temperature.

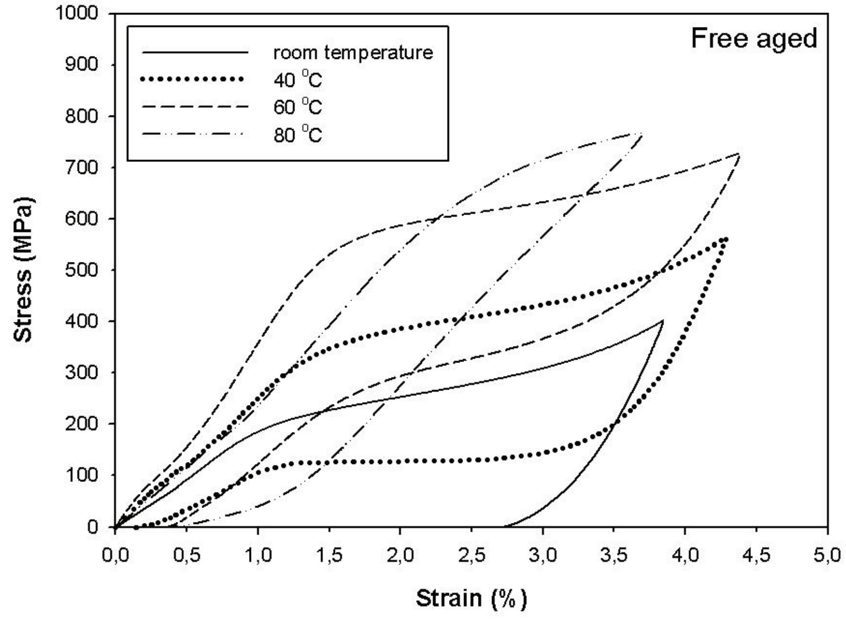

Figure 4.27 Stress-strain diagrams of free aged 50.7 at. % Ni- Ti alloys at different temperatures.

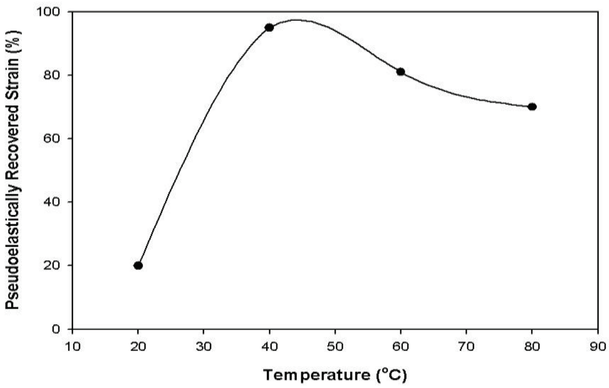

Figure 4.28 Dependence of pseudoelastically recovered strain on temperature of the free aged specimen.

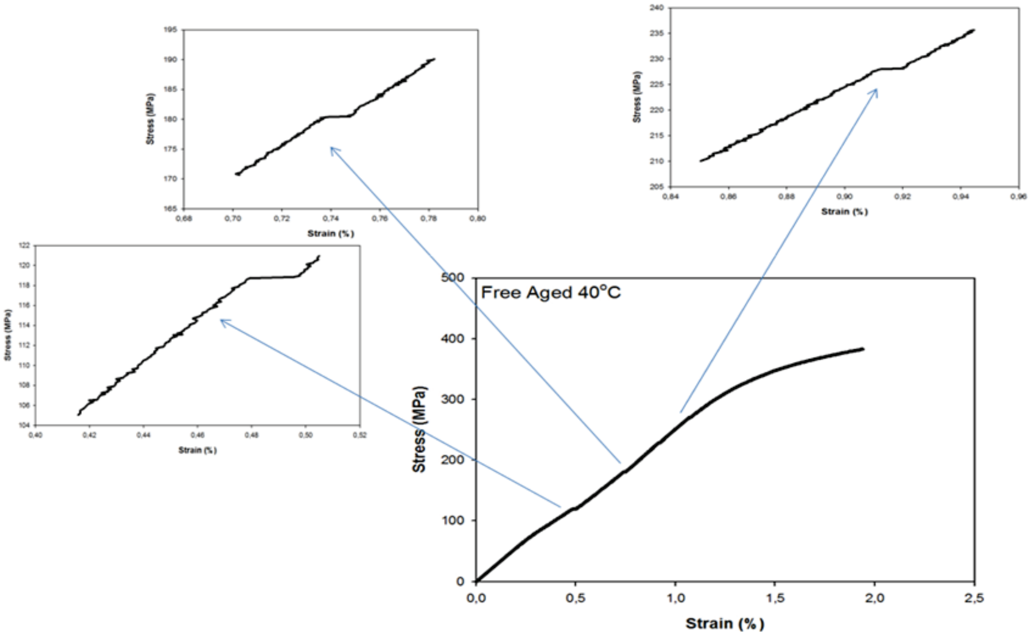

Figure 4.29 Successive reorientation of R-phase variants.

The dependence of superelastic behavior on temperature of the specimen aged under 20 MPa is given in Figure 4.30. At all test temperatures, the specimen showed a clear plateau for forward transformation. The recovery is not consummating at room temperature and 80 ^{o}C, as it can be seen in Figure 4.31. The unrecovered strain at room temperature is related to the thermal stability of martensite phase at this temperature since it is below A_f. On the other hand, the stress induced martensites are stabilized due to the deformation during transformation at 80 °C. Actually, the stabilization of stress induced martensites starts at 60 °C. Although, this temperature is higher than A_f, the pseudoelastically recovered strain, is lower compared to that at 40 °C due to the stabilization effect. At 40 °C, reorientation of R-phase is observed upon loading. Figure 4.32 shows the small reorientation plateaus which are nearly at the same strain levels with that of free aged specimen.

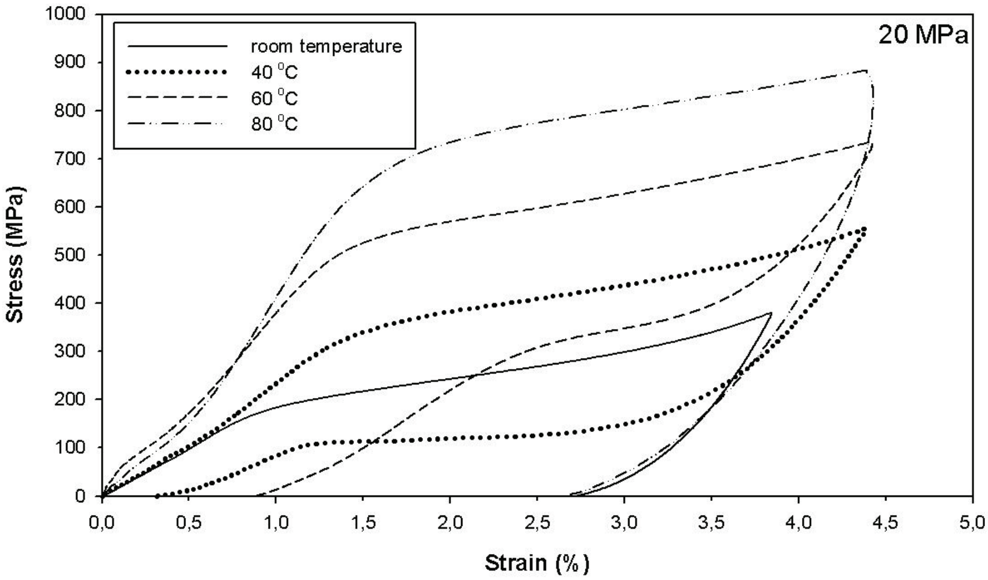

Figure 4.30 Stress strain diagrams of the specimen aged under 20 MPa at different temperatures.

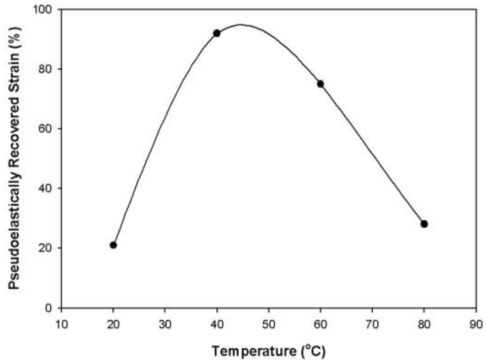

Figure 4.31 Dependence of pseudoelastic recovery on temperature of the alloy aged under 20 MPa.

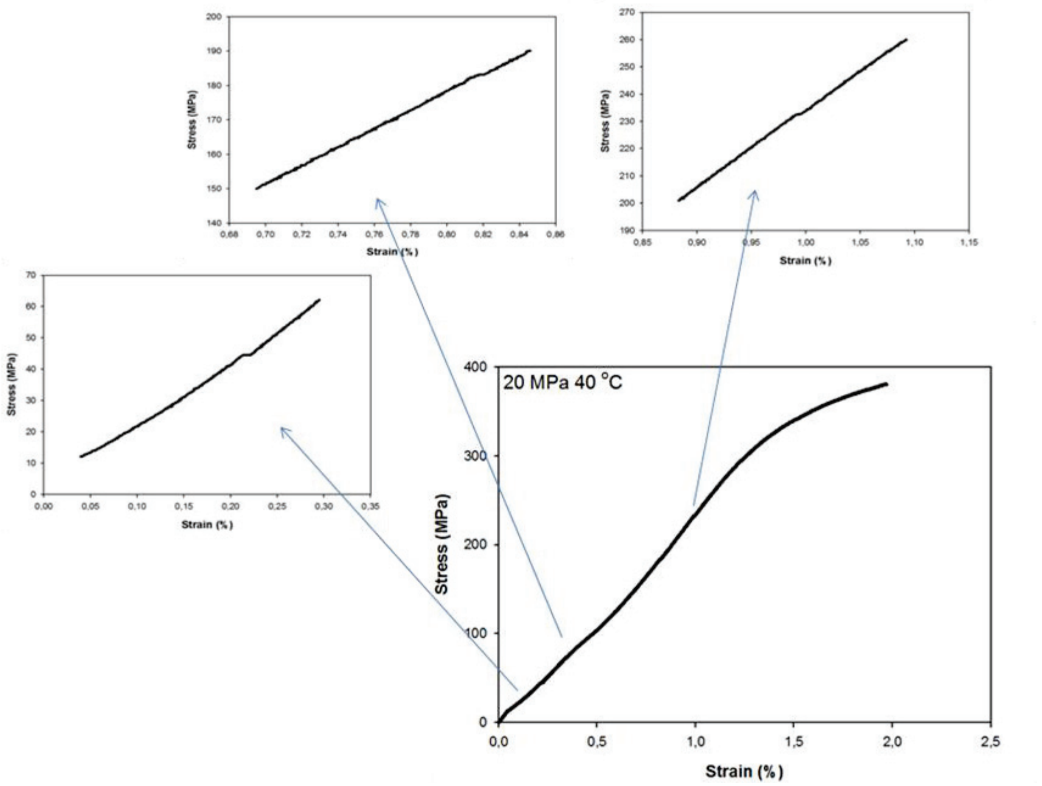

Figure 4.32 Successive reorientation of R-phase variants observed in a specimen aged under 20 MPa.

The stress-strain diagram of the specimens aged under 100 MPa, which are mechanically tested at different temperatures with intermediate anneals at 90 ^{o}C are given in Figure 4.33. At all test temperatures except room temperature, an explicit transformation plateau is observable. In addition, all curves except the one corresponding to 80 ^{o}C, shows the region with an upward slope following to transformation plateau where stress induced transformation, deformation of austenite and reorientation of martensites take place together. The shape of the stress-strain diagram at room temperature indicates the start of stress induced transformation immediately upon loading. However, the pseudoelastically recovered strain, which is given in Figure 4.34, shows that most of the martensites formed during loading did not revert back during unloading due to the fact that the A_f temperature is above the test temperature. On the other hand, the recovery improves when the temperature is raised to 40 ^{o}C and clear plateaus upon loading and unloading are observed. The pseudoelastically recovered strain increases even more when the testing temperature is

60 °C due to increased stability of the austenite phase. In addition to this, the elastic recovery of the austenite phase upon unloading also increases and mechanical hysteresis of transformation decreases. The pseudoelastic recovery diminishes with further increase in temperature due to the deformation which avoids the reverse martensitic transformation upon unloading.

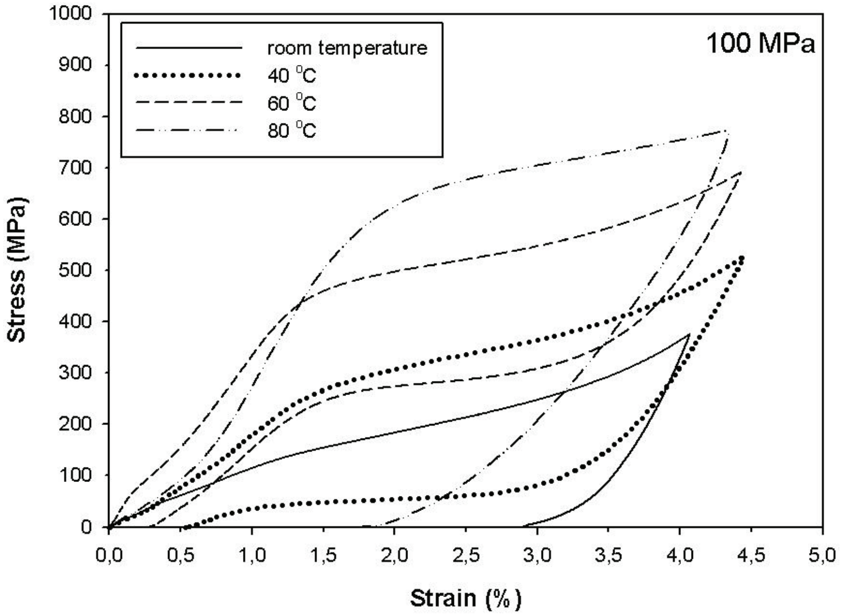

Figure 4.33 Stress-strain diagrams of the specimen aged under 100 MPa at different temperatures.

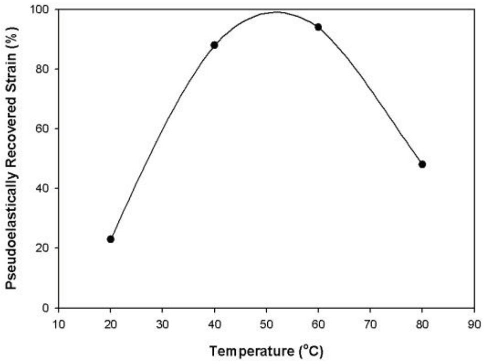

Figure 4.34 Dependence of pseudoelastic recovery on temperature of the alloy aged under 100 MPa.

The stress-strain diagrams of the alloy aged under 200 MPa showing superelasticity tests at different temperatures are given in Figure 4.35. The forward transformation plateau is observable clearly at all temperatures except room temperature as it is for the tests under 100 MPa. In addition, the curves other than 80 ^{o}C, shows the upward deviation from linearity at strains higher than that corresponds to transformation. In this region where stress increases rapidly, pseudoelastic transformation, elastic deformation of martensite and austenite and reorientation of martensite variants take place together.

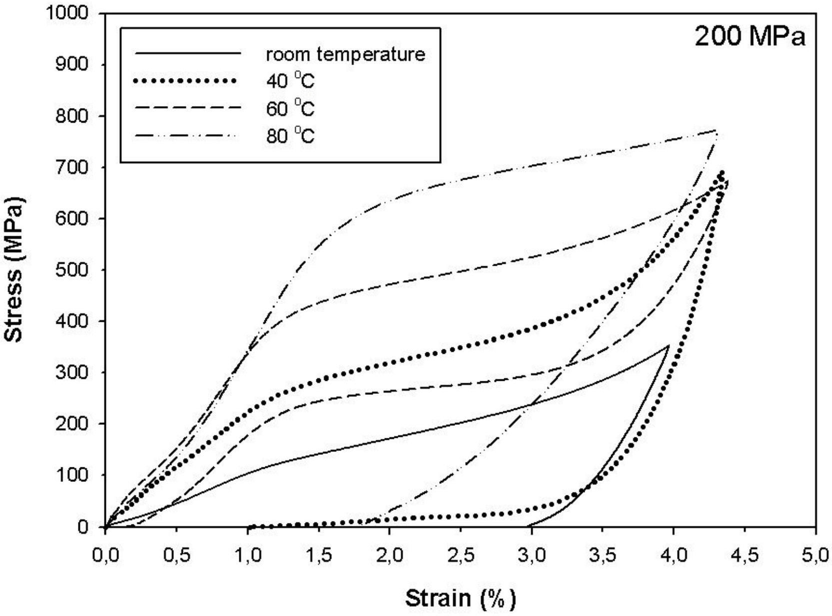

Figure 4.35 Stress-strain diagrams of the specimen aged under 200 MPa at different temperatures.

At room temperature, there are austenite, and R-phase. The transformations taking place upon loading is $B2 \rightarrow R \rightarrow B19'$ and $R \rightarrow B19'$. The pseudoelastically recovered strain, the dependence of which on temperature is given in Figure 4.36, is lower at this temperature due to the fact that the temperature is lower than A_f.

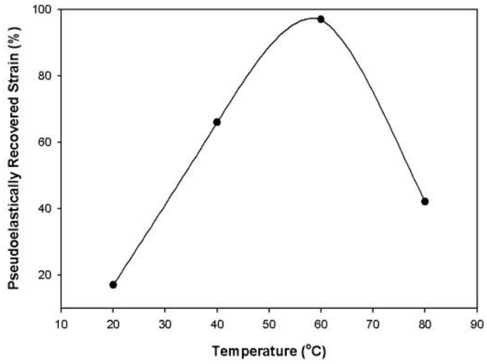

Figure 4.36 Dependence of pseudoelastically recovered strain on temperature for the alloy aged under 200 MPa.

At 40 ^{o}C, R-phase and austenite are present. Since this temperature is around the finish temperature of $B19' \rightarrow B2$ transformation and the formed martensites are only stable under the effect of stress, the recovered strain is increased. At 60^{o}C, the only phase present is austenite and as a result of this most of the total strain is recovered pseudoelastically upon unloading. At 80^{o}C the microstructure is expected to be fully austenitic and as a result of this recovered strain should be higher. However, due to incomplete transformations during anneal at 90 ^{o}C, probably some martensite is retained in the microstructure and with further loading of the alloy, detwinning and reorientation of martensites take place in addition to the stress induced transformation. The abrupt decrease in pseudoelastically recovered strain and increase in unrecovered strain indicate that the in addition to mentioned mechanism dislocation slip also takes place.

Figure 4.37 shows the critical stress for transformation versus temperature relationship. Clausius-Clapeyron constant for the forward transformation of the free aged specimen is found to be 8,22 MPa/ ^{o}K, while in the literature, this value for aged Ni-rich NiTi alloys is given as 5 MPa/ ^{o}K-8 MPa/^{o}K for $B2 \rightarrow B19'$ [56,131-133] and to be in the range of 9-15 MPa/^{o}K for $B2 \rightarrow R \rightarrow B19'$ transformations [56]. In the temperature range of compression tests, upon loading at 20 ^{o}C and 40 ^{o}C $B2 \rightarrow R \rightarrow B19'$ transformations take place, whereas at higher temperatures $B2 \rightarrow B19'$ takes place, as a result of this the Clausius-Clapeyron constant has a values between typical values of the constant of mentioned transformations. Also, the higher value in comparison with that of the as-received ones shows that there is a decrease in the transformation strain. This is related to the fact that due to precipitation the transformed volume decreases.

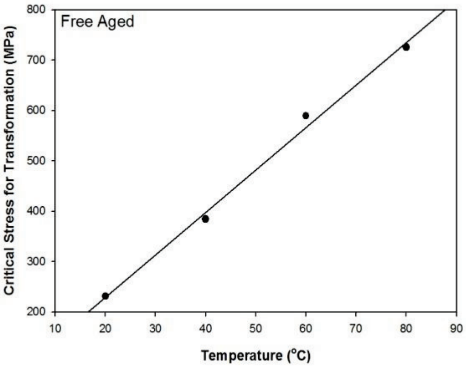

Figure 4.37 Dependence of critical stress for forward transformation on temperature of the free aged specimen.

The change in critical stress for martensitic transformation with increasing temperature of the alloy aged under 20 MPa is given in Figure 4.38. The Clausius-Clapeyron constant for the forward transformation of the specimen aged under 20 MPa is 7,97 MPa/ ^{o}K. Actually this value is between the reported constants for transformation from B2 to B19’ and that including R-phase transformation as an intermediate step. At room temperature and 40 ^{o}C, these transformations take place simultaneously upon loading. However, with increase in temperature the stress induces only $B2 \rightarrow B19$’ transformation.

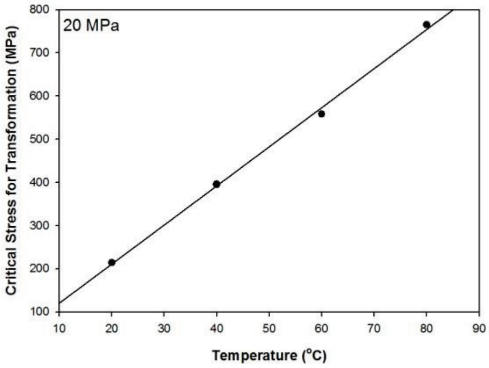

Figure 4.38 Change in critical stress for forward transformation with increasing temperature of the 20 MPa of stress-assisted aged alloy.

Figure 4.39 shows the critical stress temperature relationships for the alloyed aged under 100 MPa of stress. The Clausius-Clapeyron constant for the forward transformation is 9,34 MPa/ ^{o}K,which is higher than the expected value for $B2 \rightarrow B19'$ transformation. However this is related to the fact that upon initial states of loading at room temperature not only elastic deformation of austenite but also stress-induced transformation takes place. When the Clausius-Clapeyron are calculated in the temperature range of 40 ^{o}C -80 ^{o}C, the value decreases to 7.02 MPa/^{o}K which is in agreement with literature [137-139].

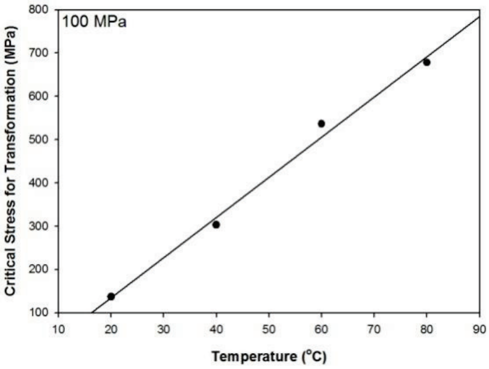

Figure 4.39 Change in critical stress with respect to temperature of sample aged under 100 MPa.

The change in critical stress with test temperature is given in Figure 4.40 for the specimen aged under stress of 200 MPa. The Clausius-Clapeyron constant for the forward transformation of the specimen is 8,64 MPa/ ^{o}K. Again this value is between typical values of the $B2 \rightarrow R \rightarrow B19'$ and $B2 \rightarrow B19'$ transformations [56]. This is also expected since both takes place upon loading in the mechanical test temperature range.

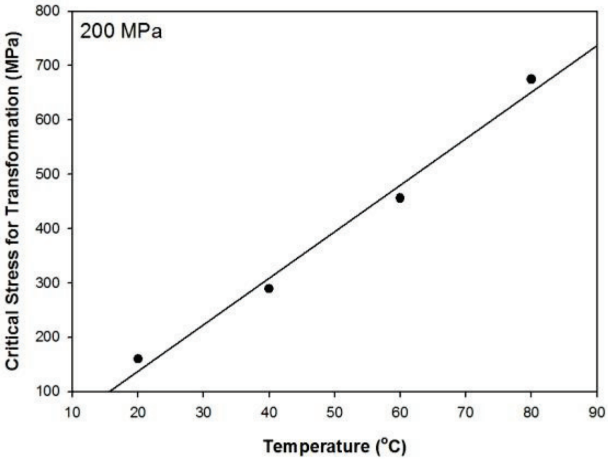

Figure 4.40 Change in critical stress for forward transformation with temperature of a sample aged under 200 MPa.

Figure 4.41 shows dependence of the loading and unloading moduli on temperature for the free aged samples. At 20 ^{o}C, the expected phases are R-phase and B2 according to the DSC curve. However, XRD chart shows the presence of B19’, B2 and Ti_3Ni_4 phases as well indicating that there is retained martensite subsequent to the aging treatment. On the other hand, DSC experiments were conducted by heating and cooling rates of 10^{o}C/min whereas quenching was applied after aging. The faster cooling rate may have suppressed R-phase formation and triggered B19’ instead of it. However, prior to the superelasticity test conducted at 20 ^{o}C, the specimen was annealed and normalized, so that the phases present were R-phase and B2. So, low loading modulus at room temperature is due to the presence of R-phase at this temperature. The loading modulus stays nearly the same when the temperature is raised to 40 ^{o}C since still R-phase is present in the structure. When the temperature is increased to 60 ^{o}C, only austenite is present and as a result of this loading modulus increased. The loading modulus of 80 °C is lower than the expected value. The reason is that at 80 °C, during the previous loading cycles the austenite phases deformed by the strain created as a result of stress induced transformation and the anneal between compression tests at 60 °C and 80 °C does not cause the recovery of the deformation in austenite phase since it is no more elastic but instead plastic at 60°C. As a result of this, the loading slope at 80 °C becomes the elastic modulus of the deformed austenite phase which known to be lower than the undeformed one [140].

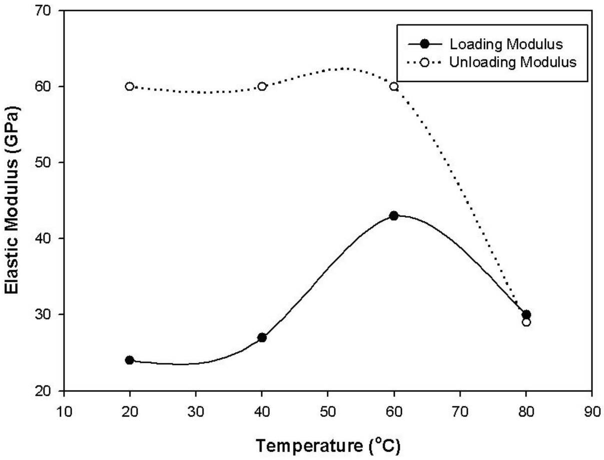

Figure 4.41 Dependence of loading and unloading moduli of free aged specimen on temperature.

Unloading moduli at 20 °C, 40 °C and 60 °C are same indicating that the stress induced martensites amount of which does not change as the temperature is changed. However, as it is explained above, the recovered strain at 20 °C is different from those at 40 °C and 80 °C since this temperature is lower than A_f. In addition to elastic modulus of martensite, following the reverse transformation plateau there is another elastic region upon unloading at 40 °C and 60 °C giving the modulus of deformed parent phases elastically and by stress induced transformation. The slope of this region at 40 °C is around 15 MPa whereas it is around 20 MPa at 60 °C. These values are lower than the expected value of the deformed austenite. However, they are almost equal to the slope of the region which was observed upon loading following to the transformation plateau. Along this region, the stress induced transformation continues in addition to the elastic deformation of austenite regions which are locked by deformation created by transformation. So, upon unloading along the second linear region, reverse transformation and elastic recovery of deformed austenite takes place concurrently. The unloading slope, at 80 °C is equal to the loading slope. The reason is that the main mechanism as response to applied stress is elastic deformation of austenite.

Figure 4.42 shows dependence of elastic moduli on temperature of the alloy aged under 20 MPa. The loading moduli are same at room temperature and 40 °C. The low loading modulus at these temperatures stems from the presence of R-phase. Upon increasing the temperature to 60 °C, the loading modulus increases due to the fact that the only stable phase is austenite. The further increase in loading modulus at 80 °C is related to the increase in loading modulus of austenite with increasing temperature [140] and stabilized martensite via deformation induced during transformation.

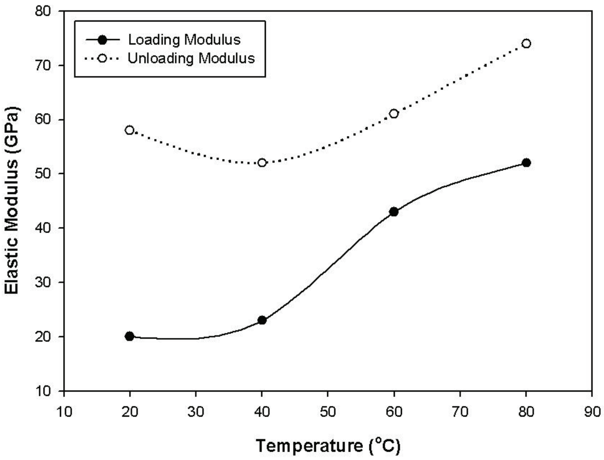

Figure 4.42 Dependence of elastic moduli on temperature of the specimen aged under 20 MPa.

As in the case of loading moduli, the unloading moduli at room temperature and 40°C is nearly equal indicating that the stress induced martensite amount is not different at these temperatures. The increase in unloading modulus with increasing temperature to 60 °C and 80 °C shows that after 40 °C, the amount of stress induced martensite increases with increasing temperature as it is expected when any other deformation mechanism like dislocation slip does not take place. So, it can be said that in the test temperature range, the stresses did not reach to the critical stress for dislocation slip and the dominating response mechanism to the applied stress is stress induced martensitic transformation.

In the Figure 4.43 dependence of elastic modulus observed upon loading and unloading on temperature for the alloy aged under 100 MPa is shown. The loading moduli increase gradually with increasing temperature. The extremely small loading modulus at 20 °C is related to the starting of stress induced transformation immediately upon loading. A similar situation is also valid for the test at 40 °C as it is apparent from the slight increase in loading modulus with increasing temperature. At 60 °C, the loading modulus increases and reaches the expected values, due to increased critical stress for forward transformation with increasing temperature. The increase in loading modulus at 80 °C is related to the increased stability of austenite phase.

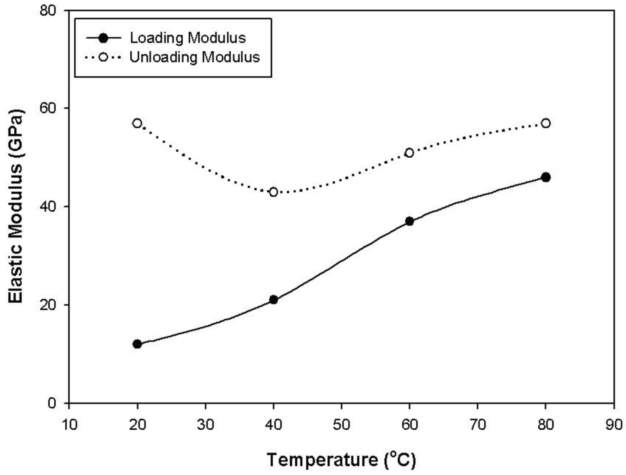

Figure 4.43 Dependence of loading and unloading modulus on temperature of the alloy aged under 100 MPa.

The unloading modulus is nearly same for room temperature, 60 °C and 80 °C, indicating that the stress induced martensite amount is same for all these temperatures. However, the unloading modulus is slightly lower at 40°C. The lower value of unloading modulus at 40

^{o}C can be attributed to the fact that recovery of stress-induced martensite and elastic recovery of austenite take place upon unloading simultaneously, while the elastic deformation of austenite at room temperature is limited, since transformation proceeds immediately. On the other hand at 60 ^{o}C and 80 ^{o}C, the elastic recovery of the austenite phase takes place as a separate region following to the reverse transformation plateau.

Figure 4.44 shows the dependence of loading and unloading modulus on test temperature for the alloy aged under 200 MPa. The loading modulus increases with increasing temperature. The very low loading modulus at 20 ^{o}C is related to the presence of R-phase. In addition, the $R \rightarrow B19'$ transformation starts immediately upon loading. The slight increase in loading modulus at 40 ^{o}C may be attributed to the presence of fewer amounts of R-phase and also transformations that take place along the explicitly observable plateau upon loading. Further increase in loading modulus at 60 ^{o}C is due to the fact that only austenite phase is present at this temperature. On the other hand, the increase in loading modulus at 80 ^{o}C stems from the presence of retained martensite from the former loadings.

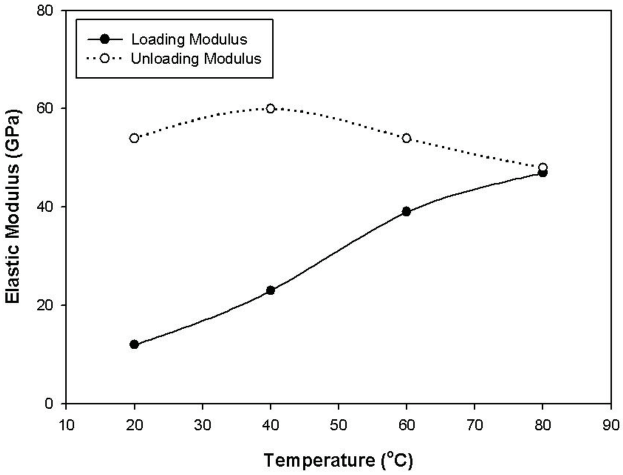

Figure 4.44 Dependence of loading and unloading moduli of a specimen aged under 200 MPa.

The unloading moduli do not change considerably with temperature in the range of 20 ^{o}C to 60 ^{o}C, indicating that the amount of stress induced martensites is constant in this temperature range. On the other hand, there is a slight decrease in unloading modulus when the temperature is increased to 80 ^{o}C. The slight decrease in amount of martensite is related to the multiple mechanisms taking place upon loading. Also, the unloading modulus being equal to the loading modulus, shows that among the mechanisms mentioned above stress induced martensitic transformation is not the dominant one.

4.5. Comparison of Aged Specimens

4.5.1. Phase Analysis

Figure 4.45 shows the XRD patterns of the aged specimens in a comparative manner. The diagrams other than free aged are shifted 2000 cps up with respect to each other. The minimum B2 phase intensity is observed in the free aged specimen, whereas the maximum is seen in the specimen aged under 200 MPa. The same is also valid for the Ti_3Ni_4 phase. In addition, the intensity sequence of the peaks of Ti_3Ni_4 is different for stress-free and stress assisted aging. For the free aged specimen the intensity of the peak at 43.35^{o} is higher whereas after the application of stress during aging the intensity of the peak at 78.30^{o} becomes higher. This shows that with stress-assisted aging variant selection takes place during precipitation. In addition to this, the intensity of B19’ peaks decreases with increasing stress level. In none of the specimen R-phase is observed at room temperature.

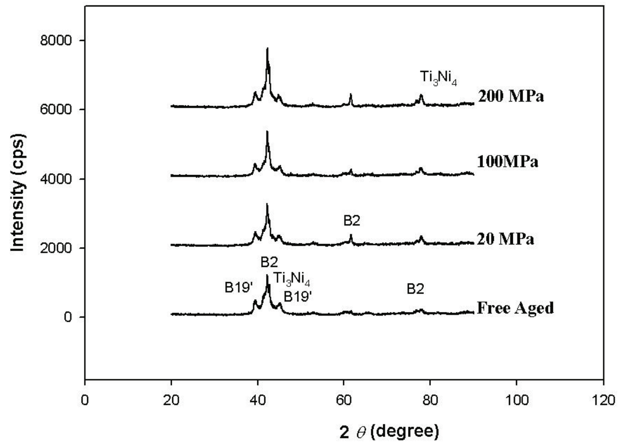

Figure 4.45 XRD patterns of the aged specimen.

4.5.2. Thermal Analysis

Figure 4.46 shows the DSC curves of the hot-rolled and aged specimens together for the second cycle of heating and cooling in (a) and (b) respectively. The transformation sequence changes upon heating and cooling with application of stress. Upon heating, the free aged specimen goes through $B19' \rightarrow R$ and $R \rightarrow B2$ transformation whereas, the transformations taking place upon heating of specimen aged under 20 MPa are $B19' \rightarrow R$, $R \rightarrow B2$, $B19' \rightarrow B2$. On the other hand, only $B19' \rightarrow B2$ transformation occurs in one step when the applied stress is 100 MPa. When the applied stress during aging is increased to 200 MPa, the transformation turns into a two step one and the transformations are $B19' \rightarrow B2$ and $R \rightarrow B2$.

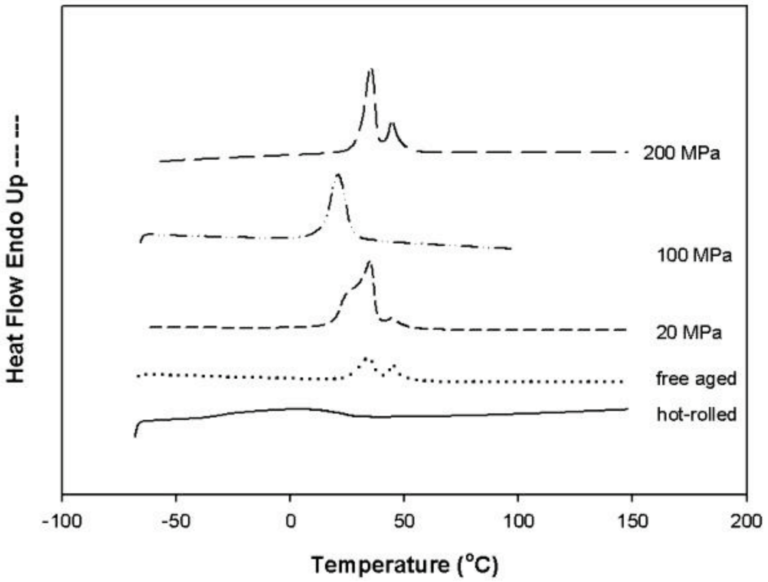

(a)

Figure 4.47 DSC curves of the samples used in study (a) upon heating (b) upon cooling.

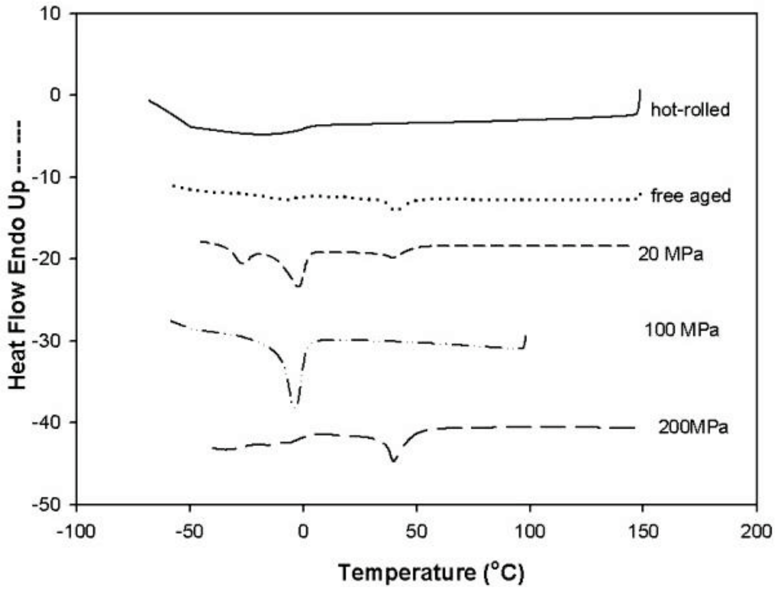

(b)

Figure 4.47 (continued)

Upon cooling, as stress was applied and increased the transformation sequences change. $B2 \rightarrow R$ and $B2 \rightarrow B19'$ transformations are observed during cooling of free aged specimen. For this case another transformation, R →B19', is expected but could not be detected probably due to low thermal stability of the DSC instrument. When 20 MPa of stress is applied, in addition to $B2 \rightarrow R \rightarrow B19'$ transformation, $B2 \rightarrow B19$' also occurs whereas, when the stress applied is increased to 100 MPa, the transformation changes into a single step $B2 \rightarrow B19'$. The only transformation observed upon cooling in the specimen aged under 200 MPa is $B2 \rightarrow R$. However, it is believed that there is $R \rightarrow B19'$ another reaction at lower temperatures yet it could not be detected.

The change in transformation temperatures with applied stress during aging is given in Figure 4.48. The only transformation temperature that shows considerable change with increased applied stress is the start temperature of $B19' \rightarrow B2$ transformation upon heating. The other transformation temperatures show a slight decrease with application of stress, but were not affected from level of stress. Upon cooling, the change in transformation temperatures follows a similar trend. Only the finish temperature of

$B2 \rightarrow B19'$ transformation changes in a significant amount with application of stress during aging.

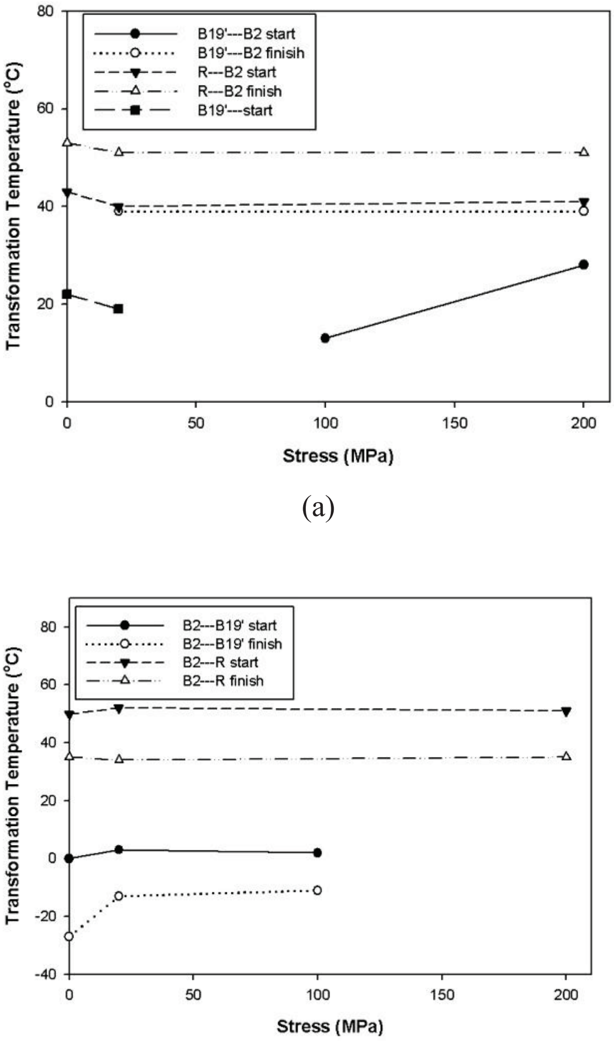

(a)

(b)

Figure 4.48 Change in transformation temperatures with applied stress during aging upon (a) heating, (b) cooling.

The constant temperature of $R \rightarrow B2$ transformation upon heating shows that the matrix composition is same for the all alloys with different thermomechanical history. So, it becomes obvious that the parameters creating change in transformation sequence are interparticle distance, strain levels and the extent of strain into the matrix around the precipitates. It is known that the strain created is effective only for small sized precipitates (up to 50-300 nm) [80]. So, for specimen aged without application of stress and aged under 20 MPa, the precipitate size is estimated to be smaller than 300 nm. The appearance of the $R \rightarrow B19'$ in the latter aging condition is related to the increased size of precipitates. The single step transformation observed in the specimen aged under 100 MPa implies the increased interparticle distance such that the size of the precipitates is larger than the ones formed under any other aging conditions. So, the strain induced by these is smaller and in addition the distance between precipitates is larger than that required for nucleation of martensites [78]. As a result of these, formation of R-phase is not favorable any more.

Although, in the literature it is said that increase in stress level is not effective on nucleation rate, only causes a slight increase in growth rate [94], the change of the transformation sequence from single step to three step when the applied stress level is increased from 100 MPa to 200 MPa contradicts this. The change in transformation sequence implies that the precipitate size and interparticle distance of the precipitates are smaller when 200 MPa of stress is applied instead of 100 MPa during aging. This is only possible when the nucleation rate is higher for the higher stress level so that precipitates can reach only to a limited size.

For an increase in the nucleation rate, an increase is required in the driving force for precipitation. This increase can be related to the orientation of the specimens since the virgin samples are hot-rolled. However, they are from the same batch and their sampling orientation is also identical. So, such an orientation based driving force increase is not possible. The increase in driving force is increase in instability of B2 phase with increased stress level.

4.5.3. Mechanical and Superelastic Characterization

Figure 4.49 given below shows the stress-strain diagram of the aged specimen and dependence of pseudoelastic strain on the applied stress during aging for all different test temperatures. It is known that local stress fields of the coherent precipitates is additive to the applied one and these regions act as nucleation site for the stress induced phase transformation during the superelasticity tests and in result cause a decrease in the critical stress for transformation.

The critical stresses for transformation in these study decreases with applied stresses during aging at all temperatures which is manifested by the downward shift of the stress-strain diagrams. At room temperature, although critical stress for transformation of the as-received sample is greater than those of the other, the pseudoelastic behavior is superior compared to others. There is no considerable difference between the critical stress for forward transformation of free aged specimen and the one aged under 20 MPa, although they are both considerable lower than that of the as received one. When the stress applied during aging is increased to 100 MPa, the critical stress is further reduced. The stress to induce transformation in the specimen aged under 200 MPa is not very different from that of the ones aged under 100 MPa. In addition, there is no clear plateau of transformation for the alloys aged under 100 MPa and 200 MPa.

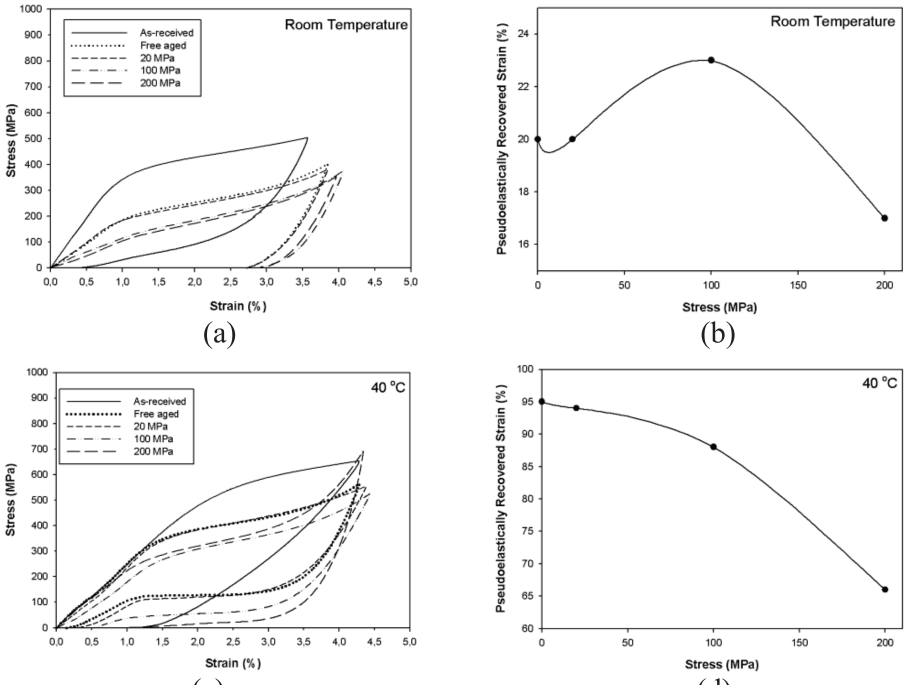

(a) (b)

(c) (d)

Figure 4.49 Stress-strain diagrams of the specimens and dependence of pseudoelastic strain on stress applied during aging at (a-b) room temperature, (c-d) 40 ℃, (e-f) 60 ℃ (g-h) 80 ℃.

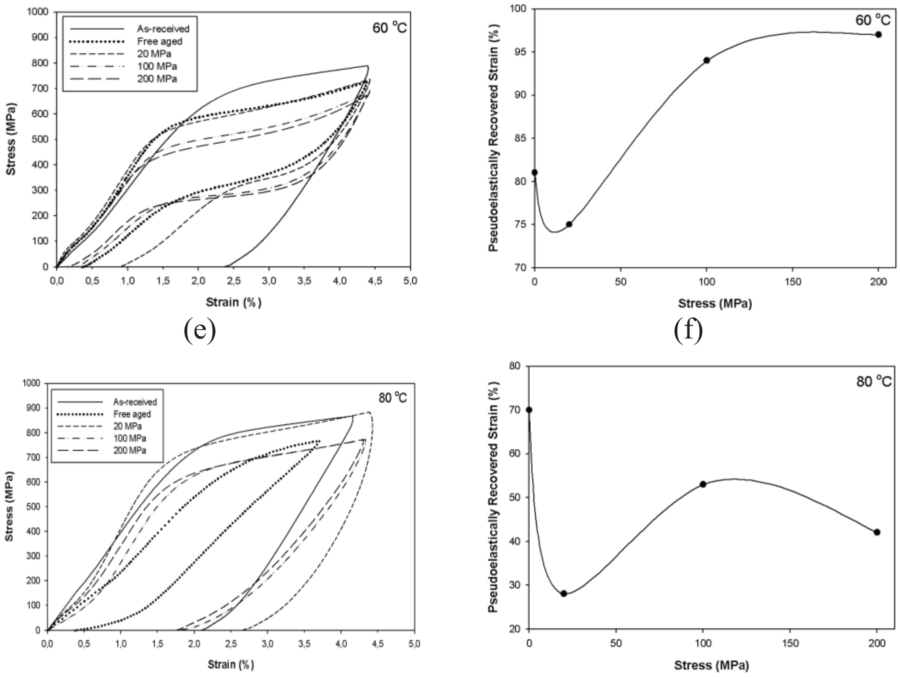

(e) (f)

(g) (h)

Figure 4.49 (continued)

The dependence of critical stresses on aging conditions at any test temperature is not much different from the one at room temperature. While the recovery of as-received one is much superior to the others, which show very limited recovery, at room temperature tests, it falls considerably behind that of the aged specimens at 40 and 60 ^{o}C. At 40 ^{o}C the best recovery is achieved by the free aged samples, whereas at 60 ^{o}C, the ones aged under 200 MPa shows the best recovery. At 80 ^{o}C, none of the specimens show good superelastic properties due to the fact that at this temperature response mechanisms other than stress induced transformation are activated. The mechanisms taking place are dislocation slip, elastic deformation, detwinning and reorientation of martensite variants. Although, the free aged specimen seems to be showing a good superelastic behavior at 80 ^{o}C, it is related to the small total strain applied to this specimen.

Figure 4.50 shows the change in Clausius-Clapeyron constant with applied stress which is related to the response mechanisms activated during loading and the transformations taking place. For the free aged, aged under 20 and aged under 200 MPa alloys, the value is between the typical values of the $B2 \rightarrow R \rightarrow B19'$ and $B2 \rightarrow B19'$ transformations since both transformations take place at all superelasticity test temperatures. Since the dependence of critical stresses on temperature is higher for $B2 \rightarrow R \rightarrow B19'$ than that of $B2 \rightarrow B19'$ [56], Clausius-Clapeyron constant of the specimen aged under 200 MPa being higher than the others can be interpreted as the $B2 \rightarrow R \rightarrow B19'$ transformation becomes dominant in this alloy during superelastic loading, indicating the effect of precipitates are maximum for that specimen. On the other hand, the Clausius-Clapeyron constant of the specimen aged under 100 MPa is typical value for the single phase near equiatomic NiTi alloys exhibiting $B2 \rightarrow B19'$ transformation implying that the effect of precipitates at this temperature is only depletion of Ni content of matrix.

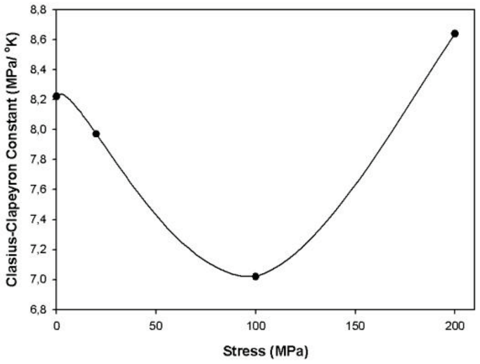

Figure 4.50 Change in Clausius-Clapeyron constant with applied stress during aging.

In addition to superelasticity tests, microhardness measurements were conducted on the specimens. Figure 4.51 shows the change in the microhardness of the specimens during with the applied stress during aging. Microhardness of the aged NiTi alloys are more related to the prevention of dislocation motion than decrease in critical stress for transformation [91]. In other words, size of the precipitates is much more effective than any other parameter. The microhardnesses measured in this study indicate that the precipitate size is minimum when a stress of 20 MPa is applied during again. The smaller microhardness of the alloy aged under 100 MPa compared to 200 MPa also proves the smaller precipitate size of the latter one.

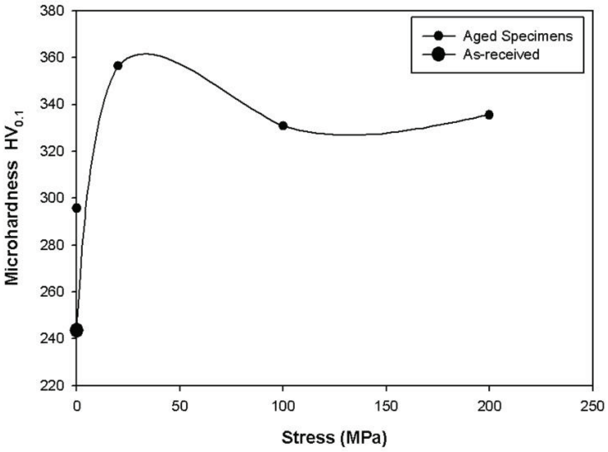

Figure 4.51 Microhardness values of specimens with different thermomechanical histories.

CHAPTER 5

CONCLUSION

1. Hot-rolling, free aging and low-stress level (20 MPa) assisted aging is not enough for homogenization and hindering multi-step transformation.

2. There is a threshold stress level between 20 MPa and 100 MPa to avoid multi-step transformation.

3. Thermal cycling does not cause any difference in transformation behavior or temperatures in hot-rolled and hot-rolled and aged alloys.

4. The transformation sequence is changed with applied stress according to the size and interparticle spacing of the precipitates. It is inferred that the minimum-sized precipitates are formed in the specimen aged under 20 MPa and the largest when aged under 100 MPa, volume fraction being constant.

5. The specimens aged under higher the stress level (200 MPa) behaves as if it has precipitates smaller than the ones aged under 100 MPa. This suggests the relative effect of stress on nucleation and growth of the precipitates changes by stress level. As the stress magnitude is increased, its effect on nucleation surpass its effect on growth due to increased instability of austenite.

6. Upon heating, stress assisted aging is observed to influence only the $B19' \rightarrow B2$ transformation, while other transformations affected only slightly from the stress.

7. $R \rightarrow B2$ transformation temperature being not changed with stress applied during aging indicates that the metastable chemical equilibrium between matrix and precipitates are maintained for each aging condition.

8. Upon cooling, only $B19' \rightarrow B2$ transformation temperature changes considerably with the applied stress.

9. $R \rightarrow B19'$ has been suppressed to the very low temperatures for free aged specimen and the one aged under 200 MPa whereas it is higher for the specimen aged under 20 MPa.

10. Upon loading at different temperatures, different response mechanisms are activated depending on the aging conditions. As a result, recovered strains and Clausius-Clapeyron constants also change.

11. At temperatures where R-phase is present, all specimens except the one aged under 200 MPa show reorientation of R-phase and $R \rightarrow B19'$ transformation.

12. In hot-rolled and free-aged specimen at 60 °C and 80 °C and in the specimen aged under 200 MPa at 80 °C, both dislocation slip and martensite stabliziation via deformation of austenite upon loading takes place simultaneously.

REFERENCES

[1] J.D. Verhoeven, *Fundamentals of Physical Metallurgy,* First Edition, John Wiley & Sons Inc., New York, pp.457, 458 ,1975.

[2] K. Otsuka and C.M. Wayman, *Shape Memory Materials,* Cambridge University Press, Cambridge, pp.3, 1998.

[3] D.A. Porter, K.E. Easterling, *Phase Transformations in Metals and Alloys,* Second Edition, Chapman & Hall, London, pp.382,1992.

[4] C. Bain, *Trans. AIME,* 1924;70:25

[5] K. Otsuka and C.M. Wayman, *Shape Memory Materials,* Cambridge University Press, Cambridge, pp.7, 8, 1998.

[6] J.D. Verhoeven, *Fundamentals of Physical Metallurgy,* First Edition, John Wiley & Sons Inc., New York, pp.471- 474, 1975.

[7] R.E.Reed-Hill, *Physical Metallurgy Principles*, First Edition, D. Van Nostrand Company, New York, pp.638-640, 1973.

[8] D.A. Porter, K.E. Easterling, *Phase Transformations in Metals and Alloys,* Second Edition, Chapman & Hall, London, pp.391,1992.

[9] J.D. Verhoeven, *Fundamentals of Physical Metallurgy,* First Edition, John Wiley & Sons Inc., New York, pp.485, 1975.

[10] K. Otsuka and C.M. Wayman, *Shape Memory Materials,* Cambridge University Press, Cambridge, pp.11, 1998.

[11] K. Otsuka and C.M. Wayman, *Deformation Behavior of Materials*, edited by P. Feltham, Vol. II, Freund Publishing House, Israel, pp. 91, 1977.

[12] Y. Murakami, K. Otsuka, S. Hanada, S. Watanabe, *Mater. Sci. Eng.*, 1994; A189:191.

[13] Y. Murakami and K. Otsuka, *Mater. Sci. Eng.*, 1994; A189:241

[14] K. Otsuka and C.M. Wayman, *Shape Memory Materials,* Cambridge University Press, Cambridge, pp.21-25, 1998.

[15] L. Kaufman, and M. Cohen, *Progress in Metal Physics,* Pergamon Press, Oxford, 1957;7:169.

[16] J.D. Verhoeven, *Fundamentals of Physical Metallurgy,* First Edition, John Wiley & Sons Inc., New York, pp.496,497, 1975.

[17] D.A. Porter, K.E. Easterling, *Phase Transformations in Metals and Alloys,* Second Edition, Chapman & Hall, London, pp.415,416, 1992.

[18] R.E.Reed-Hill, *Physical Metallurgy Principles*, First Edition, D. Van Nostrand Company, New York, pp.655,656, 1973

[19] L. Kaufman, M. Cohen, *Progress in Metal Physics,* 1958;7:165

[20] A. K. Sinha, *Physical Metallurgy Handbook*, First Edition, Mc. Graw-Hill Companies,Inc., New York, pp.8.10-8.21, 2003.

[21] L.C. Chang and T.A. Read, Trans. AIME, 1951; 189:47

[22] D Stöckel, ESOMAT 1989-1st European Symposium on Martensitic Transformations, 1989

[23] H.M. Wu, L.McD. Schetky, *Proceedings, SMST-2000*, Pacific Grove, California, pp.171-182, 2000.

[24] K. Otsuka and C.M. Wayman, *Shape Memory Materials,* Cambridge University Press, Cambridge, pp.36, 1998.

[25] K. Otsuka, *Functional Metallic Materials*, edited by M. Doyama and R. Yamamoto, University of Tokyo Press, pp. 56, 1985.

[26] K. Otsuka, K. Shimizu, *Int. Metals Rev.,* 1986;31:93.

[27] T.W. Duerig, K.N. Melton, D. Stöckel, C. M. Wayman, *Engineering Aspects of Shape Memory Alloys*, Butterworth-Heinemann Ltd, London, 1990.

[28] R. Stalmans, J. Van Humbeeck, L. Delaey, *Acta Metall. Mater.,*1992; 40:501.

[29] G.B. Olson and M. Cohen, Scr. Metall., 1975; 9:1247.

[30] G.B. Olson and M. Cohen, Scr. Metall., 1977; 11:345.

[31] L. Delaey and E. Aernoudt, *Proceeding of International Conference on Martensitic Transformations 1986*, edited by I. Tamura, pp.926, 1987.

[32] G. Guénin, *The Martensitic Transformation in Science and Technology*, edited by E. Hornbogen and E. Jost, DGM Informationgesellschaft, Oberursel, pp. 39, 1989.

[33] E. Zanaboni, Thesis, University of Pavia, 2008.

[34] J. Van Humbeeck and R. Stalsman, *Shape Memory Materials*, edited by K. Otsuka, C.M. Wayman, Cambridge University Press, Cambridge, pp.149-182,1998.

[35] T. Duerig , A. Pelton, D. Stöckel, *Mater. Sci. Eng.,* 1999; A273-275:149.

[36] T. Saburi, T. Tatsumi, S. Nenno, *Journal De Physique,*1982; C4: 261.

[37] J. Van Humbeeck, *J. Eng. Mater. Technol*., 1999; 121:98.

[38] K. Otsuka, X. Ren, *Prog. Mater. Sci.,* 2005;50:511.

[39] W. Tang, *Metall Trans,* 1997; 28A:537.

[40] J. Zhang, G. Fan, Y. Zhou, X. Ding, K. Otsuka, K. Nakamura, J. Sun, X. Ren, *Acta Materialia*, 2007;55:2897.

[41] T.N. Nam, T. Saburi, K. Shimizu, *Mater. Trans. JIM,* 1990;31:959.

[42] M. Matsumoto, T. Honma, *1st JIM International Symposium on Martensite*, *Kobe, Japan*, 1976: 199.

[43] S. Miyazaki, K. Otsuka, *Metall. Trans. A*, 1972; 17A:115.

[44] C.M. Wayman, L. Cornelis, K. Shimizu, *Scripta Mater.*, 1972; 6: 115.

[45] K. Otsuka, T. Sawamura, K. Shimizu, Phys Status Solidi (a), 1971; 5:457.

[46] K.M. Knowles, D.A. Smith, Acta Metall.,1981; 29:101.

[47] T. Saburi, *Shape Memory Materials,* edited by K. Otsuka and C.M. Wayman, Cambridge University Press, Cambridge, pp.49-96,1998.

[48] T. Honma, *Shape Memory Alloys,* edited by H. Funakubo, Gordon and Breach Science Publishers S.A., Amsterdam, pp.61-101,1987.

[49] Y. Shugo, F. Hasegawa, T. Honma, *Bull Research Institute of Mineral Dressing and Metallurgy*, Tohoku University 1981;37:79.

[50] T. Tadaki, C.M. Wayman, *Metallography*, 1982; 15: 247.

[51] T.H. Nam, T. Saburi, K. Shimizu, *Trans JIM*, 1990; 31:1050.

[52] T. Saburi, Y. Watanabe, S. Nenno, *ISIJ Internat.,* 1989; 29:405.

[53] T. Fukuda, T. Saburi, T. Chihara, Y. Tsuzuki, *Mater Trans JIM*, 1995; 36:1248.

[54] F.E. Wang, W. J. Buehler, S.J. Pickart, *Appl. Phys*., 1965; 36:3232.

[55] S. Miyazaki, K. Otsuka, Metall. Trans, 1986; 17A:53.

[56] P. Sittner, V. Novak, P. Lukas, M. Landa, *Transactions of the ASME,*2006;128:268.

[57] P. Sittner, M. Landa , P. Lukas, V. Novak, *Mechanics of Materials,* 2006; 38:475.

[58] S. Miyazaki, S. Kimura, K. Otsuka, *Philos. Mag. A*, 1988; 57:467.

[59] G. D. Sandrock, A.J. Perkins, R.F. Heheman, *Metall. Trans*., 1971; 2:2769.

[60] C.M. Hwang, M. Meichle, M.B. Salamon, C.M. Wayman, *Philos. Mag. A*, 1983; 47: 31.

[61] S. Miyazaki, S. Kimura, K. Otsuka, *Philos. Mag. A*, 1984; 50:393.

[62] V.N. Khachin, V.E. Gjyunter, V.P. Sivokha, A.S. Savvinov, *Proceeding International Conference on Martensitic Transformation 1979*, Cambridge, MA, pp. 474,1979.

[63] V.N. Khachin, Y.I. Paskal, V.E. Gunter, A.A. Monasevich, V.P. Sivokha, Phys. Met. Metallog., 1978;46:49.

[64] H.C. Ling, R. Kaplov, *Metall. Trans A*., 1980; 11:77.

[65] H.C. Ling, R. Kaplov, *Metall. Trans A*., 1981;12:2101.

[66] T. Fukuda, T. Saburi, K. Doi and S. Nenno, *Mater. Trans. JIM,* 1992; 33: 271.

[67] C.M. Hwang, M.B. Salamon, C.M. Wayman, *Philos. Mag. A*, 1983; 47: 177.

[68] M.Nishida, C.M. Wayman, A. Chiba, *Metallography*, 1988;21:275.

[69] M. Nishida, C. M. Wayman, T. Honma, Metall. Trans, 1986; 17A:1505.

[70] R. Kainuma, M. Matsumoto, T. Honma, *Bull Inst Mineral Dressing and Metall*, Tohoku University, 1987; 43:149.

[71] T. Tadaki, Y. Nakata, K. Shimizu, K. Otsuka, *Trans JIM,* 1986;27:731.

[72] T. Saburi, S. Nenno, T. Fukuda, *J. Less- Comm. Metals*, 1986;125: 157.

[73] M. Nishida, C.M. Wayman, R. Kainuma, T. Honma, *Scripta Metall*., 1986; 20: 899.

[74] T. Hara, T. Ohba, K. Otsuka, M. Nishida, *Mater. Trans. JIM*, 1997; 38:277.

[75] A. Taylor, R.W. Floyd, *Acta Crystall.,* 1950; 3:285.

[76] K. Otsuka, T. Kakeshita, *MRS Bulletin*, 2002; 27:91.

[77] J. Zhang, PhD thesis, University of Tsukuba, 2000.

[78] E. Yu. Panchenko, Yu. I. Chumyakov, I.V. Kireeva, A.V. Ovsyannikov, H. Sehitoglu, I. Karaman, Y.H.J. Maier, *The Physics of Metals and Metallography,* 2008; 106: 577.

[79] O. Bojda, G. Eggeler, A. Dlouhy, *Scripta Materialia*, 2005;53:99.

[80] W. Tirry, D. Schryvers, *Acta Materialia*, 2005; 53:1041.

[81] X. Ren, N. Miura, J. Zhang, K. Otsuka, K. Tanaka, M. Koiwa, T. Suzuki, Yu.I. Chumlyakov, M. Asai, *Materials Science and Engineering A*, 2001; 312: 196.

[82] M.C. Carroll, Ch. Somsen, G.Eggeler, *Scripta Materialia,* 2004*;* 50: 187.

[83] E. Hornbogen, V. Mertinger, and D. Wurzel, *Scripta Materialia,* 2001*;* 44: 171.

[84] E. Hornbogen, *Acta Materialia*,1985; 33:595.

[85] Yu. I. Chumlyakov, I. V. Kireeva, I. Karaman, et al.*, Izv. Vyssh. Uchebn. Zaved*., 2004; 9:4.

[86] K. Gall, H. Sehitoglu, Yu. I. Chumlyakov, I.V. Kireeva, H. J. Maier, *Journal of Engineering Materials and Technology,* 199; 121 :19.

[87] J. Khalil-Allafi, A. Dlouhy, and G. Eggeler, *Acta Materialia*, 2004; 52: 4351.

[88] Yu. I. Chumlyakov, S. P. Efimenko, I. V. Kireeva, et al., *Dokl. Ross. Akad. Nauk 381* ,2001; 5: 610.

[89] V. V. Kokorin, *Magnetic Transformations in Inhomogeneous Solid Solutions* Naukova Dumka, Kiev, 1987.

[90] L. Bataillard, J.- E. Bidaux, J. -E., R. Gotthardt, *Philosophical Magazine A*, 1998; 78,2 : 327.

[91] K. Gall, K. Juntunen, H. J. Maier, H. Sehitoglu, Yu. I. Chumlyakov, *Acta Materialia*, 2001; 49: 3205.

[92] Y. Zheng, F.Jiang, L. Li, H. Yang, Y. Liu, *Acta Materialia*, 2008; 56: 736.

[93] J. Khalil Allafi, X. Ren, G. Eggeler, *Acta Materialia,* 2002; 50:793.

[94] J. Khalil Allafi, A. Dlouhy , G. Eggeler, *Acta Materialia,* 2002; 50:4255.

[95] A. Dlouhy, J. Khalil Allafi, G. Eggeler, *Philosophical Magazine A*, 2003; 83:339.

[96] G. Fan, W. Chen, S. Yang, J. Zhu, X. Ren, K. Otsuka, *Acta Materialia,* 2004; 52:4351.

[97] K. Fujishima, M. Nishida, Y. Morizono, K. Yamaguchi, K. Ishiuchi, T. Yamamuro, *Materials Science and Engineering A*, 2006; 438-440: 489.

[98] J. Michutta, Ch. Somsen, A. Yawny, A. Dlouhy, G. Eggeler, *Acta Materialia,* 2006*;* 54:3525.

[99] A.J. Wagoner Johnson, R.F. Hamilton, H. Sehitoglu, G. Biallas, H.J. Maier, Y.I. Chumlyakov, H.S. Woo, *Metallurgical And Materials Transactions A*, 2005; 36A: 919.

[100] J. Khalil-Allafi,G. Eggeler, W. W. Schmahl, D. Sheptyakov, *Materials Science and Engineering A*, 2006; 438-440: 593.

[101] Z.G. Wang, X.T. Zu, X.D. Feng, H.Q. Mo, J.M. Zhou, *Materials Letters*, 2004; 58: 3141.

[102] L.J. Chiang, C.H. Li, Y.F. Hsu, W.H. Wang, *Journal of Alloys and Compounds*, 2008; 458:231.

[103] J.I. Kim, Y. Liu, S. Miyazaki, *Acta Materialia,* 2004; 52: 487.

[104] R.Portier, D. Gratias, *Journal de Physique*, 1982; 43: 17.

[105] J.W. Stewart, R.C. Thomson, H.K.D.H. Bhadesia, *Journal Materials Science*, 1994; 29: 6079.

[106] R. Kainuma, M.Matsumoto, T.Honma, *Proceeding International Conference on Martensitic Transformations,* 1986, 1987; 717.

[107] D.Y. Li, L.Q. Chen, *Acta Materialia,* 1998; 45:2435.

[108] D.Y. Li, L.Q. Chen, *Acta Materialia,* 1998; 46:639.

[109] D.Y. Li, L.Q. Chen, *Acta Materialia,* 1997; 45:471.

[110] J. Michutta, M.C. Carroll, A. Yawny, Ch. Somsen, K. Neuking, G. Eggeler, *Materials Science and Engineering A,* 2004; 378:152.

[111] D. Favier, Y. Liu, L. Orgeas, A. Sandel, L. Debove P. Comte-Gaz, Y. Liu, *Materials Science and Engineering A*, 2006; 429: 130.

[112] O. Bojda, G. Eggeler, A. Dlouhy, *Scripta Materialia*, 2005; 53: 99.

[113] S. W. Robertson, V. Imbeni,H.-R. Wenk, R. O. Ritchie, *Wiley Periodicals, Inc.,* 2005; 190.

[114] C. P. Frick, A. M. Ortega, J. Tyber, K. Gall, H. J. Maier, *Metallurgical And Materials Transactions A*, 2004 ; 35: 2013.

[115] L. McD. Schetky, M.H. Wu, *Memry Corporation,* Bethel, Connecticut, USA.

[116] C. P. Frick, A. M. Ortega, J. Tyber, A. El. M.Maksound, H. J. Maier,Y. Liu, K. Gall, , *Materials Science and Engineering A*, 2005 ; 405: 34.

[117] S.K. Wu, H.C. Lin, *Materials Chemistry and Physics,* 2000; 64:81.

[118] J.Tyber, J. McCormick, K. Gall; R. DesRoches, H. J. Maier, A. E. A. Maksoud, *Journal Of Engineering Mechanics*, 2007: 1.

[119] P. Filip, K. Manzanec, *Scripta Materialia*, 2001; 45:701.

[120] F.J. Humphreys, M.Hatherly, *Recrystallization and Related Annealing Phenomena*, Second Edition, Elsevier, Oxford, 2004, pp. 310-312.

[121] H.C. Lin,S.K. Wu, Materials Science and Engineering A,1992; 158:87.

[122] ASTM E209-00; Standard Practice for Compression Tests of Metallic Materials at Elevated Temperatures with Conventional or Rapid Heating Rates and Strain Rates.

[123] C. P. Frick,T. W. Lang, K. Spark, K. Gall, *Acta Materialia,* 2006; 54:2223.

[124] ASTM F2004-05, Standard Test Method for Transformation Temperature of Nickel-Titanium Alloys by Thermal Analysis.

[125] M. Nishida, C.M. Wayman , T. Honma . *Metall. Trans. A*, 1986;17:1505.

[126] S. Miyazaki, Y. Kohiyama, unpublished work.

[127] R. Delville, B. Malard, J. Pilch, P. Sittner, D. Schryvers, *International Journal of Plasticity*, 2011; 27:282.

[128] S. Manchiraju, Ph.D. Thesis, Ohio State University, 2011

[129] K. Gall, H. Sehitoglu, Y.I. Chumlyakov, I.V. Kireeva, *Scripta Materialia*, 1999, 40:7.

[130] H. Sehitoglu, I. Karaman, R. Anderson, X. Zhang, K. Gall, H. J. Maier, Y. Chumlyakov, *Acta Materialia,* 2000; 48:3311.

[131] K. N. Melton, O. Mercier, *Acta Metall.,* 1981; 29:393.

[132] S. Miyazaki, K. Otsuka, *Philosophical Magazine A,* 1984; 50: 393.

[133] G.B. Stachowiak, P.G. McCormick, *Acta Metall.,* 1998; 33:391.

[134] Y. Liu, H. Yang,*Smart Materials and Structures*, 2007; 16:22.

[135] Y. Liu, D. Favier, *Acta Materialia,* 2000; 48:3489.

[136] G. Tan, Y. Liu, *Intermetallics*, 2004; 12:373.

[137] L.C. Brinson, I. Schmidt, R. Lammering, *Journal of Mechanics and Phyics of Solids*, 2004; 52:1549.

[138] P.H. Leo,T.W. Shield,et al., *Acta Metall. Mater.,* 1993; 41 (8): 2477.

[139] P.H.Lin, H. Tobushi, et al., *JSME Int. J. Ser. A—Mech. Mater. Eng*., 1996; 39 (1): 117.

[140] Y. Liu, H. Xiang, *Journal of Alloys and Compounds*, 1998; 270:154.